

Scatterometer Image Reconstruction Tuning and Aperture Function Estimation
for the Advanced Microwave Scanning Radiometer
aboard the Earth Observing System

Brian A. Gunn

A thesis submitted to the faculty of
Brigham Young University
in partial fulfillment of the requirements for the degree of
Master of Science

David G. Long, Chair
Richard W. Christiansen
Brian A. Mazzeo

Department of Electrical and Computer Engineering
Brigham Young University
August 2010

Copyright © 2010 Brian A. Gunn

All Rights Reserved

ABSTRACT

Scatterometer Image Reconstruction Tuning and Aperture Function Estimation

for the Advanced Microwave Scanning Radiometer

aboard the Earth Observing System

Brian A. Gunn

Department of Electrical and Computer Engineering

Master of Science

AMSR-E is a space-borne radiometer which measures Earth microwave emissions or brightness temperatures (T_B) over a wide swath. AMSR-E data and images are useful in mapping valuable Earth-surface and atmospheric phenomena. A modified version of the Scatterometer Image Reconstruction (SIR) algorithm creates T_B images from the collected data. SIR is an iterative algorithm with tuning parameters to optimize the reconstruction for the instrument and channel. It requires an approximate aperture function for each channel to be effective.

This thesis presents a simulator-based optimization of SIR iteration and aperture function threshold parameters for each AMSR-E channel. A comparison of actual T_B images generated using the optimal and sub-optimal values is included. Tuned parameters produce images with sharper transitions between regions of low and high T_B for lower-frequency channels. For higher-frequency channels, the severity of artifacts due to temporal T_B variation of the input measurements decreases and coverage gaps are eliminated after tuning.

A two-parameter Gaussian-like bell model is currently assumed in image reconstruction to approximate the AMSR-E aperture function. This paper presents a method of estimating the effective AMSR-E aperture function using T_B measurements and geographical information. The estimate is used as an input for image reconstruction. The resulting T_B images are compared with those produced with the previous Gaussian approximation. Results support the estimates found in this paper for channels 1h, 1v, and 2h. Images processed using the old or new aperture functions for all channels differed by a fraction of a Kelvin over spatially smooth regions.

Keywords: AMSR-E, radiometer, image reconstruction, deconvolution, aperture function, parameter tuning.

ACKNOWLEDGMENTS

This thesis is not my own. It belongs to the people who have helped me overcome challenges, adapt to changes, and make difficult choices in my personal and educational progress. It seems that my friends and family have put more into this thesis than I have.

My parents have been the most influential in helping me understand the importance of education and supporting me in that endeavor. My siblings have helped me keep a balance between scholarship and other “ships,” so I do not go overboard with my engineering work. Teachers and church leaders have been more than that to me as they’ve mentored, befriended, and put up with me.

Thanks to my colleagues and friends, to Faözi, for biking with me, and to an unknown benefactor who paid my tuition when I was dealing with medical bills. This person never quacked, so I say thanks here.

Lastly, thanks to Dr. Long, who taught me the importance of asking the right questions and that engineers aren’t (necessarily) as bland as their stereotype.

TABLE OF CONTENTS

LIST OF TABLES	vi
LIST OF FIGURES	viii
Chapter 1 Introduction	1
1.1 Motivation	1
1.2 Thesis Statement	2
1.3 Contributions	2
1.4 Thesis Outline	3
Chapter 2 Background	5
2.1 Introduction	5
2.2 Microwave Earth Remote Sensing (MERS)	5
2.3 Radiometry	6
2.4 AMSR-E	9
2.5 T_B Image Notation	12
2.6 Scatterometry Image Reconstruction (SIR)	13
2.7 SIR for AMSR-E	18
Chapter 3 SIR Parameter Optimization	21
3.1 Simulation	21
3.1.1 Process	22
3.1.2 Simulation Noise	22
3.1.3 Reference Scene	24
3.1.4 Local Time of Day (LTOD) vs Daily Images	25
3.2 SIR Iteration	26
3.3 Aperture Function Threshold	31
3.4 Conclusion	34
Chapter 4 AMSR-E Aperture Function Estimation	35
4.1 Formulation	35
4.1.1 Mathematical Formulation	35
4.1.2 Geographic Region and Implications	38
4.1.3 Models	43
4.2 Simulation	44
4.3 AMSR-E Aperture Function Estimates	58
4.4 Conclusion	63
Chapter 5 Comparisons	65
5.1 Tuning	65
5.1.1 Iteration	66
5.1.2 Threshold	71

5.2	Aperture Function Estimate	71
5.3	Conclusion	100
Chapter 6	Conclusion	101
6.1	Contributions	102
6.2	Future Work	102
REFERENCES	103
Appendix A	Antenna Far Field and the Fast Fourier Transform	105
Appendix B	ξ and Aperture Rotation Bias	111

LIST OF TABLES

2.1	AMSR-E channels	11
2.2	Assumed Aperture Function Contours	18
3.1	ΔT for AMSR-E simulation	23
3.2	Tuned SIR parameters	34
4.1	Islands selected for each channel.	43
4.2	Gaussian model parameters for aperture function estimates.	63

LIST OF FIGURES

2.1	Radiometry distributed target	6
2.2	AMSR-E T_B 4v images.	7
2.3	AMSR-E image products	8
2.4	AMSR-E instrument.	9
2.5	Aqua satellite	10
2.6	AMSR-E orbit and scan geometry.	11
2.7	GRD, SIR, and sampling density images of Greenland	13
2.8	Sampling with an aperture function	15
2.9	SIR in the Frequency Domain	16
2.10	Assumed Aperture Function Contours	17
2.11	T_B image showing imaging gaps because of untuned aperture function thresholds.	18
3.1	Synthetic scene and simulator-sampled SIR images	21
3.2	Measurement standard deviation (\mathbf{V}) image	23
3.3	Reference scene spectrum	25
3.4	Reference scene	25
3.5	Simulated error images for SIR iteration	27
3.6	Simulated error images for SIR iteration (low-pass reference)	28
3.7	Error vs SIR iteration	29
3.8	Daily and LTOD errors	30
3.9	Optimum iteration with varying simulation noise	32
3.10	Threshold optimization (LTOD)	33
3.11	Threshold optimization (Daily)	34
4.1	AMSR-E sampling	36
4.2	A 1D aperture function estimation spectrum representation	38
4.3	T_B measurements over target island	40
4.4	G-matrix singular values	41
4.5	Noiseless T_B simulated measurements	45
4.6	Channel 1 LS/low-pass aperture function estimates for noiseless simulation	46
4.7	Channel 1 \cos^n and Gaussian aperture function estimate for noiseless simulation	47
4.8	Channel 1 LS/low-pass aperture function estimates for noisy simulation	48
4.9	Channel 1 \cos^n /Gaussian noisy simulation results	49
4.10	Channel 2 LS/low-pass aperture function estimates for noisy simulation	50
4.11	Channel 2 \cos^n /Gaussian noisy simulation results	51
4.12	Channel 3 LS/low-pass aperture function estimates for noisy simulation	52
4.13	Channel 3 \cos^n /Gaussian noisy simulation results	53
4.14	Channel 4 LS/low-pass aperture function estimates for noisy simulation	54
4.15	Channel 4 \cos^n /Gaussian noisy simulation results	55
4.16	Channel 5 LS/low-pass aperture function estimates for noisy simulation	56
4.17	Channel 5 \cos^n /Gaussian noisy simulation results	57
4.18	Aperture function estimate for channel 1, v/h pol	59
4.19	Sampling aperture estimates for channels 2, h/v pol	60

4.20	Sampling aperture estimates for channels 3, h/v pol	61
4.21	Sampling aperture estimates for channels 5, h/v pol	62
5.1	Iteration comparison: Am1v	67
5.2	N–S T_B cross section through Iceland comparing iterations	68
5.3	E–W T_B cross section through Iceland comparing iterations	69
5.4	N–S T_B cross section through Greenland comparing iterations	70
5.5	N–S T_B cross section through Iceland comparing thresholds	72
5.6	E–W T_B cross section through Iceland comparing thresholds	73
5.7	N–S T_B cross section through Greenland comparing thresholds	74
5.8	Threshold comparison: Am5v	75
5.9	Threshold comparison: Am5v	76
5.10	Threshold comparison: Am6v	77
5.11	Threshold comparison: Am6v	78
5.12	Threshold comparison: AM6v	79
5.13	Threshold comparison: AM6v	80
5.14	Aperture function comparison: Am1v	82
5.15	Aperture function comparison: Am2v	83
5.16	Aperture function comparison: Am3v	84
5.17	Aperture function comparison: Am5v	85
5.18	Aperture function comparison: Am1h	86
5.19	Aperture function comparison: Am2h	87
5.20	Aperture function comparison: Am3h	88
5.21	Aperture function comparison: Am5h	89
5.22	T_B plots comparing aperture functions: A*1h	90
5.23	T_B plots comparing aperture functions: A*2h	91
5.24	T_B plots comparing aperture functions: A*3h	92
5.25	T_B plots comparing aperture functions: A*5h	93
5.26	T_B plots comparing aperture functions: A*1v	94
5.27	T_B plots comparing aperture functions: A*2v	95
5.28	T_B plots comparing aperture functions: A*3v	96
5.29	T_B plots comparing aperture functions: A*5v	97
5.30	N–S T_B cross section through Greenland comparing aperture functions	98
5.31	N–S T_B cross section over Iceland’s coast comparing aperture functions	99
A.1	Model Simplifications	107

CHAPTER 1. INTRODUCTION

1.1 Motivation

All matter produces microwave radiation. The amount of energy produced at specific frequencies, polarizations, and incidence angles contains information about its emitter. Measurements of an object's microwave radiation or brightness temperature (T_B) can be processed to give estimates of some of the object's properties. Radiometers are the instruments which measure T_B .

Spaceborne Earth-scanning radiometers measure the T_B emitted from Earth. They usually have large spatial coverages and high temporal sampling frequencies. In only a few days, complete global coverage can be obtained. Earth T_B images are used to produce maps of phenomena such as wind velocity at the ocean's surface, ocean surface temperature, sea ice classification and extent, atmospheric moisture, precipitation, vegetation, and soil moisture, to name a few. These maps are useful in studies in various fields, including meteorology, climatology, agriculture, and ocean shipping.

For example, consider a storm front over the ocean approaching a populated coastal region. Scientists desire to predict the rain, wind speed, duration, and path of the storm in order to advise those to be affected and to estimate the expected damage. Data from surface-based sensors are limited to those collected by sensors on ships, buoys, aircraft, and land. The sparsity of these data sources can limit the accuracy of the prediction they produce.

On the other hand, a spaceborne radiometer may take hundreds of measurements over the storm of interest at a relatively high spatial sampling density in an interval of just a few minutes. These T_B measurements are used to estimate storm characteristics to obtain more accurate weather predictions. With this and other applications for radiometry data, the drive for improved accuracy and resolution of T_B -derived products is continual.

While T_B measurements are generally taken on an irregularly-sampled spatial grid, methods exist which create regularly-spaced T_B images from T_B measurements. The resolution of a

traditional radiometer image is about the size of the aperture function—or the spatial response function—used to collect the data, which is usually on the order of tens of kilometers. These radiometer images are produced from drop-in-the-bucket or similar algorithms which ignore effects of aperture filtering. Higher resolution images are created by estimating the brightness scene over a finer grid from the measurements after formulating a linear inverse problem [1]. An approximation of the sampling aperture is required in this formulation. Other parameters may also be instrument-specific.

Although originally developed for use with scatterometers, the Scatterometer Image Reconstruction (SIR) algorithm has also been applied to radiometer data to produce higher-resolution images [2]. Data from the Advanced Microwave Scanning Radiometer on the Earth Observation System (AMSR-EOS or AMSR-E) is used in such an adapted SIR algorithm, but SIR tuning parameter values have not yet been optimized for AMSR-E processing. Also, an improved estimate of the sampling aperture may result in improved image reconstruction.

1.2 Thesis Statement

The purpose of this thesis is to improve SIR processing of AMSR-E data to produce better T_B images. We accomplish this by tuning SIR for AMSR-E and by finding an improved estimate of the AMSR-E sampling aperture. Local time-of-day (LTOD) processing (see Section 3.1.4) is also developed for AMSR-E to increase temporal resolution and decrease processing artifacts.

The resulting T_B images have sharper transitions between regions of contrasting T_B , eliminate intra-swath T_B gaps, and decrease the severity of image artifacts due to temporal variation in the T_B measurements. A slight increase in edge consistency in the low-frequency channels results from using the new aperture functions.

1.3 Contributions

This thesis' contributions to the remote-sensing community include:

1. The application of bi-daily LTOD imaging for the AMSR-E instrument.
2. A study exploring the advantages of LTOD over daily images for the Greenland region.

3. An optimization of SIR iteration and sampling aperture threshold parameters for both daily and LTOD AMSR-E data sets.
4. The development of a method for estimating a satellite-based radiometer's aperture function mid-mission, the development of noise-reducing sampling aperture models, and the application of the method and models to AMSR-E.
5. Modification of the SIR algorithm to use the mid-mission AMSR-E sampling aperture estimate for AMSR-E image reconstruction.

These contributions improve SIR images for AMSR-E data. They also justify similar studies for other instruments and establish some new methods for their execution.

1.4 Thesis Outline

The remaining chapters are organized as follows:

- Chapter 2 provides the background for our optimization and estimation problems. Radiometry in general and particulars of the AMSR-E instrument are introduced. Next is a discussion of Scatterometry Image Reconstruction (SIR) and its application to AMSR-E.
- Chapter 3 presents the simulation-based optimization of SIR tuning parameters for daily and LTOD images. A discussion of the simulation and simulation parameters is included.
- Chapter 4 discusses a process for estimating the AMSR-E sampling aperture. Aperture models are developed to increase signal-to-noise ratio (SNR). Estimates of the sampling aperture for each AMSR-E channel are compared to the approximation currently used in SIR.
- Chapter 5 is a comparison of SIR T_B images generated using the current SIR parameter values and sampling aperture as opposed to those suggested in Chapters 3 and 4.
- Chapter 6 concludes and discusses possible future work.

CHAPTER 2. BACKGROUND

2.1 Introduction

This chapter introduces the basic concepts of microwave remote sensing and the specifics of the passive AMSR-E sensor which this study researches. A conceptual introduction of SIR is given, and motivation for the research performed follows. In this chapter, some insignificant detail or principle may seem emphasized or explored while other core topics are only briefly mentioned. The reason is that this chapter's purpose is to provide a background for models and assumptions which rely heavily on those details covered in this chapter. Further explanation follows in the subsequent chapters or appendices.

2.2 Microwave Earth Remote Sensing (MERS)

Microwave Earth Remote Sensing (MERS) includes the techniques used to measure electromagnetic (EM) scattering or emission from the Earth's atmosphere and surface using satellite or airborne instruments. These measurements are taken over spatially-distributed targets and can be used to reconstruct estimate scenes of the electromagnetic scattering or emission properties. Some of the target's physical properties—such as composition, density, temperature, and surface characteristics—affect the EM properties in such a way that they can be estimated using measurements from one or more frequency and polarization channels. Thus, measurements or maps of EM properties can be used to create maps of physical properties.

Among others, the following are created using MERS data: sea ice concentration and type, iceberg location, land usage, foliage, and soil classification, surface elevation, soil moisture, snow cover, sea wind speed/velocity, rain rate, atmospheric moisture/water vapor, surface temperature [3]. These maps have high value in meteorological and climate studies, especially those created using measurements collected by satellite-based sensors. The advantages of using

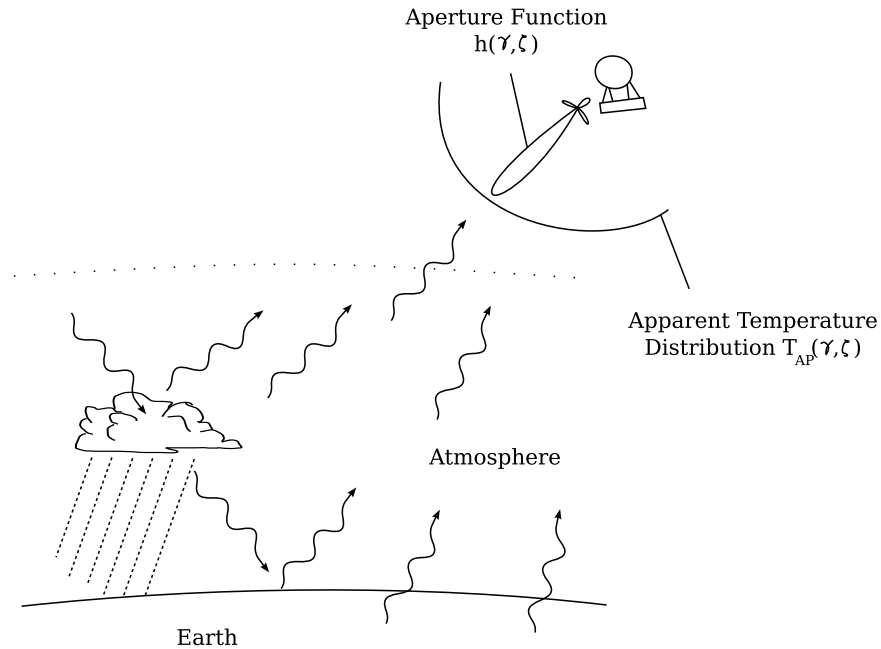


Figure 2.1: Image illustrating the contribution of various sources to the total brightness temperature T_B at the antenna. Each measurement is the result of an inner product of the T_B scene (T_{AP}) and the aperture function $h(\gamma, \zeta)$. The aperture function or an approximate must be known in order to reconstruct the brightness scene at a higher spatial resolution than the size of its main beam.

satellite-based sensors include measurements with relatively high spatial extent and temporal frequency, and a typical mission life-span of several years.

Active sensors transmit a signal towards the scene and measure the return signal. They include radars, scatterometers, and altimeters. On the other hand, radiometers are passive sensors, meaning they measure the signal emitted from the target. Figure 2.1 illustrates the signal model for passive sensors.

2.3 Radiometry

Satellite Earth-scanning radiometers are passive sensors used to measure microwave energy emitted from the Earth at different frequencies and polarizations. This energy is called brightness temperature (T_B), and it is emitted from all matter. An object's T_B increases nearly linearly with its temperature for all microwave frequencies and is dependent on dielectric and physical properties of the emitter. An object's emissivity, $e(\gamma, \zeta, f, p)$, is the incidence-angle, frequency-, and polarization-dependent factor that relates physical temperature T to brightness temperature T_B ,

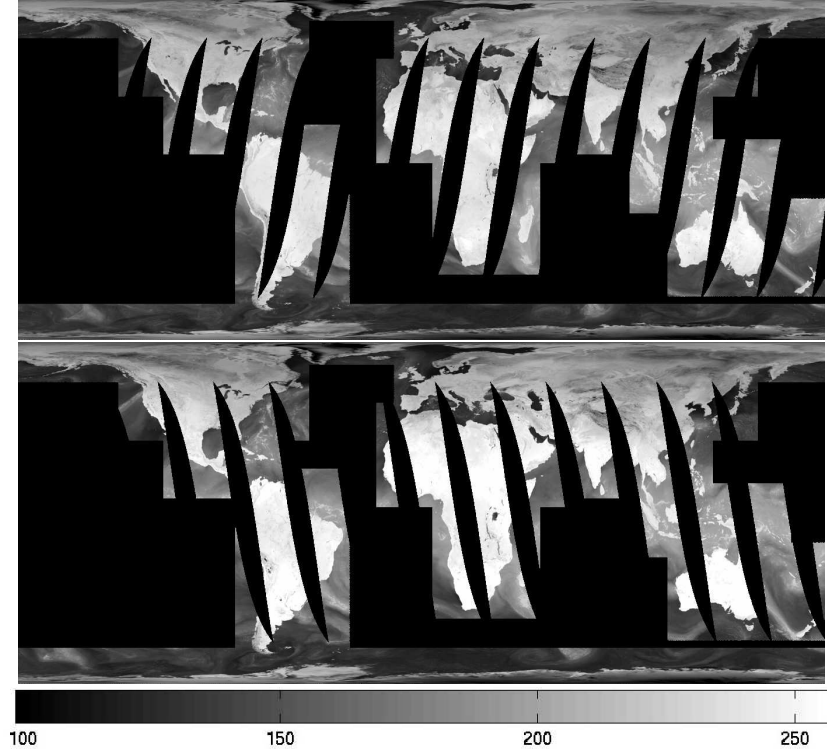


Figure 2.2: AMSR-E T_B images for the 4v channel, showing the midnight/descending (top) and noon/ascending (bottom) images, with half of one day's data used for each. In order to save processing, general-purpose data processing only uses data near continental land.

where both T and T_B are in Kelvin:

$$T_B = e(\gamma, \zeta, f, p) \cdot T,$$

with γ and ζ , the elevation and azimuth angles from the emitter. The parameters f and p are the electromagnetic frequency and polarization, respectively.

For example, the ocean's emissivity is generally much higher for vertically-polarized radiation than for horizontally-polarized radiation. Dry earth, on the other hand, emits similarly at both polarizations. The ratio between the two polarizations can be used to differentiate ocean from land. Advanced techniques are used to estimate more specific target properties [3].

A radiometer's antenna pattern integrates over time and space to produce a single measurement. Figure 2.1 shows how energy from various targets contributes to each measurement. Cosmic radiation and atmospheric emissions produce downwelling energy, or energy traveling

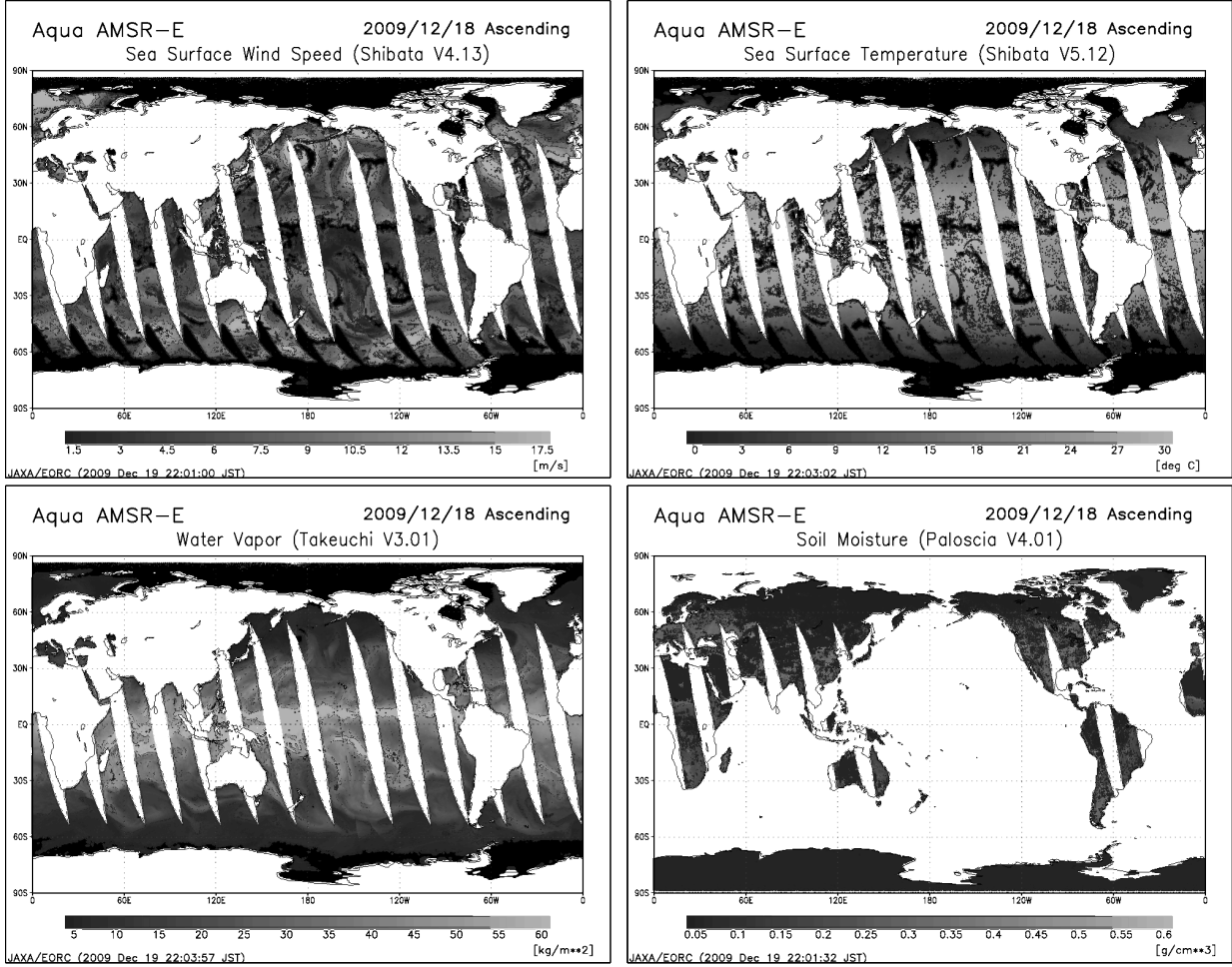


Figure 2.3: Maps of ocean surface winds, temperature, atmospheric water vapor, and land soil moisture estimated using data from the AMSR-E radiometer. These estimates are made by combining measurements from channels of different frequency and polarization through geophysical models or channel comparison algorithms. From [4].

downward toward Earth’s surface. Depending on the surface properties, some down-welling energy is scattered upwards while the rest is absorbed, increasing the surface’s temperature. The energy scattered and emitted from the surface experiences atmospheric attenuation as it travels upward. The atmosphere also emits upwelling energy. The measured T_B at the antenna results from these sources combined in an inner product with the aperture function (or antenna pattern for a stationary antenna) and are sometimes referred to as “aperture-filtered samples.”

The effects of physical phenomena on T_B are a function of electromagnetic frequency and polarization, with higher frequencies generally being more sensitive to atmospheric effects and surface roughness. Maps of phenomenal properties and extent are created by comparing measure-

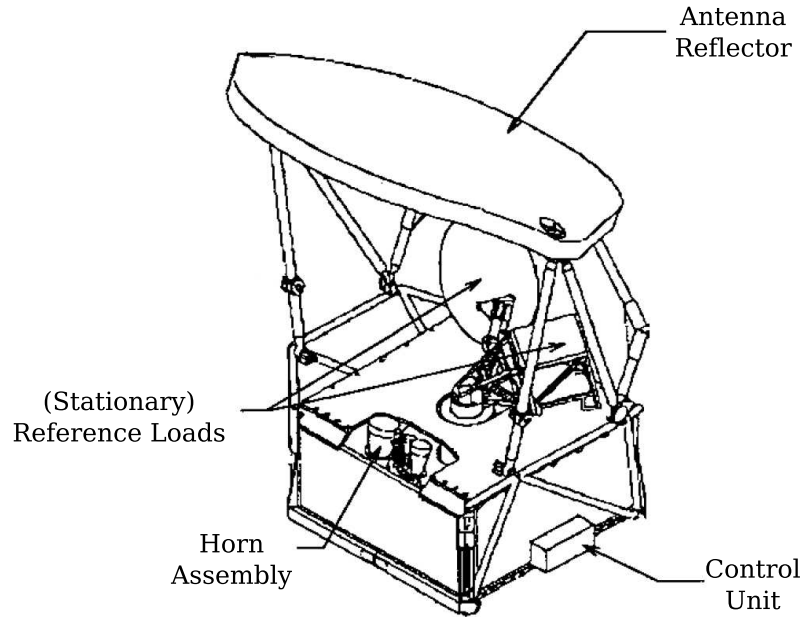


Figure 2.4: The AMSR-E Instrument. The AMSR-E antenna assembly rotates about its azimuth (vertical) axis with a period of 1.5 sec., scanning the Earth’s surface with its pencil-beam aperture function. The illumination of the antenna reflector corresponds to the spectrum of the antenna pattern and is tapered to reduce side lobes in the far-field. The reference loads are measured each rotation for sensor calibration. From [5]. The instrument nadir is towards the bottom of the instrument in its displayed orientation (see Fig. 2.5).

ments at different frequencies and polarizations. Radiometer data has been used to produce maps of snow coverage and depth, sea-ice concentration, precipitation, ocean wind speed, and atmospheric water vapor, to name a few. In Fig. 2.2, the 36 GHz T_B image reveals atmospheric, land, ocean, and ice properties. Figure 2.3 shows ocean surface winds, temperature, atmospheric water vapor, and land soil moisture estimated using data from the AMSR-E radiometer (from [4]).

2.4 AMSR-E

AMSR-E is an Earth-scanning radiometer (see Fig. 2.4). Its satellite platform (Fig. 2.5) travels in a near-polar sun-synchronous orbit at an altitude of 705 km. The AMSR-E antenna assembly includes a 1.6 m diameter reflector dish mounted above a horn assembly, with horns and filters to select frequency and polarization for each channel. Channel specifications are shown in Table 2.1. The antenna footprint refers to the region enclosed by the 3dB contour of the antenna

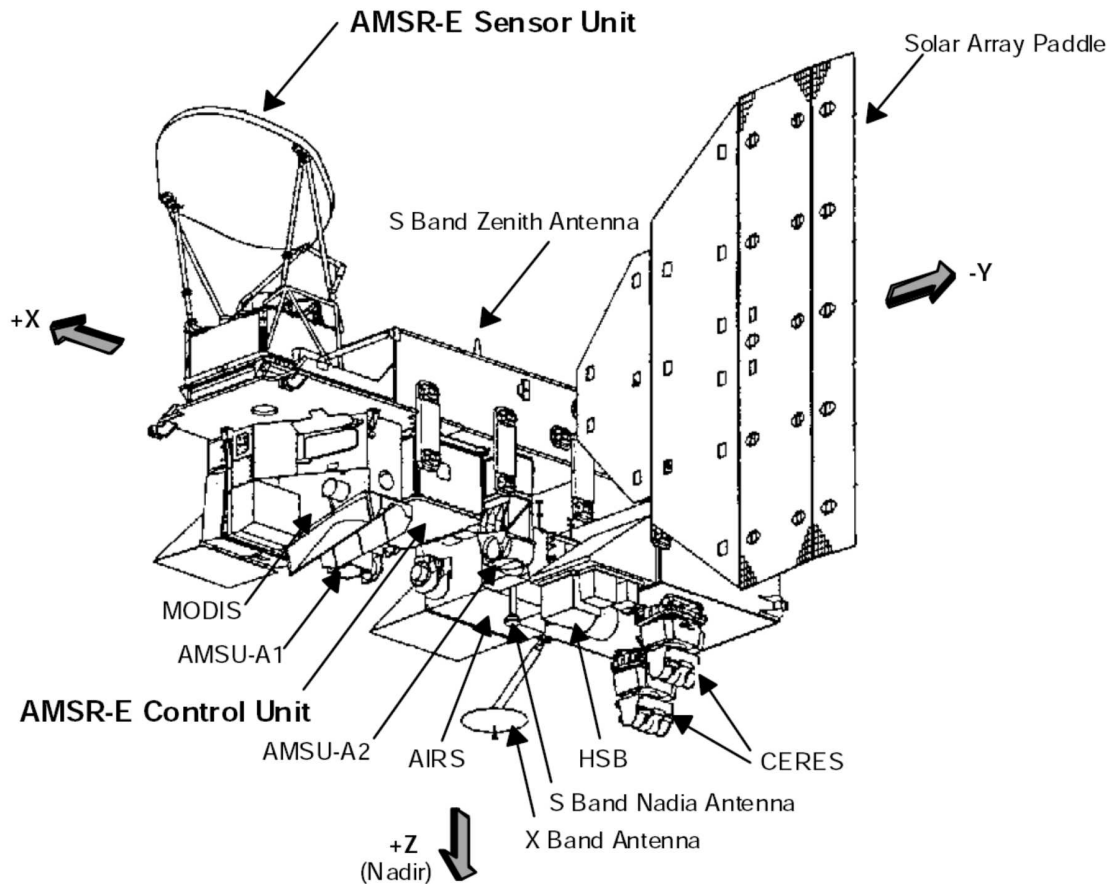


Figure 2.5: The Aqua satellite, with AMSR-E labeled in the upper left, with the flight direction toward +x. From [5].

pattern's projection onto the Earth's surface. Lower-frequency channels generally have larger antenna footprints.

To increase spatial coverage, the antenna assembly rotates every 1.5 seconds, making forward-looking measurements with a nominal incidence angle of 55° (see Fig. 2.6). Each scan across the 1445 km swath collects over 100 samples per channel. The orbit and scan geometry determine the irregular shifts and rotations of the aperture function.

Antenna footprint motion during the sampling integration causes a blur in the aperture function. The satellite nadir point moves at about 7 km/sec, which causes an along-track blur of about 20 m in 2.6 ms—negligible when compared to the kilometer-scale footprint. The instrument

Table 2.1: AMSR-E Channels and their parameters. (Data from [6].)

Channel	Pol.	F_c (GHz)	BW (MHz)	t_{int} (ms)	ΔT (K)	Sampling Interval (km), Specs	3dB Footprint (km)	
							Cross scan	Along scan
1v, 1h	V/H	6.925	350	2.6	0.3	10	74	43
2v, 2h	V/H	10.65	100	2.6	0.6	10	51	30
3v, 3h	V/H	18.7	200	2.6	0.6	10	27	16
4v, 4h	V/H	23.8	400	2.6	0.6	10	31	18
5v, 5h	V/H	36.5	1000	2.6	0.6	10	14	8
6v, 6h	V/H	89.0	3000	1.3	1.1	5	6	4

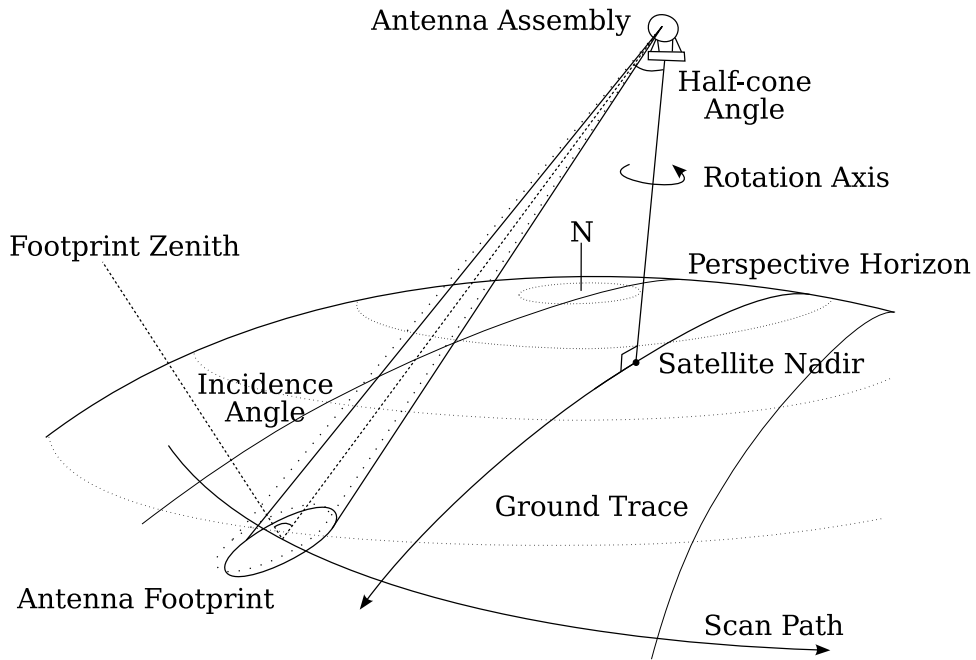


Figure 2.6: AMSR-E scan and orbit geometry, near the start of a descending (southward) orbit. The half-cone beam angle is 47.4° from the rotation axis, which results in the nominal beam incidence angle of 55° with the Earth's surface normal. The dotted- and solid-line beams and antenna footprints represent those at the beginning and end of the measurement sampling integration interval, respectively. The movement during the integration interval causes an along-scan blur in the aperture function. The two lines parallel to the ground trace delimit the pass swath where the scan is active.

rotation, however, results in along-scan speeds upwards of 2000 km/sec, resulting in along scan blurs on the order of kilometers. We assume the shape of the antenna footprint is constant, or that only its orientation and position change. This information provides a basis for our aperture function estimation model.

T_B images using estimates of T_B over regular grids are preferred over the raw irregularly sampled measurements collected by the sensor both for analysis and display purposes. Various techniques are used to create T_B images from AMSR-E data. The drop-in-bucket method produces gridded (GRD) images of coarse resolution—on the order of the aperture function footprint—and obtains pixel values by averaging all measurements whose center lies within it [7]. Other methods (such as Scatterometer Image Reconstruction (SIR), discussed in Section 2.6) use an approximation of the aperture function and attempt to invert the effect of aperture-filtering in the measurements. Pixel resolution of these images can be much higher than that of GRD images.

When creating an image over a particular region, it is common to increase the spatial coverage or sample density by combining swaths. While images traditionally are produced by grouping data in daily sets, data processed using local time-of-day (LTOD) are separated into bi-daily morning and evening images with complete spatial coverage in the polar regions beyond about $\pm 60^\circ$ latitude. The data used for these images have increased temporal resolution and decreased spatial sampling density—characteristics which influence the image characteristics [8]. Figure 2.7 shows sample density images over the Greenland region for both LTOD and daily images. Consecutive swaths are separated by approximately 100 minutes. LTOD is further discussed in Section 3.1.4.

2.5 T_B Image Notation

AMSR-E images are named to specify the instrument, dataset type (LTOD/daily), frequency, and polarization. An “An4v” T_B image is an example. The “A” specifies it as an AMSR-E image, the “n” refers to the LTOD noon dataset, the “4” to the fourth frequency channel, and “v” to vertical polarization. The letter “n” is replaced by “m” when referring to a midnight LTOD image or by an upper-case “M” for the daily image. Frequency channels run from 1 to 6, and polarization is either “h” or “v.” We use this notation extensively in Chapters 3, 4, and 5.

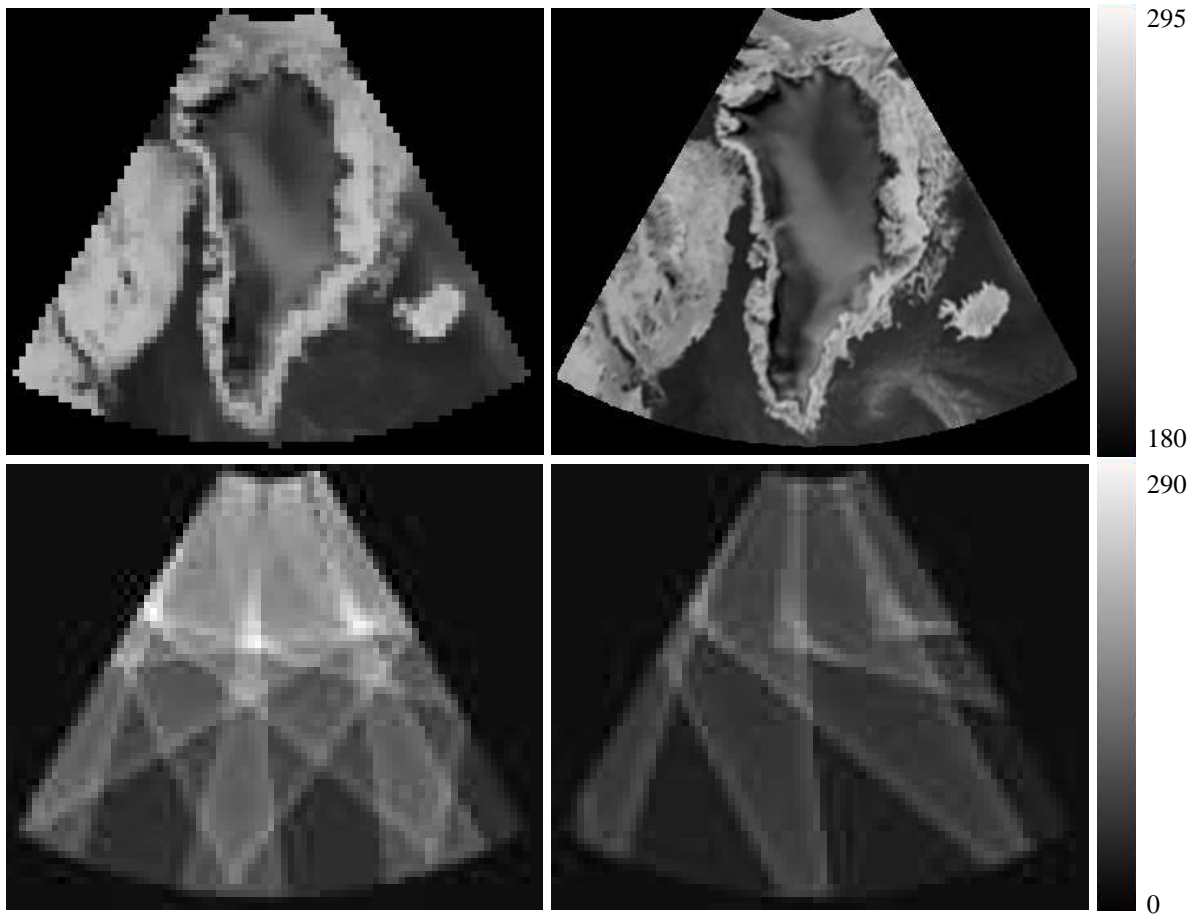


Figure 2.7: Non-enhanced (top left) and SIR (top right) T_B images and daily (bottom left) and noon LTOD (bottom right) sampling density images over the Greenland imaging region. The color bar units for the top are Kelvin. The units of the bottom color bar are the number of measurements contributing to each pixel value. Many measurements overlap within a single swath; the maximum number of swaths over each pixel is 7, with increasing sampling density for each additional swath.

2.6 Scatterometry Image Reconstruction (SIR)

As the name implies, Scatterometer Image Reconstruction (SIR) was originally developed for use with scatterometer data [8,9]. It has since been adapted for use with radiometer data [2]. Depending on aperture function characteristics and surface oversampling, SIR can produce enhanced-resolution images with better resolution than the sensor aperture function footprint.

The premise of this and other image reconstruction techniques lies in each T_B measurement being an inner product of a spatial low-pass aperture function and an all-pass scene (see Fig. 2.8). Because the aperture function is low pass, the T_B measurements are also band limited. Image

reconstruction techniques attempt to invert the effect of the inner product of the T_B scene with the aperture function in order to obtain a T_B estimate over a high-resolution regular grid.

Neglecting noise, we let g represent the Earth's T_B and h represent the aperture function. A T_B measurement y_n is given by

$$y_n = \int g(\vec{v}) h(\theta_n, \vec{x}_n, \vec{v}) d\vec{v} \quad (2.1)$$

where θ_n and \vec{x}_n are the rotation and center location of the aperture function, respectively. The vector \vec{v} describes the displacement from the center of the sampling aperture and is the variable of integration. By applying the same simplifications used in Chapter 4 and with a slight variation on that formulation, the above equation can be expressed discretely by the matrix multiplication $\mathcal{H} \mathbf{g} = \mathbf{y}$ with \mathcal{H} the aperture filtering convolution matrix, \mathbf{g} the discrete vectorized brightness scene over a regular grid, and \mathbf{y} the set of T_B measurements. Because the aperture response is low pass, the Nyquist criterion is satisfied for sufficiently dense sampling, as is the case with AMSR-E. For additional details [8, 9] or Chapter 4.

\mathcal{H} is generally non-invertible, which is due to the null space in the high spatial frequency band. Even within its passband, attenuation may occur at higher frequencies due to the illumination taper of the antenna equivalence current (see Appendix A). Additional noise signal complicates the problem. A low-pass pseudo inverse can provide an estimate of \mathbf{g} , the brightness scene.

SIR is an iterative adaptive algorithm which obtains an estimate of \mathbf{g} from T_B measurements [8]. Because aperture filtering through \mathcal{H} creates band-limited measurements, the best or “ideal” reconstructed image is low-pass. Within the passband of \mathcal{H} , SIR amplifies the signal in those bands which \mathcal{H} attenuates. Figures 2.8 and 2.9 illustrate aperture filtering and scene reconstruction in one dimension, respectively. With increasing iteration, both noise and signal amplification occurs in those bands where the scene spectrum was attenuated, causing reconstruction error to decrease and noise error to increase. The increase in noise error is generally less than the decrease in reconstruction error for a low number of iterations. After many more iterations, however, iterating may increase the total error because of noise amplification.

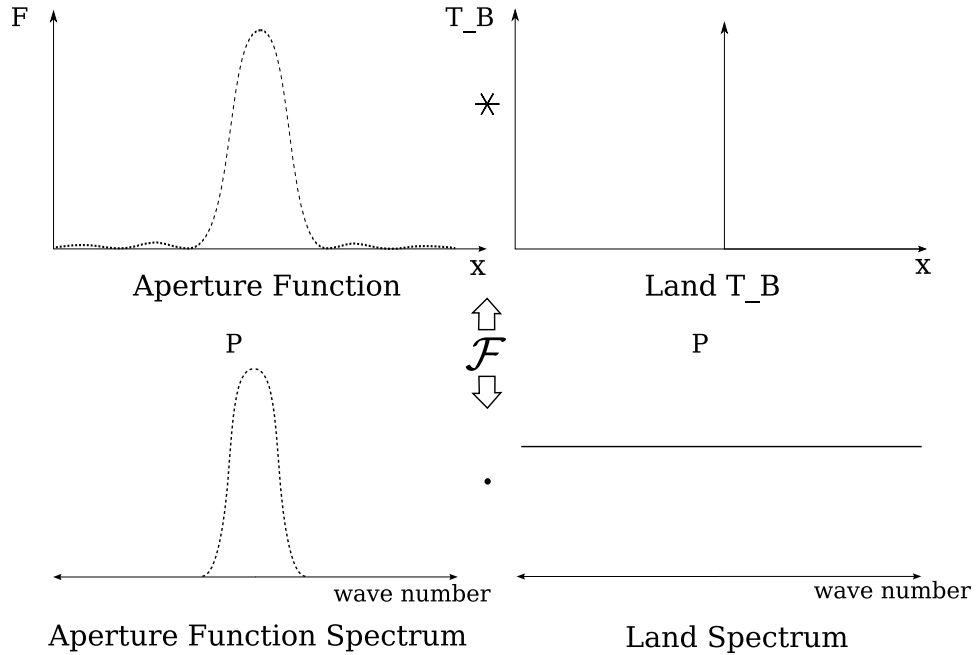


Figure 2.8: 1D representation of aperture filtering in the spatial (top) and spatial-frequency domain (bottom). In space, the aperture-filtered measurements can be represented by a convolution between the sampling aperture and the scene (top). In spatial frequency, the convolution becomes a multiplication (bottom). (Although the scene is not a delta function, its spectrum is non-zero over the support of the aperture spectrum. We use a constant-spectrum scene here and in Fig. 2.9 to illustrate the effects of aperture filtering and subsequent reconstruction.)

Knowledge of the aperture function is required for SIR to be useful in inverting its effects. Although a rough approximation of the aperture function can often be sufficient in SIR, more accurate approximation of the aperture function can produce better quality T_B SIR images.

The assumed aperture function for AMSR-E is a 2 dimensional Gaussian-like bell function with drop-off determined by the major and minor 3dB widths of the antenna pattern's main lobe. This approximation is expressible as

$$h_G(\gamma, \zeta) = 2^{-[(\gamma/\gamma_0)^2 + (\zeta/\zeta_0)^2]}, \quad (2.2)$$

with $h_G(\gamma, \zeta)$, the two-dimensional aperture function approximation, γ and ζ , the elevation and azimuth angles, and γ_0 and ζ_0 , the corresponding 3dB antenna beam widths. Note that a change to

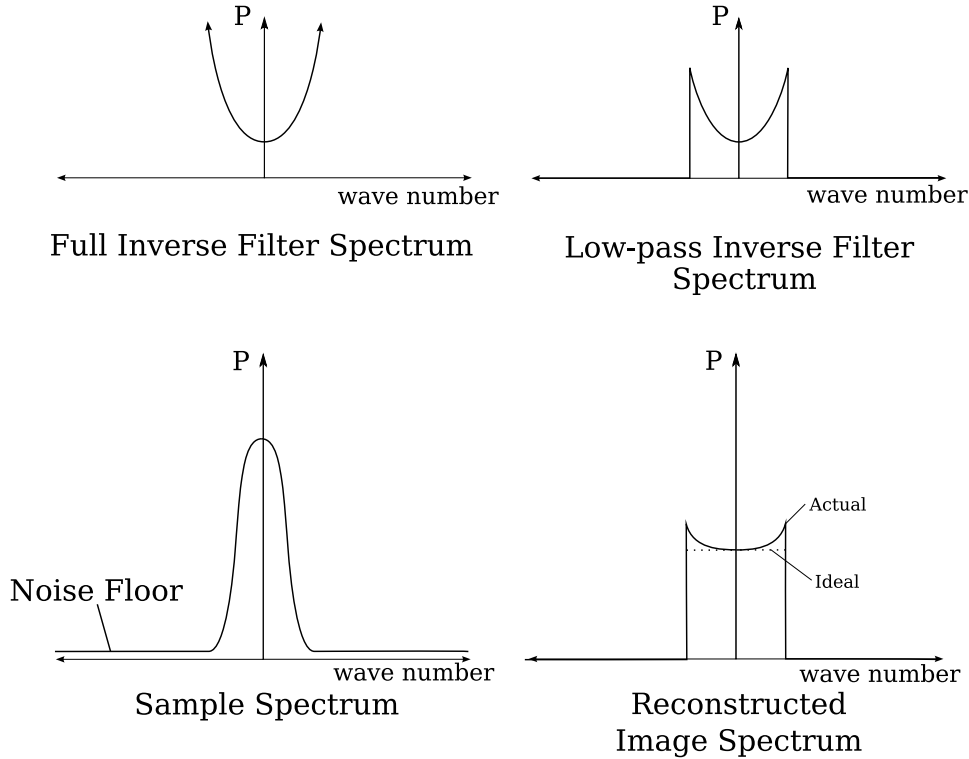


Figure 2.9: A 1D conceptual representation of SIR reconstruction in the spatial-frequency domain. Because the spectrum of the aperture function is tapered, the inverse filter (top left) amplifies the noise added for each measurement (bottom left). The low-pass inverse filter (top-right) limits noise amplification in the estimate (bottom right). Note that the ideal reconstructed scene is a low-pass version of the original. This is due to noise and null-space characteristics of the sampling.

base e provides an equivalent expression in a perhaps more familiar Gaussian exponential form:

$$h_G(\gamma, \zeta) = e^{-(\ln 2) [(\gamma/\gamma_0)^2 + (\zeta/\zeta_0)^2]}.$$

Approximations of this type are favorable because they are easily evaluated and are continuous functions of only two parameters. The Gaussian is a good approximation over the aperture function's main lobe. Although the actual aperture function is band limited (creating side lobes in the aperture function), its spectrum is tapered to reduce power in the side lobes, which reduces the error in this approximation.

The approximate aperture function used in SIR is a spatially-limited function, usually regulated by choosing a lower threshold on the aperture function approximation. Tight spatial restrictions on a good aperture function approximation yield T_B images with poorer quality but at

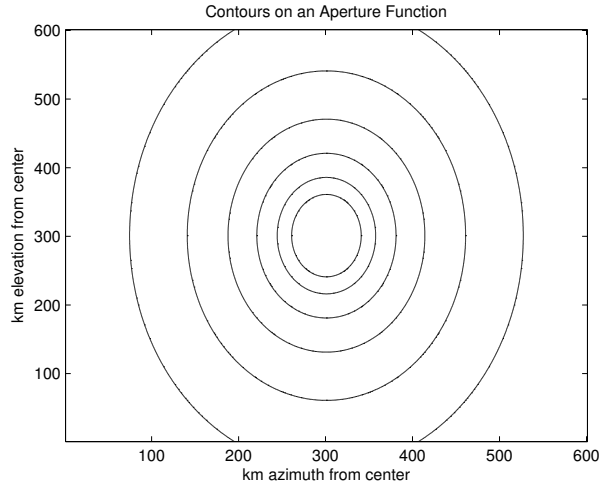


Figure 2.10: Contours of an assumed Gaussian aperture function at levels in Table 2.2, demonstrating the increased accuracy, area, and computational cost associated with decreasing the aperture function threshold.

less computational cost. Because almost all of the aperture function power lies well within its main lobe, very low thresholds (meaning large spatial extent) over the aperture may require unreasonable computation to produce a T_B image comparable to one produced using a less extreme threshold.

Figure 2.10 illustrates. Contours of an assumed aperture function at various thresholds are shown, with major and minor 3dB footprints of 60 and 40 km, respectively. Table 2.2 shows threshold values, the total error, and the computation ratio compared to using the -6 dB threshold. Note that although the error in our table continues to decrease with increasing footprint size, we've assumed here that the assumed aperture function is exact. Because it is a good approximation over only the main lobe, error does not decrease beyond a certain level. Thus, while decreasing the threshold increases computation, it does not necessarily decrease error. The assumed aperture function's -8 dB threshold is currently used to impose a spatial limit on each measurement's contribution.

Although the basic SIR process is the same in its application to any sensor, optimal SIR iteration number, sampling threshold, and aperture function approximation generally change between sensors. Change in noise figures, spatial sampling density, and actual aperture function are some of the primary reasons for instrument- and channel-specific SIR optimization.

Table 2.2: Contours of an assumed Gaussian aperture function at levels shown in Fig. 2.10. The computational ratio is in relation to the -6dB threshold.

Threshold (dB)	-3	-6	-12	-24	-48	-96
Percent Error	50.11	25.05	6.27	0.39	0.00	0.00
Computational Ratio	0.50	1.00	2.00	4.01	8.02	15.31

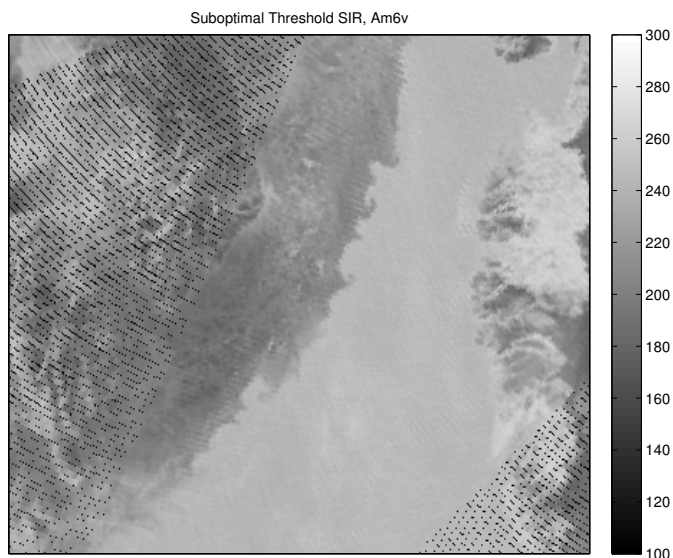


Figure 2.11: T_B image for channel 6 showing gaps in the SIR image because the currently-used -8dB threshold is not small enough, which reduces the effective footprint size. The image shows the south-western shore of Greenland to the right.

2.7 SIR for AMSR-E

The previous section presented SIR and a motivation for optimizing it for a sensor in general. Factors providing addition motivation for AMSR-E-specific optimization are discussed here. These factors depend on background covered earlier in this chapter.

First of all, AMSR-E threshold optimization is clearly necessary. The current SIR threshold is -8dB from the maximum for all channels, which produces T_B images at 36.5 and 89.0 GHz (AMSR-E channels 5 and 6) which have no-data pixels within the swaths of the output images (see Fig. 2.11). This indicates that the contribution limit on each measurement is too restrictive (the

threshold needs to be decreased). AMSR-E channels 1 and 2 have a much larger aperture function main lobe, meaning that the approximation might be restricted more in order to decrease the heavy computational burden without noticeable quality loss in the output images.

Currently, 20 iterations are used in producing AMSR-E SIR images. Because of noise amplification with SIR iteration, AMSR-E channels with higher noise figures should favor lower SIR iteration. While it is less obvious than the need for threshold optimization, iteration number also should be optimized to account for noise figure variations between channels and other factors. Whether or not the optimal value yields results similar to those of the current value, a validation is in order.

The aperture function assumed for the AMSR-E SIR algorithm is a 2D Gaussian-like bell curve with falloff dictated by the 3dB widths of each channel's antenna response. This approximation does not account for the azimuth blur as discussed in Section 2.4, neither does it consider possible rotations or aberrations on the aperture by unknown factors. Improvement in the aperture function approximation can be expected to improve the image quality. Such improvements are considered in succeeding chapters.

CHAPTER 3. SIR PARAMETER OPTIMIZATION

This chapter discusses the optimization of SIR tuning parameters, namely the SIR iteration number and the aperture threshold, for AMSR-E processing. Both are optimized empirically by reconstructing images from simulated data over a synthetic brightness scene. Error between the reconstructed scene and a low-pass synthetic scene is used as a metric for optimization.

First, an introduction of the simulator is provided, along with a discussion of the injected noise, reference scene, and sampling. Local time-of-day versus daily sets are discussed in relation to sampling. Next, a simulator-based optimization of SIR iteration and threshold parameters is presented. Last, a conclusion of SIR tuning and a discussion of the application of optimized values is provided.

3.1 Simulation

This section describes how the simulated measurements are created for use in parameter optimization. First is a discussion of the simulation process, followed by a discussion of injected

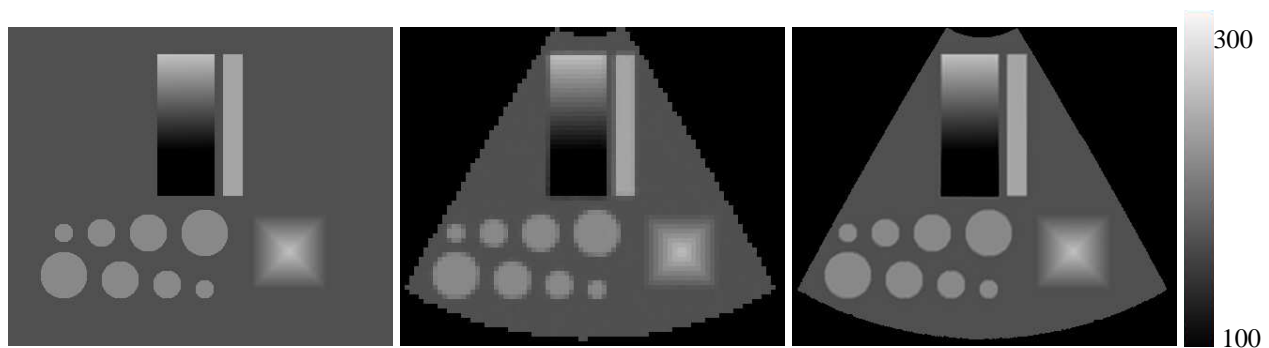


Figure 3.1: The synthetic brightness scene (left) used for simulated AMSR-E sampling and gridded (center) and SIR (right) images from the resulting measurements. The scene sampling and imaging region correspond to those over Greenland, with boundaries at approximately 60° and 80° latitude and -10° and -70° longitude.

simulator noise. Then is a selection of an error reference scene. Finally, local time-of-day (LTOD) sets and simulation sampling is presented.

3.1.1 Process

The simulation-based optimization method is similar to that used in [10]. A synthetic T_B scene is sampled at locations corresponding to actual bi-daily or daily AMSR-E sampling, using the supposed Gaussian-like aperture function for each channel. This produces the simulated T_B measurements. SIR processing is performed many times while varying SIR parameters. Values of parameters which result in the lowest RMS error in the output images are considered optimum.

A synthetic brightness scene is created with spot targets, constant regions, sharp edges, and gradients (Fig. 3.1). The synthetic image is sampled with the supposed Gaussian-like aperture function as dictated by actual sampling locations and aperture rotations of the AMSR-E instrument over the Greenland region. Both daily and LTOD sets are used to reconstruct the brightness scene for varying SIR parameters.

In order to explore changes in reconstruction error and noise error, we use measurements with (1) no noise (signal only), (2) injected noise and no signal, and (3) signal and noise. RMS errors in the resulting SIR images give us approximates of the reconstruction error, noise error, and total error, respectively. The simulated measurements are taken over the synthetic T_B scene, with sampling corresponding to the Greenland region taken for actual data. Both LTOD and daily sets are used. In addition to showing the synthetic scene, Fig. 3.1 also shows a sample low-res “gridded” image and SIR image after the currently-used 20 iterations and -8dB threshold, both reconstructed from synthesized measurements.

3.1.2 Simulation Noise

As mentioned in the previous section, noise-injected simulation measurements are used for optimization to more accurately represent actual AMSR-E sampling. Analysis of actual data is required to determine the noise levels to use in our simulator. Injected noise is of Gaussian distribution, with variance determined through AMSR-E measurement analysis.

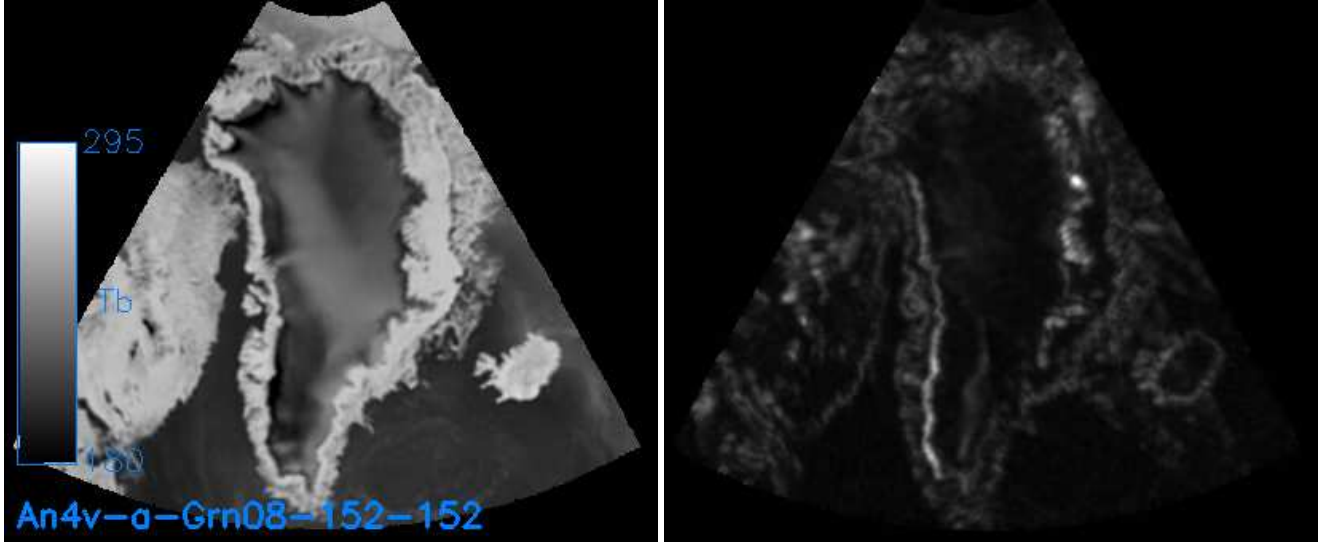


Figure 3.2: The T_B (left) and corresponding \mathbf{V} (right) SIR image product over Greenland for the 4v channel. Pixel values of the \mathbf{V} image are the standard deviation of “overlapping” measurements—or measurements whose measurement footprint overlap at that pixel.

Table 3.1: Estimated ΔT (measurement standard deviation) for AMSR-E Simulation. (\mathbf{m} is the LTOD midnight set, \mathbf{n} is the LTOD noon set, and \mathbf{M} is the daily set.)

	Frequency Channel					
	1	2	3	4	5	6
\mathbf{Amv}	0.41	0.51	0.54	0.52	0.50	0.92
\mathbf{Anv}	0.49	0.71	0.82	0.74	0.66	1.10
\mathbf{AMv}	0.57	0.80	1.11	1.13	1.49	1.86
\mathbf{Amh}	0.56	0.68	0.79	0.86	0.93	0.93
\mathbf{Anh}	0.48	0.61	0.73	0.73	0.73	1.10
\mathbf{AMh}	0.94	1.08	1.54	1.58	1.98	2.01
LTOD average	0.52	0.64	0.76	0.79	0.83	1.01

Figure 3.2 shows a \mathbf{V} image—another type of SIR product—which shows the standard deviation (ΔT) of overlapping measurements from their mean. Note that the \mathbf{V} image is brighter near high contrast regions. This is primarily due to the calculation of the measurement standard deviation from the mean of the overlapping measurements whose center location vary by up to several kilometers. With a rapidly-changing scene, this produces expected variation in the measurements.

The noise standard deviation can be approximated by an average of \mathbf{V} pixel values over a spatially near-constant T_B region. This is the method used to find the values in Table 3.1.

Another method for estimating the ΔT of a channel is to assume that a SIR image evaluated nearest each measurement center is representative of the corresponding mean T_B . Then ΔT is calculated as the standard deviation from the SIR image value at the pixel nearest the measurement center. While this method gives similar results for lower-frequency channel, it is less consistent than the previous method for higher frequencies, so the first method is used as our primary noise estimate.

For reasons discussed in Section 3.2, the optimization of SIR iteration number is highly sensitive to noise. We choose to vary ΔT in the simulation for SIR optimization to explore possible optimal iteration numbers for each channel, based on their noise. Threshold optimization proves very insensitive to noise: the RMS errors in Fig. 3.10 are essentially changed only in a bias with changing ΔT .

Note in Table 3.1 that ΔT is much higher for the daily sets than it is for the LTOD sets. This is mostly attributed to temporal variation between passes. We use the LTOD sets' estimated ΔT in our simulation in order to neglect these temporal changes and for a better comparison of sampling density effects on SIR.

3.1.3 Reference Scene

As mentioned in Section 2.6, the optimal reconstructed signal is a low-pass version of the original. Because the error between the reconstructed scene and the original contains a reconstruction error bias in the high frequency band, we use a low-pass version of the original scene as a reference. Because the frequency support of the ideal reconstructed signal is difficult to pinpoint and may actually vary within each image, we use no-noise simulated measurements to reconstruct an estimate of the ideal low-pass brightness scene with 1000 SIR iterations and use it as the reference for optimization. We do this because we assume the low-pass noiseless reconstruction is very close to the ideal low-pass scene (see [8]).

Figure 3.3 shows the spectra over part of the synthetic image shown in Fig. 3.1, the 1000-iteration reference, and their magnitude difference, all displayed in dB-scale. In Fig. 3.4, the synthetic sub image is displayed, along with the corresponding 1000-iteration reference and a low-

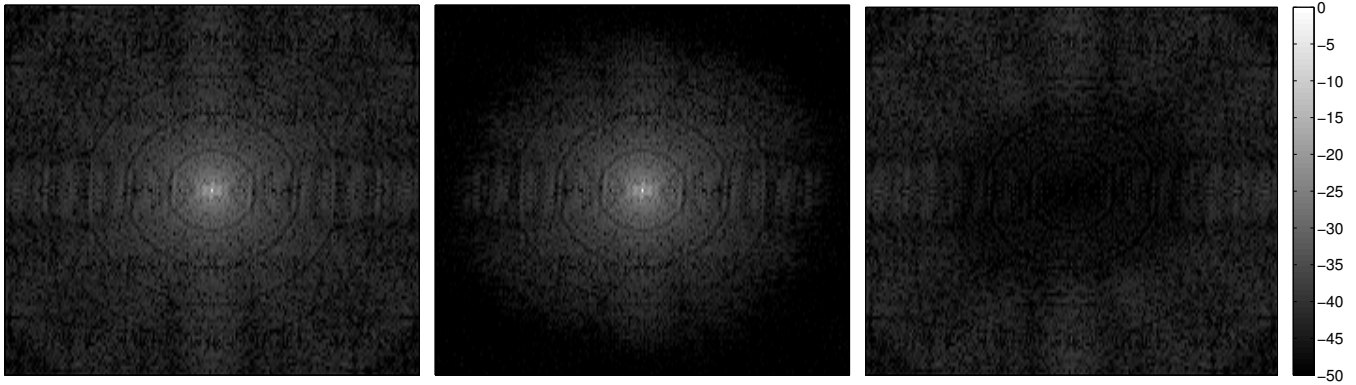


Figure 3.3: The all-pass synthetic brightness scene spectrum (left), the low-pass simulation reference spectrum (center), and their magnitude difference (right), all in log scale. The low-pass reference is a noiseless reconstruction of the brightness scene after 1000 iterations, which we assume to be near the ideal low-pass reconstructed scene.

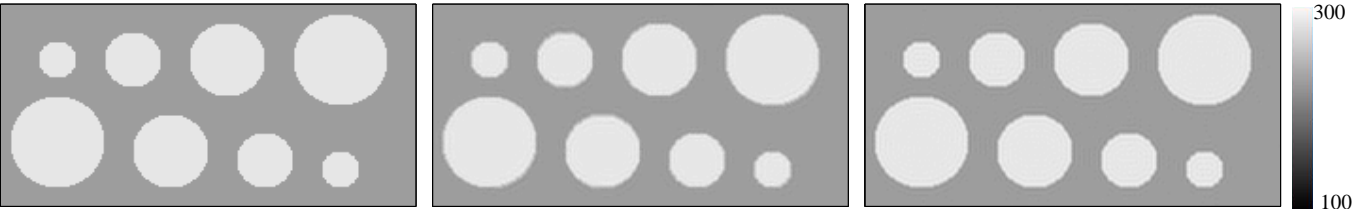


Figure 3.4: A sub image of the synthetic scene (left), the (1000-iteration) reference scene (center), and a low-pass-filtered region with band corresponding to the spatial support of the antenna reflector, or a 1.6 m diameter (right).

pass filtered synthetic image, with the frequency band hand-selected to be approximately the band of the 1000-iteration reference. Notice the reconstructed image (right) is similar to the low-pass scene (center).

3.1.4 Local Time of Day (LTOD) vs Daily Images

Images are often created using daily or bi-daily sets. In addition to having reduced spatial coverage at moderate latitudes, bi-daily or local time-of-day (LTOD) images have increased temporal resolution and decreased spatial sampling density—characteristics which impact the effectiveness of SIR.

While SIR requires spatially dense measurements, the effect of varying sampling density is nonintuitive. Assuming the scene is unchanging in time, the expected effect of combining measurements is reduced noise in the output image [11]. Also, the high sampling density with varied orientations of the aperture function—characteristics of daily sets—increases the effectiveness of image reconstruction [8]. The effect of sampling density on signal convergence for SIR is discussed after optimization of SIR parameters for both LTOD and daily images.

Because SIR assumes a temporally constant scene, temporal variation in overlapping measurements acts as injected noise, producing undesirable artifacts in the output image. Daily images combine measurements which are temporally separated by nearly 24 hours, over which time T_B can change drastically. These effects are reduced in LTOD images, where the maximum temporal gap between combined measurements is only about 7 hours, and the average temporal gap is much less [12]. The relative accuracy of LTOD versus daily images in representing transient effects such as ice edges, ice bergs, and clouds are considered in [13], which shows the benefits of using LTOD. Although in our simulation of SIR we assume a temporally-constant brightness scene, the application of SIR to actual data demonstrates this effect.

3.2 SIR Iteration

As SIR iterates, the signal over the range space of the aperture function approaches its true low-pass value. However, noise is also amplified with iteration. After many iterations, the increase in noise error may exceed the decrease in reconstruction error.

Figure 3.5 shows absolute difference images between reconstructed scenes of varying iteration number and the all-pass synthetic scene. When few iterations are used, convergence to the true scene is poor. As the number of iterations increases, the low-pass component converges quickly. After many iterations, high-frequency edges improve slightly, and noise is amplified through the high-pass nature of SIR. This behavior agrees with the discussed SIR characteristics. We use the minimum RMS error to identify the optimal number of iterations for each channel.

Figure 3.6 shows a set of images like those of Fig. 3.5, but which represent the error from the 1000-iteration low-pass reference scene. Figure 3.7 shows RMS error versus iteration using both the all-pass and low-pass (1000-iteration) reference scenes. The only noticeable difference between the all-pass (top) and low-pass (bottom) plots of Fig. 3.7 is that the reconstruction error

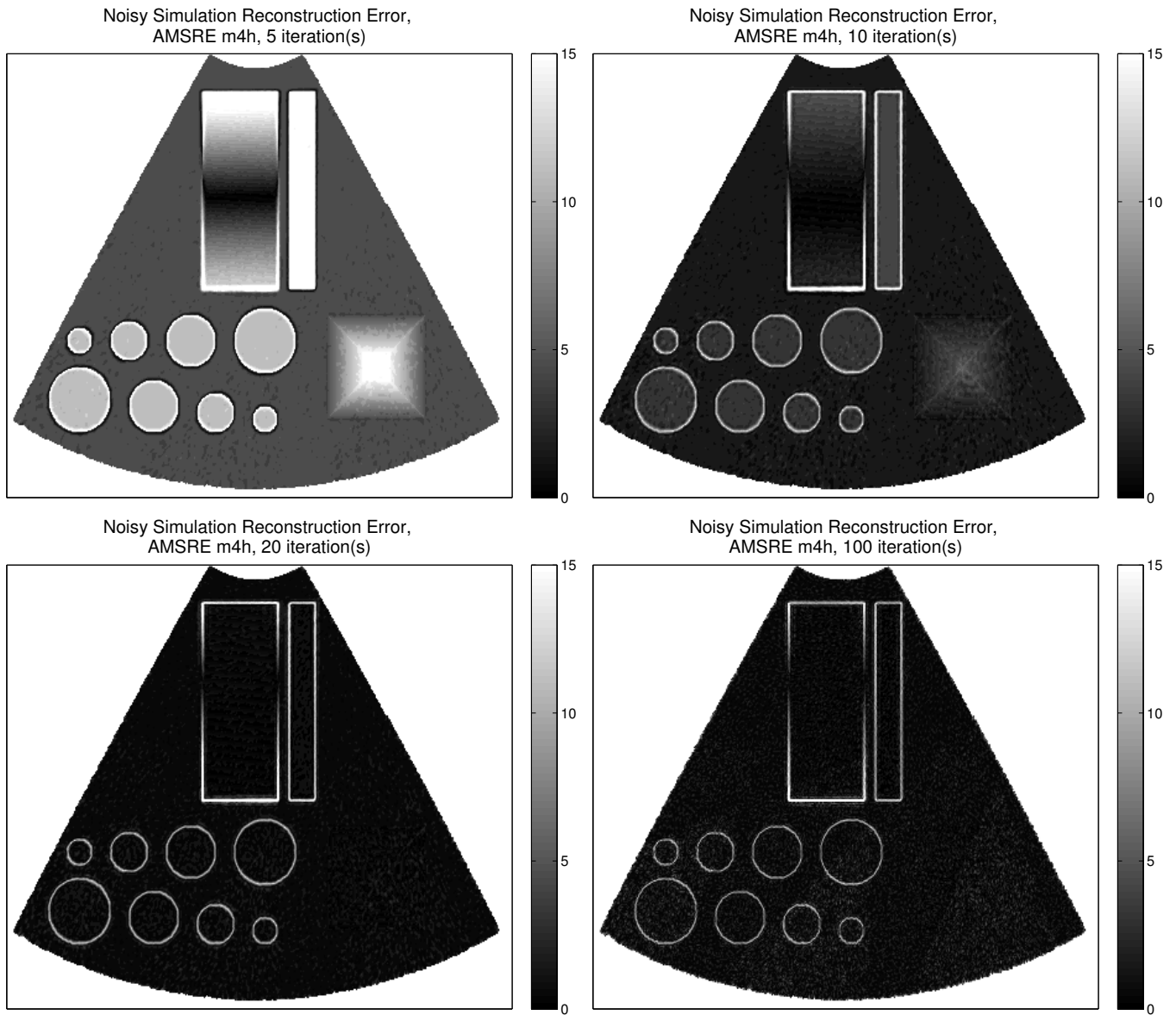


Figure 3.5: Total RMS error images for images reconstructed from simulated measurements with injected noise for 5, 10, 20, and 100 SIR iterations. Note the decrease in reconstruction error (though the edges remain apparent) and increase in noise error as iteration increases. Saturation near sharp transitions and for the 5-iteration image is expected; the color scale is chosen to highlight increasing noise amplification with iteration.

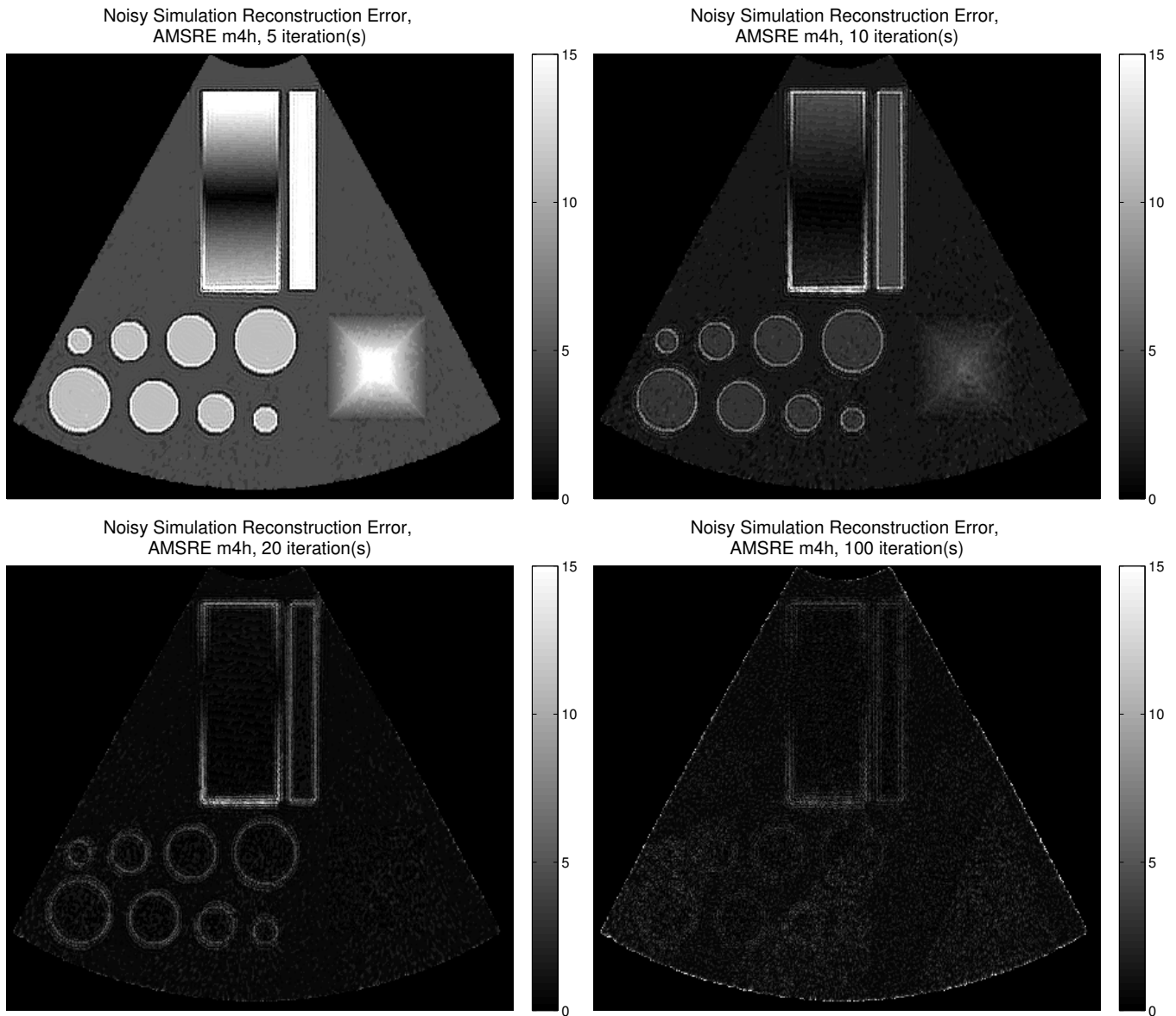


Figure 3.6: RMS error images as in Fig. 3.5, using a low-pass T_B reference scene. The reduction in error near sharp transitions (from Fig. 3.5) shows the convergence of the reconstruction to a low-pass version of the sampled brightness scene.

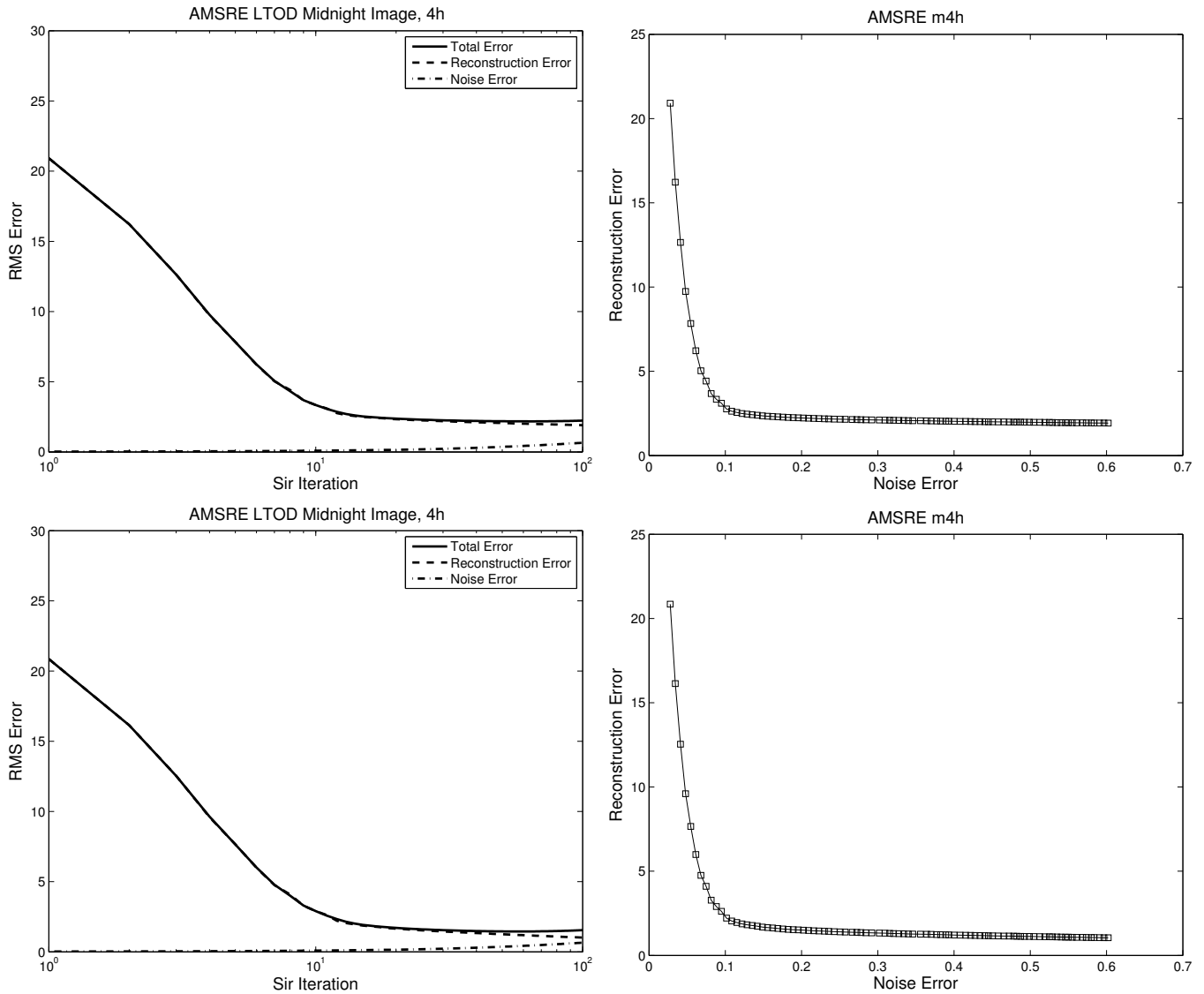


Figure 3.7: (Left) Noise, reconstruction, and total RMS error versus SIR iteration using the all-pass (top) and low-pass (bottom) reference scenes (note the log scale in the iteration axis). Reconstruction error versus noise error (right) using the all-pass (top) and low-pass (bottom) reference scenes. Note the bias in the reconstruction and total error when using the all-pass reference as opposed to the low-pass reference. The error bias represents the high-pass portion of the synthetic scene which lies in the null space of the sampling system.

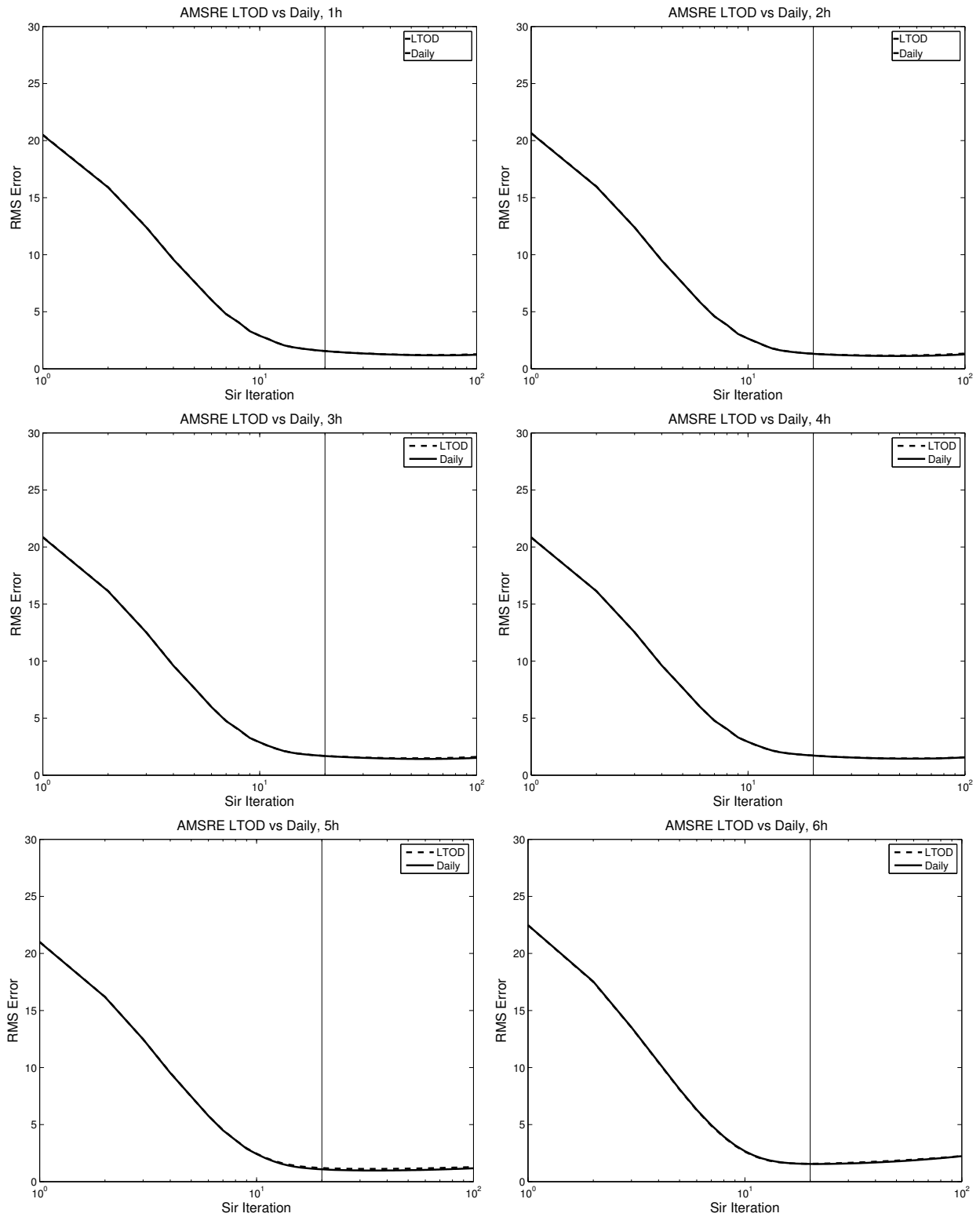


Figure 3.8: Daily and LTOD errors for each channel, using the average of LTOD simulator noise levels from Table 3.1. The vertical line is at 20 iterations, the currently-used iteration number. The LTOD error is only slightly higher than the daily error.

with respect to the all-pass reference is higher by a constant. The bias results from using an all-pass reference with a low-pass estimate. For the rest of our analysis, we use the low-pass scene as the reference.

As far as the difference between daily and LTOD reconstruction, Fig. 3.8 shows that the RMS errors are nearly identical. Only with many iterations does the LTOD error rise above the daily error. This result indicates that increasing sampling density from LTOD to daily only marginally improves error with iteration. We note that the simulation did not account for temporal variation in T_B which increases the noise in the daily image.

Figure 3.9 shows each channels' total RMS errors for various simulation noise levels. The dotted line and square marks indicate the minimum error for each noise level. Using the noise levels from Table 3.1, these results suggests that for most channels, images continue to improve after more than 20 iterations. In order to design for worst case, we use the optimal iteration corresponding to a curve of higher noise than estimated in Section 3.1.2. The used ΔT and resulting iteration numbers are found in Table 3.2.

3.3 Aperture Function Threshold

SIR threshold optimization is performed with respect to two metrics: (1) empty pixel error, or pixels within the sensor swath that are not covered by any measurement's thresholded footprint, and (2) RMS error of non-empty pixels. Computation time is also considered. We note that aperture function threshold optimization is nearly insensitive to noise, so varying the noise is unnecessary in this section.

Figure 3.10 shows plots of the two error types and processing times with decreasing threshold for each channel. The increase of computation time is nearly linear with decreasing (log-scale) threshold, so the maximum threshold which gives acceptable results is chosen. We require that the selected thresholds have no "empty-pixel" error and that the RMS error is within a few percent of their minimum. The resulting threshold values are listed in Table 3.2. Errors for daily sets are included in Fig. 3.11. Because the entire study region is covered by at least two scans (Section 2.6), the empty-pixel error is decreased dramatically.

There are a couple reasons for using the LTOD-optimized values for the daily set. First, there is not bi-daily coverage for regions nearer the equator. This means that LTOD-optimized

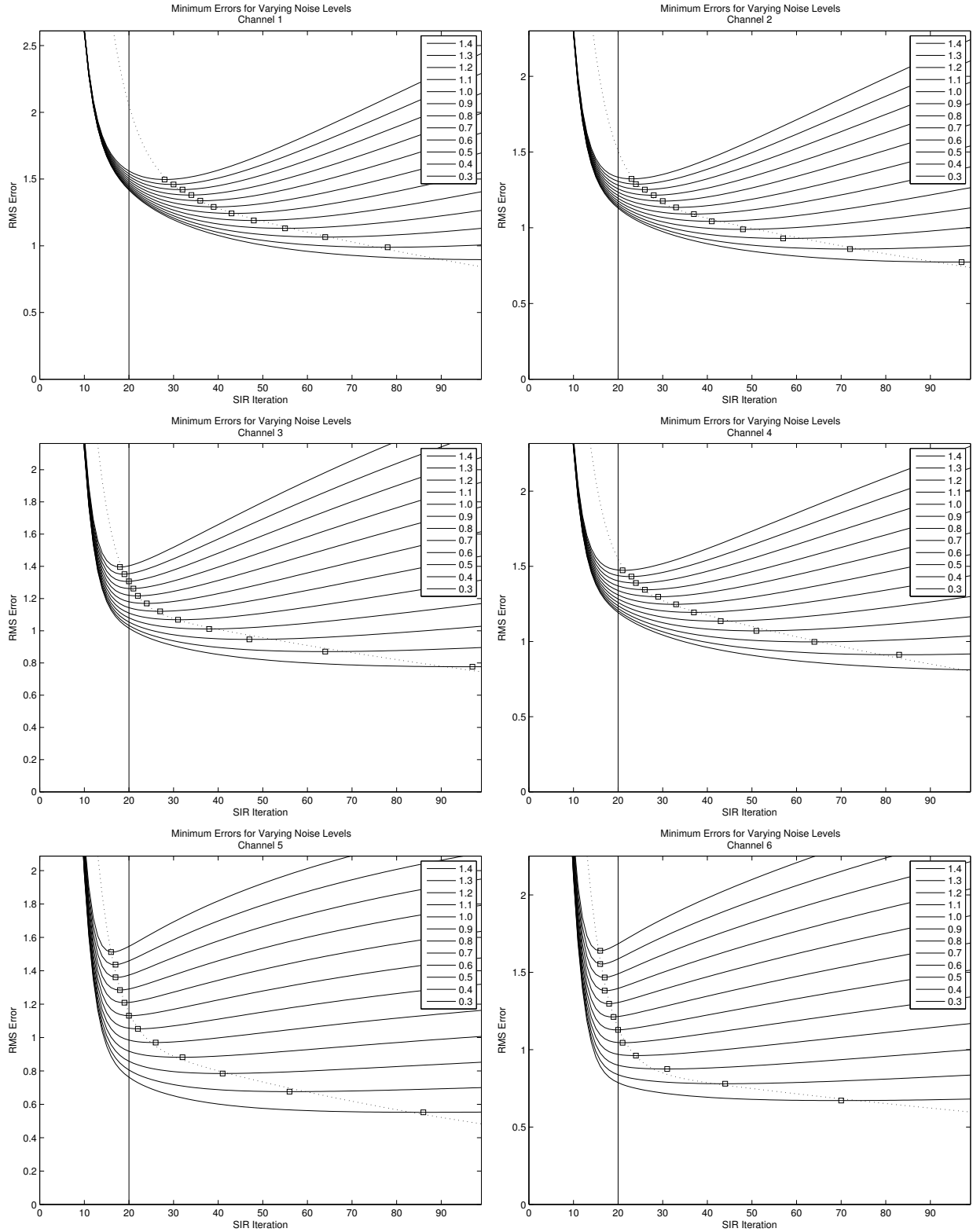


Figure 3.9: RMS error versus SIR iteration for varying noise levels for all channels. In each plot, the graph shows the RMS error with noise standard deviation ΔT ranging from 0.3 to 1.4, with lower noise levels corresponding to lower RMS errors. The dotted line is a fit to the minimum errors for each ΔT , whose actual values are marked with squares.

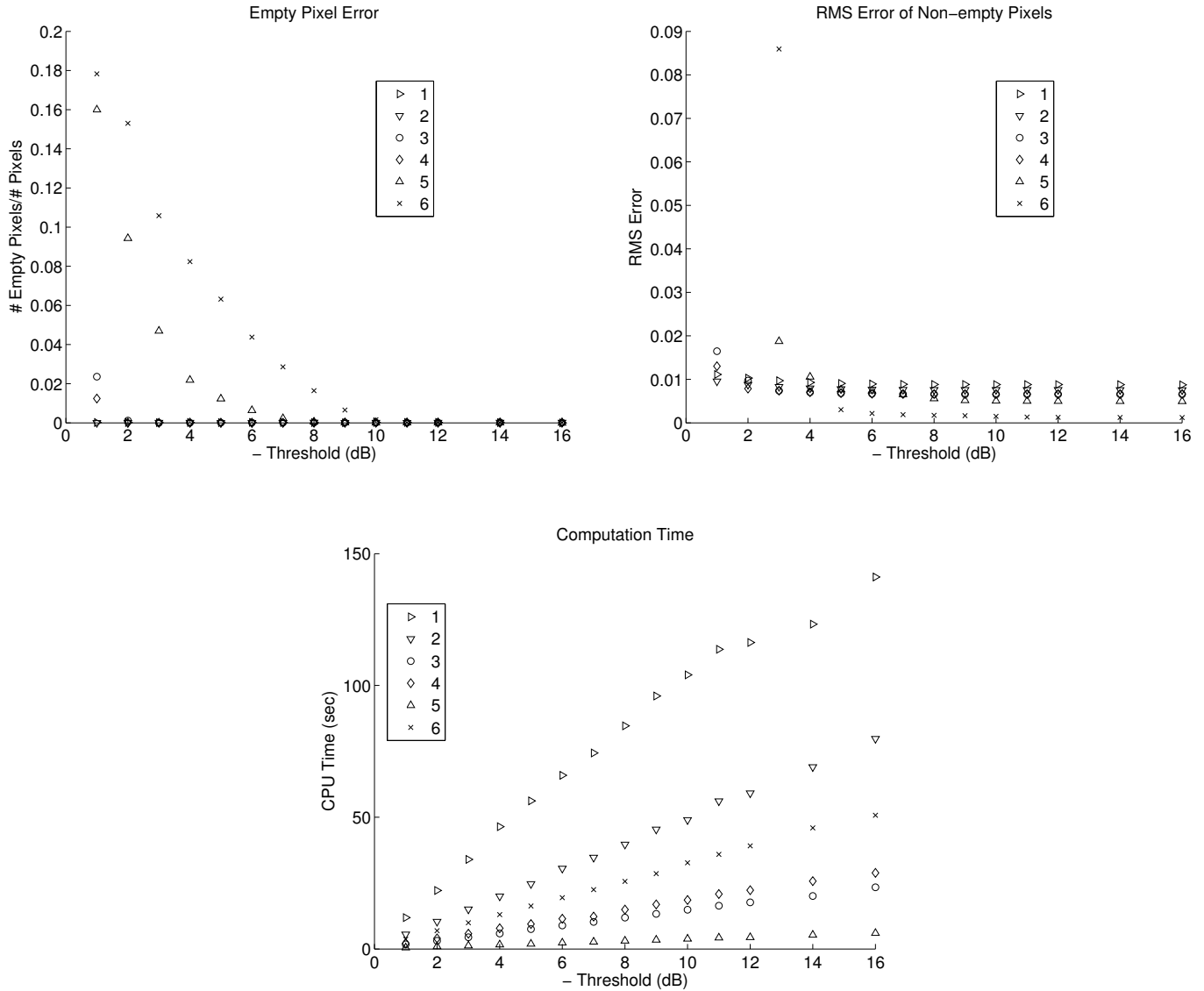


Figure 3.10: Plots of the two error types and computation times with decreasing threshold for each channel. In general, channels with larger antenna footprints (frequencies 1 and 2) or more measurements (frequency 6) take longer to process.

thresholds are required over these regions to eliminate empty-pixel error. Second, while sampling over the near-polar regions eliminates empty-pixel error for the complete image, individual swaths have decreased sampling density and resulting gaps in coverage. The contrasting values of the individual swaths are not averaged where one has empty pixels, so the effects of temporal change between swaths are accentuated for thresholds which are too high. For these reasons we recommend LTOD-optimized thresholds for daily processing.

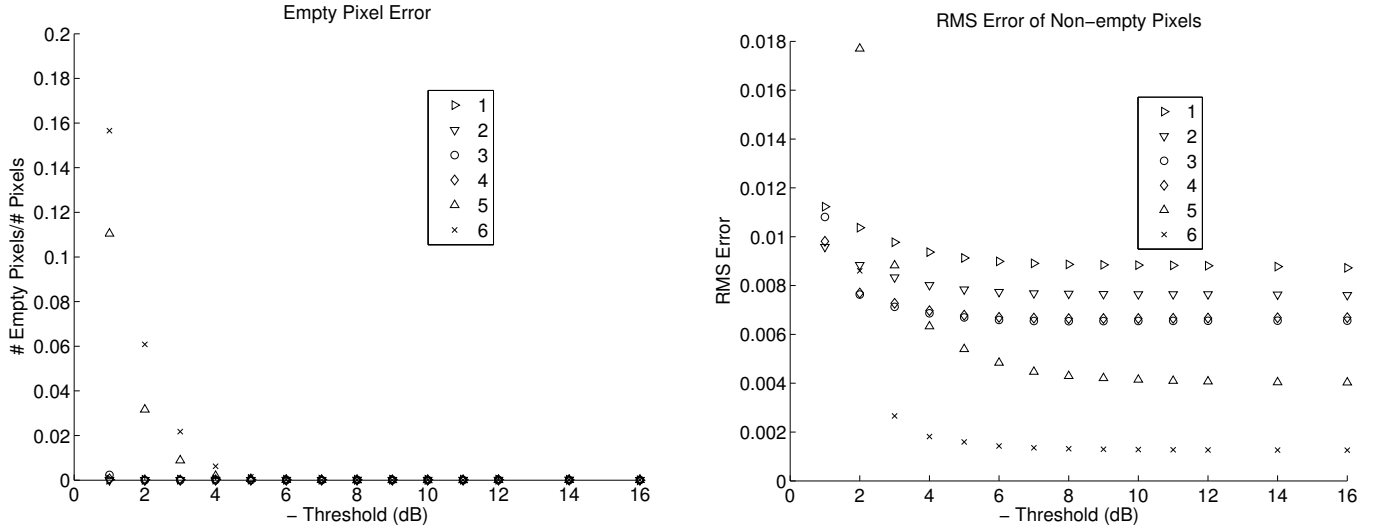


Figure 3.11: Plots of the empty-pixel error (left) and RMS error (right) for daily sampling versus threshold.

Table 3.2: Tuned SIR iteration numbers and thresholds for each channel.

	Frequency Channel					
	1	2	3	4	5	6
Assumed ΔT	0.7	0.8	0.9	1.0	1.0	1.2
SIR Iteration	47	37	23	28	18	17
SIR Threshold	-6	-7	-8	-8	-10	-13

3.4 Conclusion

The values in Table 3.2 represent the parameters' tuned values based on our criteria. From Fig. 3.9, it is apparent that for most channels, small variation from the optimal iteration number results in a very small increase in error. This is true for the lower frequencies in particular. However, the currently used 20-iteration value is outside this insensitive region for at least channels 1 and 2.

For the threshold parameter, acceptable values are more restrictive, at least if errors associated with empty pixels and the aperture function spatial-limit are to be avoided. Problems with quantization and the spatial limit could be reduced if SIR were changed to have a larger or finer aperture function grid, although this would increase computation. Chapter 5 presents actual T_B images with the tuned SIR parameters.

CHAPTER 4. AMSR-E APERTURE FUNCTION ESTIMATION

This chapter presents a method which estimates the aperture function of an operational satellite-based radiometer using T_B measurements from the instrument over a region of known geographic composition. First, the mathematical formulation of the method is presented, including discussion of the selected geographic region. A aperture function model is also suggested for noise reduction. Second, the method is applied to simulated measurements. Third, actual data is used. Last, we use the aperture function estimate in SIR processing and compare resulting T_B images to those which used the previous Gaussian approximation.

4.1 Formulation

This section presents a mathematical formulation which approximates AMSR-E sampling and a method for obtaining an estimate of the aperture function. It also discusses the choice of geographical region over which to perform the estimate and some additional considerations on the choice of models for the spatial aperture response function.

4.1.1 Mathematical Formulation

Each T_B measurement can be represented as an inner product of the aperture function and the Earth's T_B distribution. Because the aperture function is low pass, the T_B measurements are also low-pass. As discussed in the Section 2.6, image reconstruction techniques attempt to invert the effect of the inner product of the T_B scene with the aperture function in order to obtain a T_B estimate. On the other hand, our aperture function estimation procedure is to invert the effect of the inner product of the aperture with the Earth's T_B to recover an estimate of the aperture function. This is complicated by noise and temporal variability of the T_B of the Earth's surface.

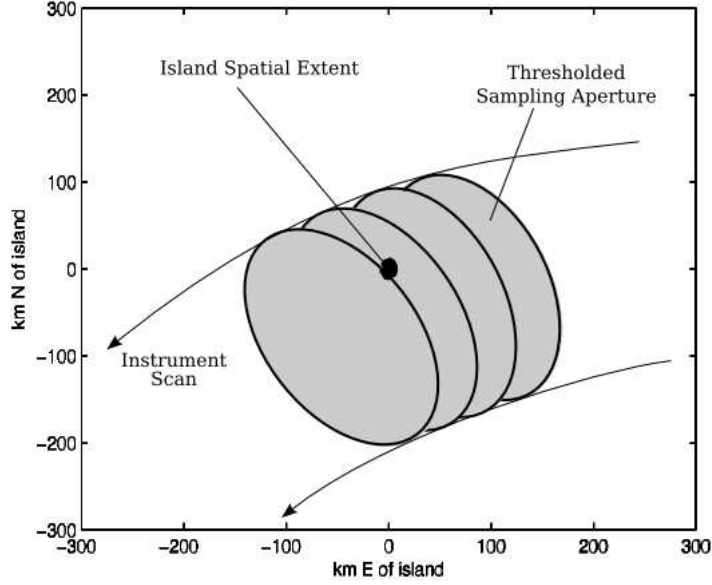


Figure 4.1: Diagram showing the location and rotation of five 6 GHz sample footprints at a ten-sample interval. The gray areas indicates roughly the -30dB -thresholded aperture functions while the black spot indicates Niue island.

Neglecting noise, we let g represent the Earth's T_B and h represent the aperture function. A T_B measurement y_n is given by

$$y_n = \int g(\vec{v}) h(\theta_n, \vec{x}_n, \vec{v}) d\vec{v} \quad (4.1)$$

where θ_n and \vec{x}_n are the rotation and center location of the aperture function, respectively. The vector \vec{v} describes the displacement from the center of the aperture function. We assume that rotations of h only effect its orientation, not its shape, and that measurement location has no effect on the shape or orientation of h . With a change of variables, Eq. 4.1 may be represented as the convolution of the Earth T_B scene and the aperture function. However, the inner product form is more convenient, especially if we perform shifts and rotations on g instead of h to compensate for the movement of the aperture function:

$$\int g(\theta_n, \vec{x}_n, \vec{v}) h(\vec{v}) d\vec{v} = y_n. \quad (4.2)$$

Although infinite in spatial extent, the aperture function h contains nearly all its power in its spatially-limited main lobe. The infinite integral can then be reasonably approximated by an integral over some spatially-limited region C containing h 's main lobe,

$$\int_{\vec{v} \in C} g(\theta_n, \vec{x}_n, \vec{v}) h(\vec{v}) d\vec{v} = y_n. \quad (4.3)$$

Although h is low-pass, g is in general all-pass. A low-pass version of g may be used in a discrete representation of the above equation. The low-pass restriction is necessary to satisfy the Nyquist criterion for g , but with a grid much finer than the aperture function main lobe, the frequency band containing h is unaffected. Thus, the integral can be approximated by a sum over a P -sample grid with sufficiently small spacing in relation to the main lobe of h ,

$$\sum_{p=1}^P g(\theta_n, \vec{x}_n, \vec{v}_p) h(\vec{v}_p) \Delta v, \quad (4.4)$$

with \vec{v}_p describing the P sampling locations over the aperture. The constant Δv is the area of each rectangular grid element for the discretization.

The sum in Eq. 4.4 can be represented as a discrete inner product of two vectors, \mathbf{g}_n and \mathbf{h} ,

$$\begin{aligned} \mathbf{g}_n^T \mathbf{h} &\approx y_n, \\ \mathbf{g}_n &= [g(\theta_n, \vec{x}_n, \vec{v}_1) \ g(\theta_n, \vec{x}_n, \vec{v}_2) \ \dots \ g(\theta_n, \vec{x}_n, \vec{v}_P)]^T, \\ \mathbf{h} &= [h(\vec{v}_1) \ h(\vec{v}_2) \ h(\vec{v}_3) \ \dots \ h(\vec{v}_P)]^T. \end{aligned}$$

An N -length sequence of T_B measurements at slightly different locations can be represented as a vector \mathbf{y} , where \mathbf{y} is given by,

$$\begin{bmatrix} \mathbf{g}_1^T \\ \mathbf{g}_2^T \\ \vdots \\ \mathbf{g}_N^T \end{bmatrix} \mathbf{h} = \mathbf{Gh} \approx \begin{bmatrix} y_1 \\ y_2 \\ \vdots \\ y_N \end{bmatrix} = \mathbf{y}. \quad (4.5)$$

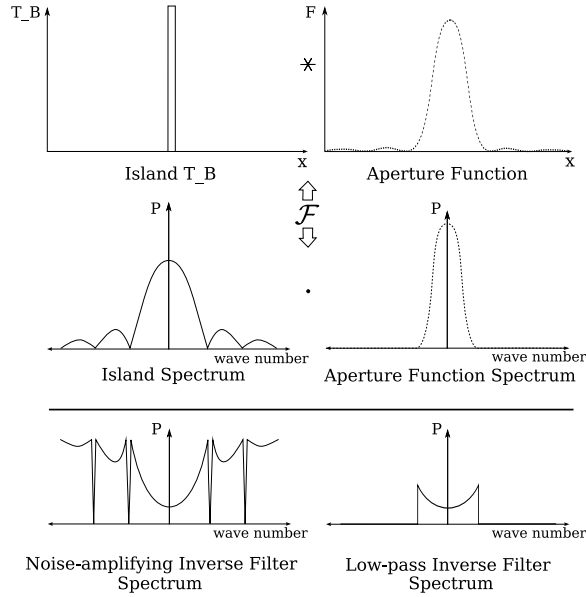


Figure 4.2: A 1D representation of the island T_B (top left) and the aperture function (top right) and the spectrum of each (middle left and right, respectively). The frequency response of the full inverse filter (bottom left), and a low-pass equivalent over the sampling aperture support (bottom right).

The aperture function estimation problem can thus be reduced to a matrix inversion. The matrix G can be thought of as a convolution matrix for the irregular-sampled aperture-filtered problem.

The geographic region can be chosen such that the frequency support of \mathbf{h} is excluded from the null space of G . We impose this condition so that \mathbf{h} is attainable by applying a pseudo-inverse of G to Eq. 4.5. The next section discusses the selection of the region under this condition, in addition to signal-to-noise ratio (SNR) considerations.

4.1.2 Geographic Region and Implications

While the function g is not known exactly, it can be approximated over a region of known geographical composition. An island is an excellent target for various reasons. First, the island scene can be modeled by an oval island of constant T_B in an ocean background. Second, the high contrast in T_B between the island and ocean improves SNR. Third, if the island dimensions are much smaller than the aperture function main lobe, the frequency-band requirement for G is satisfied. However, the smaller the island, the lower the effective SNR of the aperture function estimate.

The dominant noise affecting our estimation problem is caused by the temporal changes in the brightness scene which are unaccounted for in the supposed sampling model and brightness scene. Even at lower frequencies where the atmospheric contamination is small, weather phenomena are often responsible for T_B changes associated with ocean surface roughening. Noise effects are reduced by using a large data set—available over the several-year AMSR-E mission—and by hand-selecting days over which T_B measurements indicate favorable weather conditions.

The expected quality of aperture function estimate changes for each channel. In general, lower frequencies are less sensitive to atmospheric effects. Lower frequencies also have larger antenna patterns. This is useful in our problem, yielding more samples over the aperture function main lobe and the ability to use a larger island (see Eq. 4.9), which improves SNR. H-pol channels have better land/ocean contrast, which also improves SNR. Because of these factors, we expect the best estimates to be for lower-frequency and h-pol channels.

In order to simplify the estimation problem, the matrix G can be decomposed as

$$\mathbf{G}\mathbf{h} = (\mathbf{G}_i + \mathbf{G}_o)\mathbf{h} = \mathbf{y}_i + \mathbf{y}_o = \mathbf{y} \quad (4.6)$$

where G_i and G_o are the brightness temperatures over the island and over the ocean, respectively.

Because we are sinc-sampling the island, small-scale variations in T_B are filtered out; therefore, if the island is nearly uniform in terrain and vegetation or if the variation is small-scale, we can assume the island T_B is constant with space. Although not constant from swath to swath, any change in mean island T_B would only affect the magnitude scale of the estimate, not the shape of the aperture. In our estimation, we normalize the power in each pass over the island in order to mitigate this possible scaling.

The ocean T_B is not nearly as constant in time nor space. For simplicity, measurements that are not within about the 6dB aperture function footprint are assumed to be purely ocean, and the ocean signal near the island is estimated using a least-squares spatially-varying quadratic fit over purely-ocean measurements. The second-order term and often the first-order term in this fit are quite small, but we include them both to match banded changes in ocean T_B attributed to surface temperature or roughness variations.

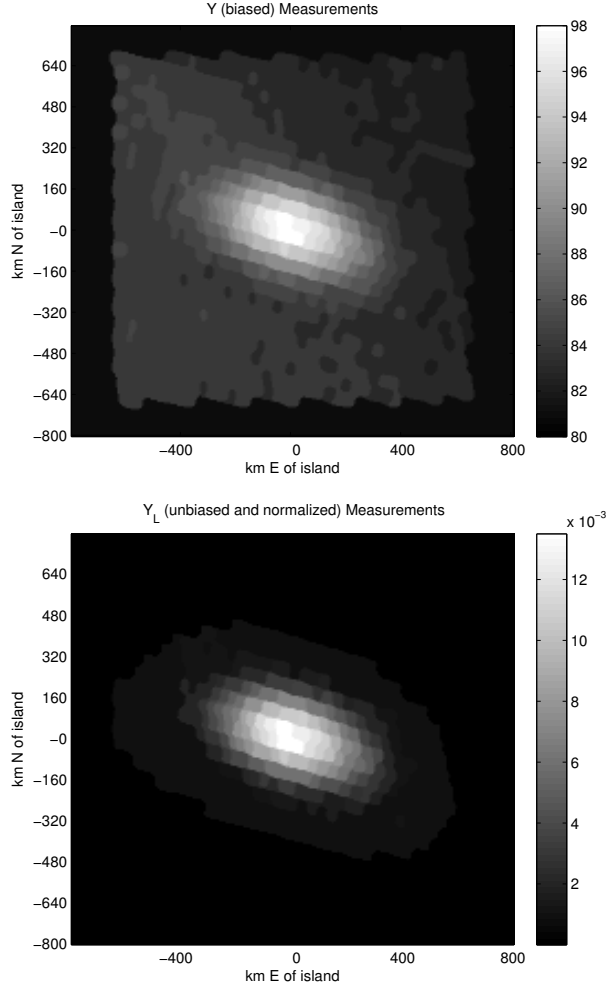


Figure 4.3: (Top) Actual measurements over Niue island. (Bottom) An approximation of y_L , or land-only measurements. A quadratic fit over the ocean-only measurements is used to determine the ocean contribution to the island-affected measurements.

Because G_o changes with time, we estimate it for each swath and modify the problem to be

$$\mathbf{G}_i \mathbf{h} = \mathbf{y} - \hat{\mathbf{y}}_o = \mathbf{y}_i. \quad (4.7)$$

A pseudo inversion of this linear system gives an estimate of the aperture function:

$$\hat{\mathbf{h}} = \mathbf{G}_i^\dagger \mathbf{y}_i. \quad (4.8)$$

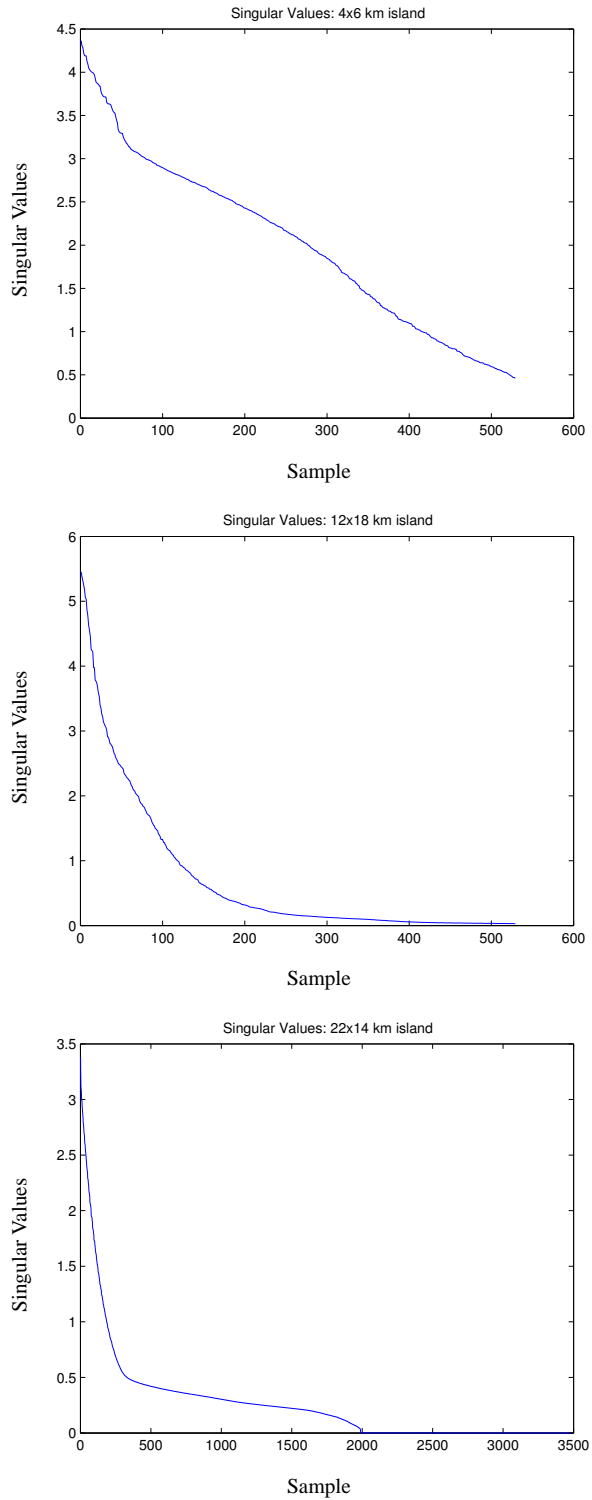


Figure 4.4: Singular values for islands with axes dimensions 4x6 km (top), 12x18 km, and 22x14 km (bottom). G-matrices associated with smaller islands are less singular. The x-axis scale is different for the largest island because more measurements of high SNR are found near that island due to high island signal power.

A near-elliptical island with an assumed-constant T_B has a 2-dimensional sinc-like spectrum. For a very small island, the first nulls in the spectrum are not contained in the band containing the aperture function's spectrum, therefore no part of any possible aperture function is in its null space. Smaller islands also have less signal power. While giving higher signal power, a very large island may have spectral nulls over the aperture function's spectral support, making its recovery impossible.

As discussed in Appendix A, the aperture function spectrum can be expressed in the spatial domain, its support limited to an area approximately the size of the antenna reflector. The island can be thought of as an antenna with a far field power distribution in the same plane as the aperture function equivalence current. For our problem, we require that the 5dB far-field beam width of the island at the equivalence current plane be about the size of the the AMSR-E antenna reflector.

A uniformly-illuminated circular antenna produces an Airy pattern power density distribution, which has a half-power beam width β of approximately $0.5\lambda/a$, with a the diameter of the circular antenna and λ the channel wavelength. In the reflector plane, the half-power beam width is about $R_0\beta$, with R_0 , the target range. The diameter d of the half-power beam width at the Earth's surface is then related to the reflector diameter a by

$$a \approx \beta R_0 \approx \frac{0.5\lambda}{d} R_0 \quad (4.9)$$

or

$$d \approx \frac{0.5\lambda}{a} R_0. \quad (4.10)$$

With the reflector diameter $a = 1.6$ m, d is about 17 km for the 6.8 GHz channel. The values of d for other channels are located in Table 4.1.

Although we have made the simplification in our calculations, note that the antenna reflector is not in the broadside of the island. The non-broadside main beam is wider than that of broadside, so if we select the island size according to our simplified calculations, our criterion is still satisfied. For higher frequency channels, smaller islands are needed.

Table 4.1: Islands selected for each channel.

Ch.	F_c (GHz)	λ (m)	d (km) (Eq. 4.9)	Island	Island Size (km)	Island Location	
						Lat.	Lon.
1	6.925	4.3×10^{-2}	17	Niue	22 x 14	19°3'S	169°51'W
2	10.65	2.8×10^{-2}	11	Rarotonga	8 x 12	21°14'S	159°46'W
3	18.7	1.6×10^{-2}	6.2	Mauke	6 x 4.5	20°10'S	157°21'W
4	23.8	1.3×10^{-2}	4.8	Mauke	6 x 4.5	20°10'S	157°21'W
5	36.5	8.2×10^{-3}	3.2	Mauke	6 x 4.5	20°10'S	157°21'W
6	89.0	3.4×10^{-3}	1.3	Takutea	1 x 2.2	19°48'S	158°19'W

The islands we selected for each channel are shown in Table 4.1. They were chosen for being relatively uniform in terrain and vegetation, and having sizes which correspond to an attenuation of less than about 5dB maximum over our estimation spectrum. The results in Section 4.2 show that this limit is acceptable. Estimation for channel 6 is omitted because the signal of Takutea and other islands of similar size is too small for our estimation. Channel 4 is highly sensitive to atmospheric water vapor, making the estimation impractical for it as well.

4.1.3 Models

The solution of the convolution matrix equation (Eq. 4.8) yields a least-squares error (LSE) estimate for our aperture function, \hat{h}_{LS} . The smaller singular values of G_i correspond to higher frequencies which are attenuated by its sinc-like spectrum as described in Fig. 4.2. The noise in the measurements is amplified when G_i is inverted, particularly in the higher frequencies. Our desired signal, the aperture function, is low-pass. As a result we can use low-pass filtering to increase the SNR by reducing the noise in the high-frequency band without adversely affecting the signal. Although singular value normalization accomplishes a similar improvement, we choose a low-pass filter as more appropriate because of the bandwidth corresponding to the spatial support of the AMSR-E reflector equivalence current.

We recognize that the representation in Fig. 4.2 is not entirely applicable to our problem; because the AMSR-E samples are irregularly spaced and its aperture function rotates, its sampling operation cannot be precisely represented by multiplication of spectra. A similar but more complicated analysis is required unless it is assumed that the regularly-sampled spectrum analy-

sis is sufficient. We assume the simpler spectra-multiplication model holds, validating the results through the simulation in Section 4.2.

While low-pass filtering can reduce the noise in the estimate, using a closed-form model may further reduce the noise. A model can be chosen to also be easily evaluatable on a continuous domain. As discussed in Chapter 2, the designed taper on the reflector dish illumination is \cos^n , a power-cosine. The power-cosine model assumes an equivalence current $J(y, z)$ near the antenna reflector of the form

$$J(y, z) = \cos^n(\sqrt{(a_1^2 z^2 + a_2^2 y^2)} + bz + c_1 z + c_2 y), \quad (4.11)$$

with parameters a_1 , a_2 , b , c_1 , and c_2 to be found for each channel. This model assumes the aperture function is the phase-scaled Fourier transform of $J(y, z)$ (see Appendix A). Although the azimuth blur caused by the movement of the antenna is unaccounted for in this model, the flexible model is shown to effectively compensate for it in the estimated parameter values.

In order to simplify the aperture function estimate for use in SIR, we also consider a Gaussian model similar to Eq. 2.2, but with an additional cross-term ξ and spatial shift terms γ_1 and ζ_1 :

$$h'_G(\gamma, \zeta) = 2^{-[(\frac{\gamma-\gamma_1}{\gamma_0})^2 + (\frac{\zeta-\zeta_1}{\zeta_0})^2 + \xi(\gamma-\gamma_1)(\zeta-\zeta_1)]}. \quad (4.12)$$

The addition of the cross-term ξ is equivalent to allowing a rotation of the aperture footprint as shown in Appendix B. The difference between this Gaussian and the power-cosine model is shown in Section 4.2 to be a fraction of a percent at most. We conclude that the modified Gaussian model in Eq. 4.12 is a sufficiently accurate substitution for the power-cosine model for use in SIR. Appendix B also shows that this model is represented in Earth-surface coordinates. Finding the power-cosine and Gaussian model parameters from the LSE is a non-linear estimation problem, solved by a Levinson-Durbin recursion.

4.2 Simulation

Before applying the proposed method to actual data, we simulate AMSR-E sampling using a presumed power-cosine aperture function and a synthetic T_B scene. Measurements are taken at

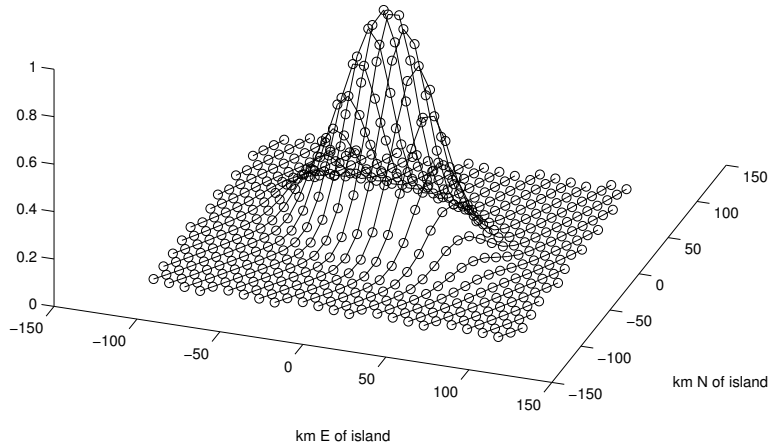


Figure 4.5: Plot of noiseless simulated land-only measurements over a Niue island, limited to one swath. Each line represents one AMSR-E scan, with each circle representing a measurement. Both the island power and the aperture function are normalized.

locations and with rotations on the aperture function based on real AMSR-E sampling, as shown in Fig. 4.1. Using the simulated measurements with added noise, we estimate the aperture function and compare it with the original. The synthetic T_B is an oval-shaped island in a low-level ocean background, with dimensions similar to those in Table 4.1 for each channel.

To create simulated AMSR-E measurements, we create a fine grid over a spatially limited approximation of the aperture function. The spatial-limit approximation excludes values below about -30dB . The shifts and rotations dictated by AMSR-E data causes varying numbers of grid points to be either island or ocean grid points (see Fig. 4.1). The island signal is spread equally across all island grid points by normalizing the grid point weights by the number of island points in the inner product approximation. Resulting measurements, limited to one swath, are shown in Fig. 4.5.

After obtaining the synthetic measurements, the estimation process is implemented as proposed in the previous section, with parameters such as grid spacing and size independent of those used during synthesis. The results for the no-noise simulation of channel 1 are shown in Figs. 4.6 and 4.7. Notice that for the \cos^n and Gaussian models, the estimates are displayed on a finer grid. This is because after the parameters of these models are computed on the coarse grid, the estimates can be easily plotted on an arbitrarily fine grid. The LS spectrum and LPF solution are on a finer grid due to pre-FFT padding.

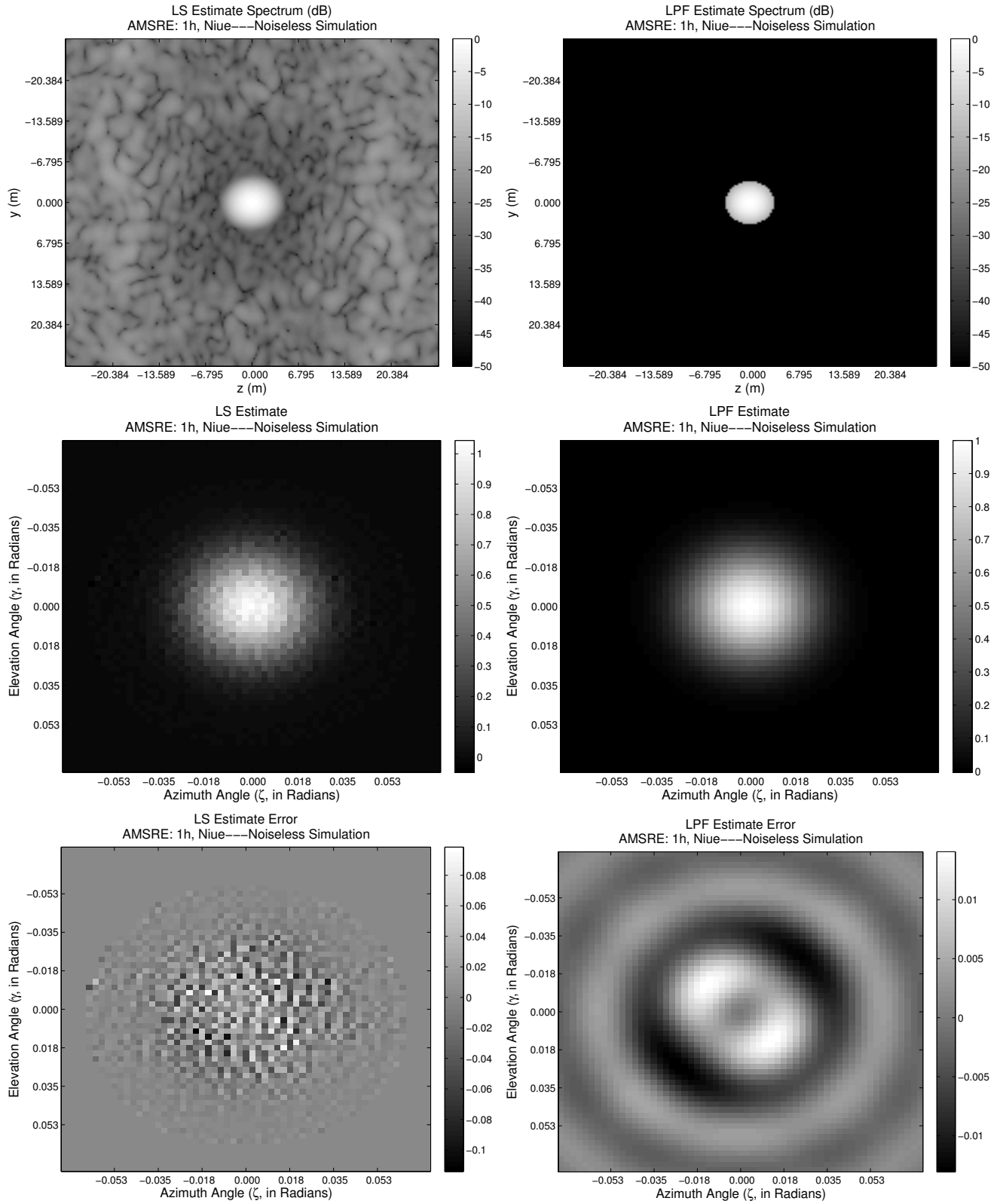


Figure 4.6: LS (left) and LPF (right) aperture function estimates for noiseless simulated measurements.

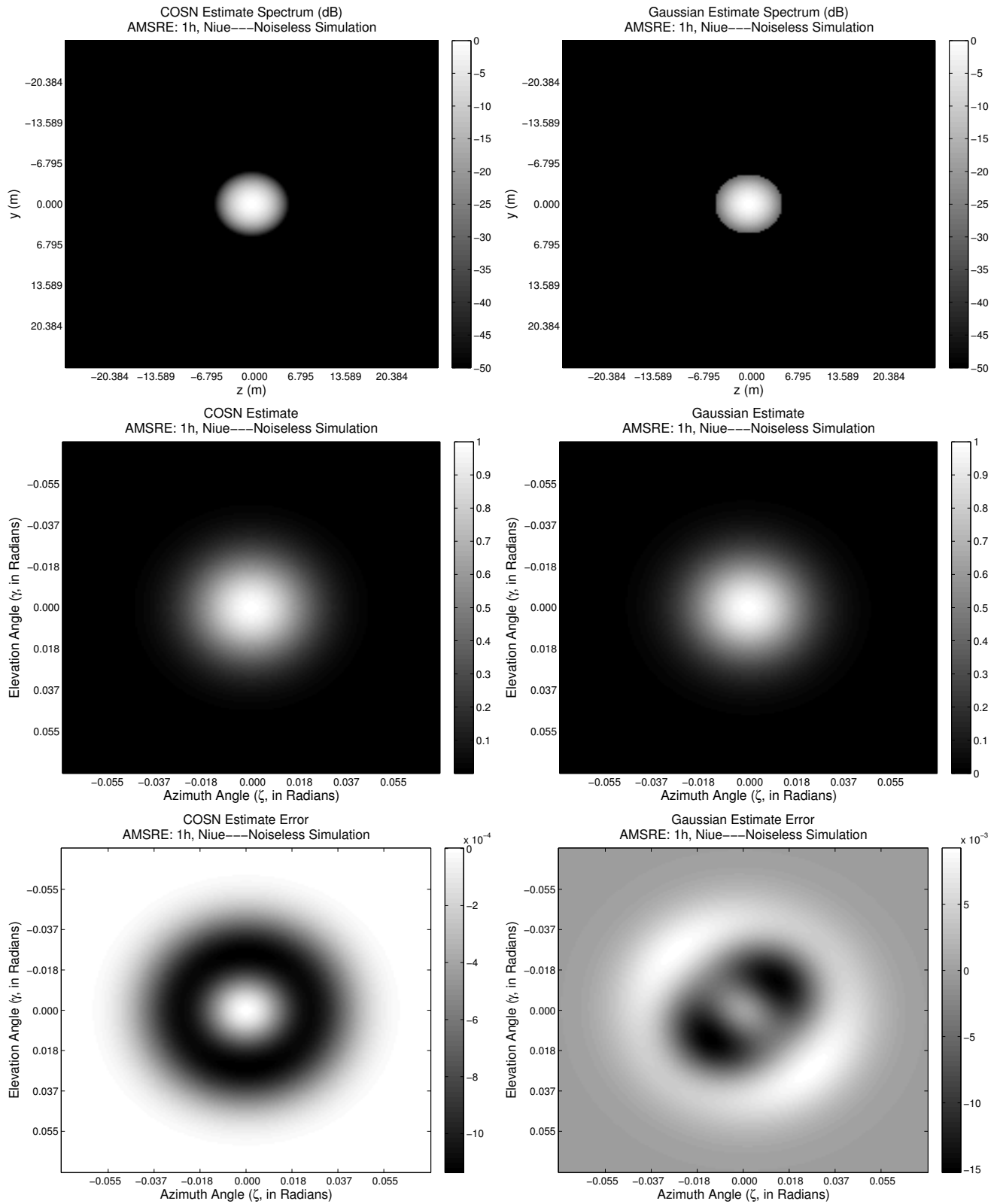


Figure 4.7: Power-cosine and Gaussian model solutions for the noiseless simulation.

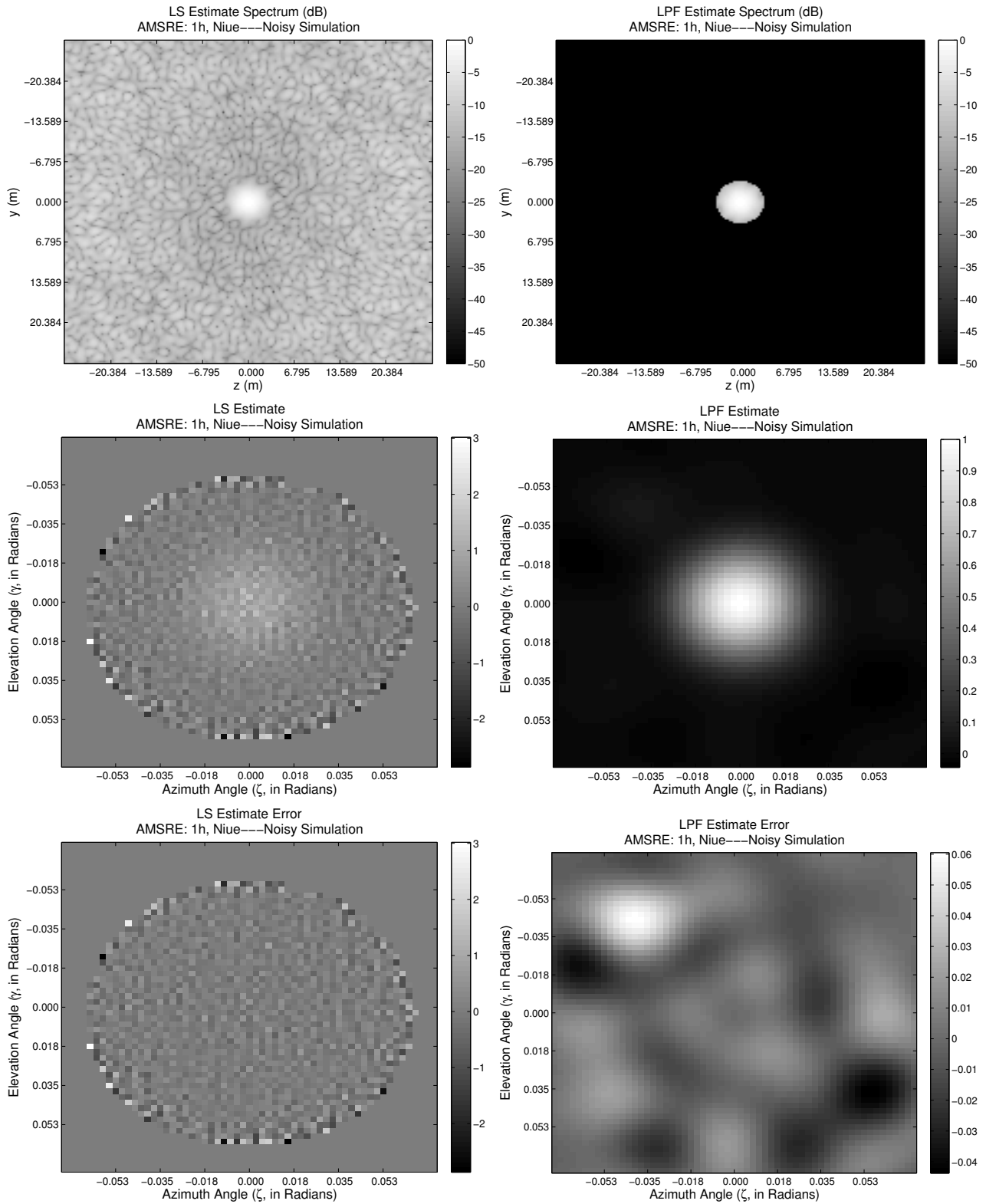


Figure 4.8: Channel 1 LS and low-pass model solutions for noisy simulation.

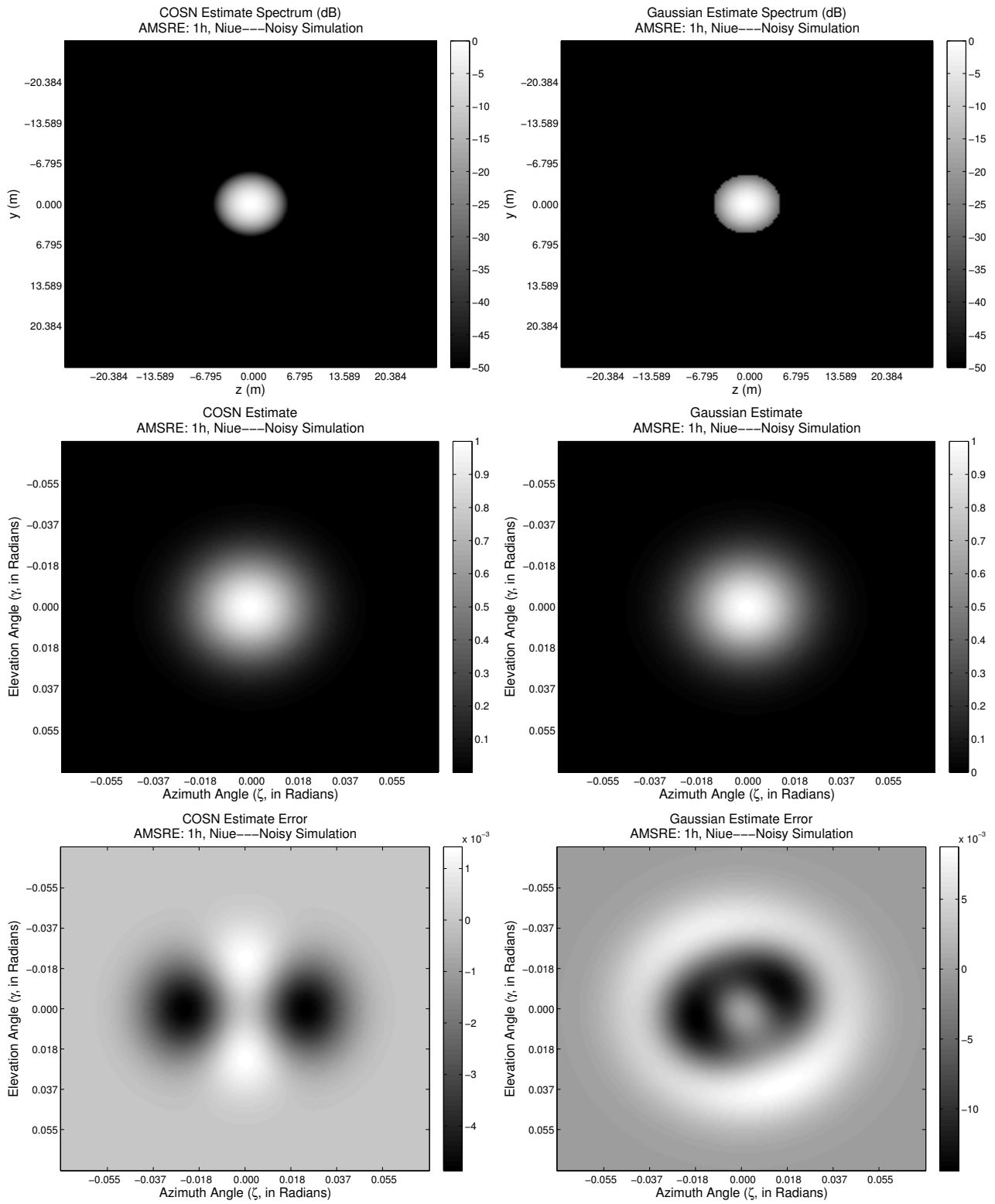


Figure 4.9: Channel 1 Power-cosine and Gaussian model solutions for noisy simulation.

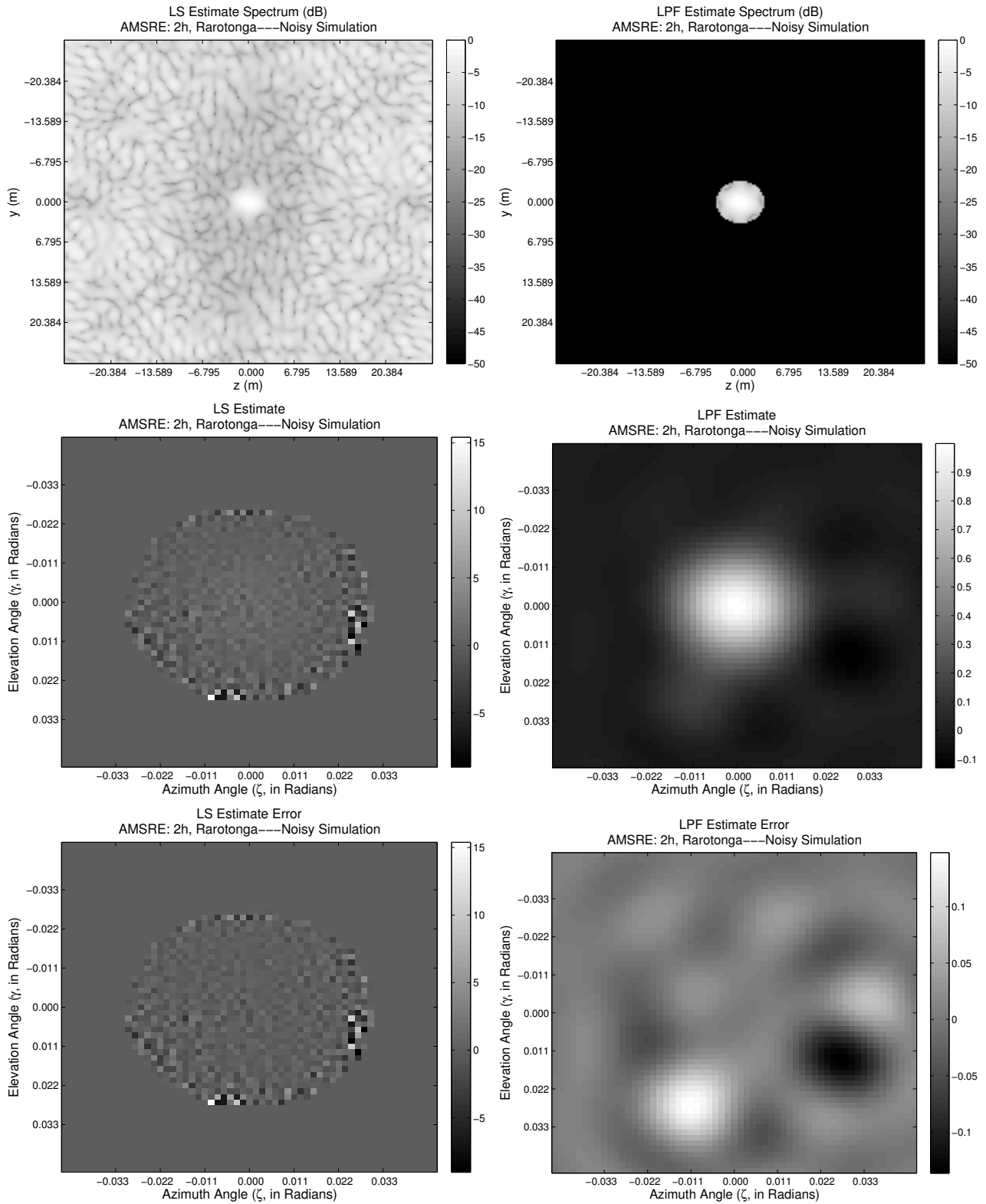


Figure 4.10: Channel 2 LS and low-pass model solutions for noisy simulation.

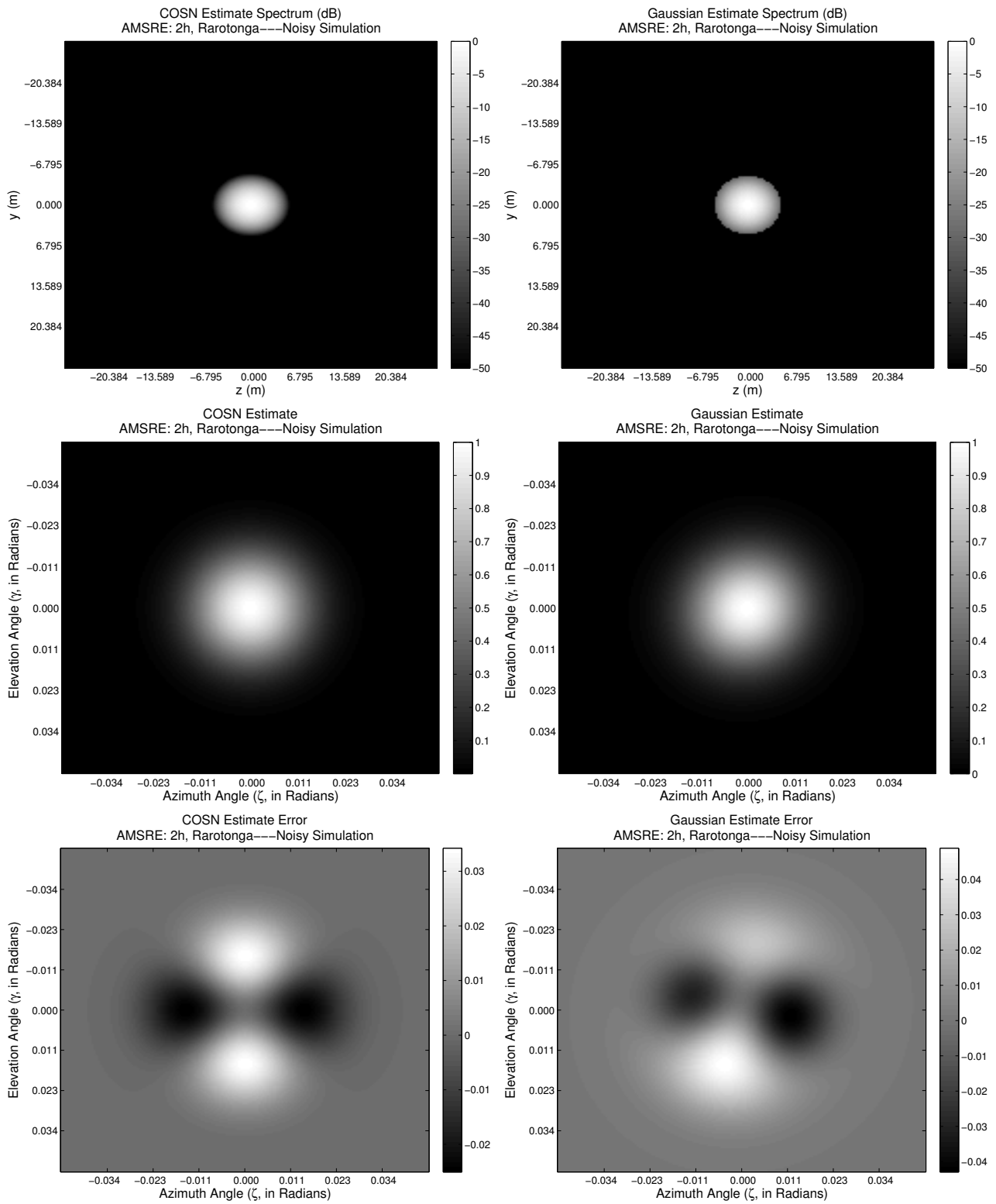


Figure 4.11: Channel 2 Power-cosine and Gaussian model solutions for noisy simulation.

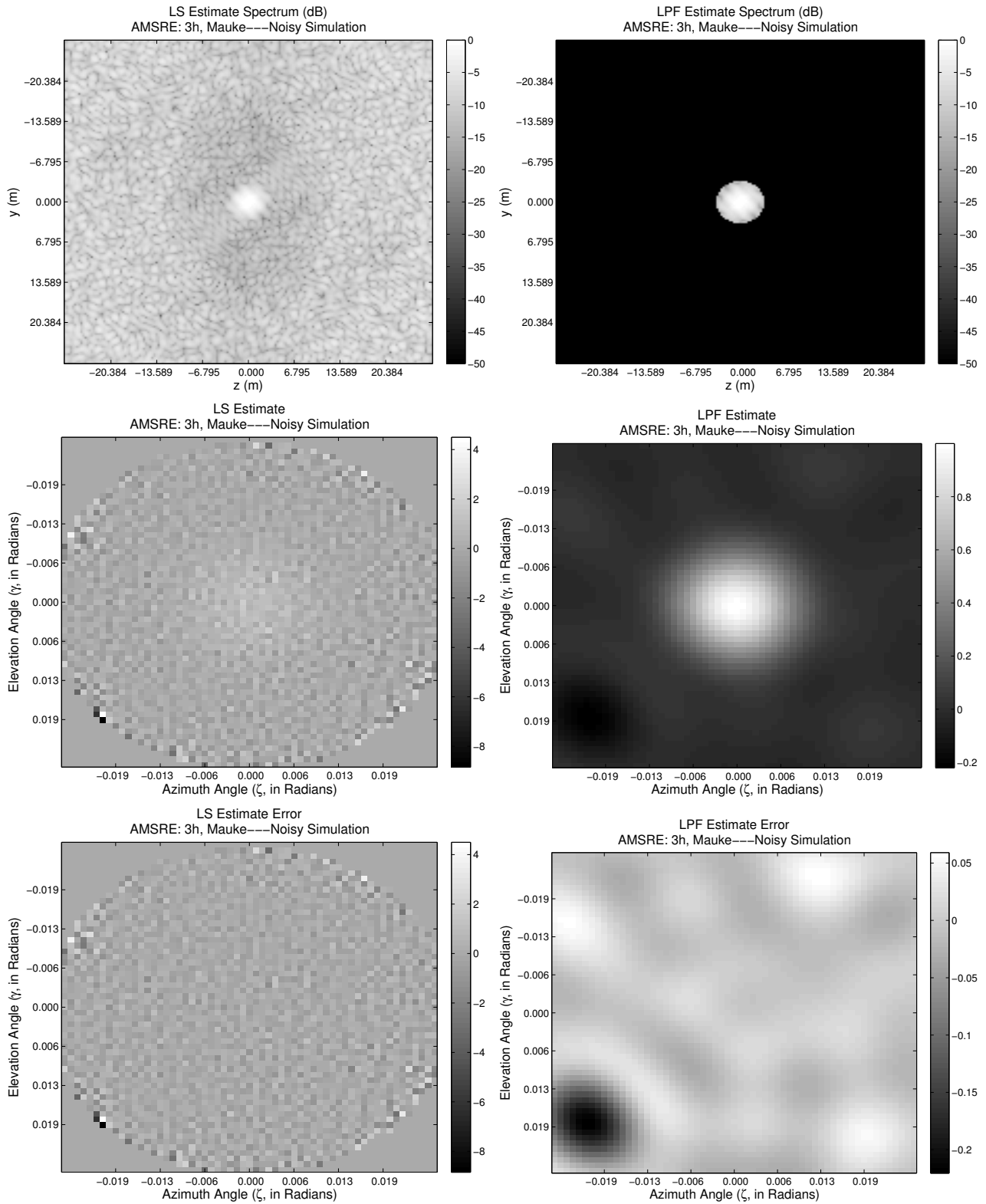


Figure 4.12: Channel 3 LS and low-pass model solutions for noisy simulation.

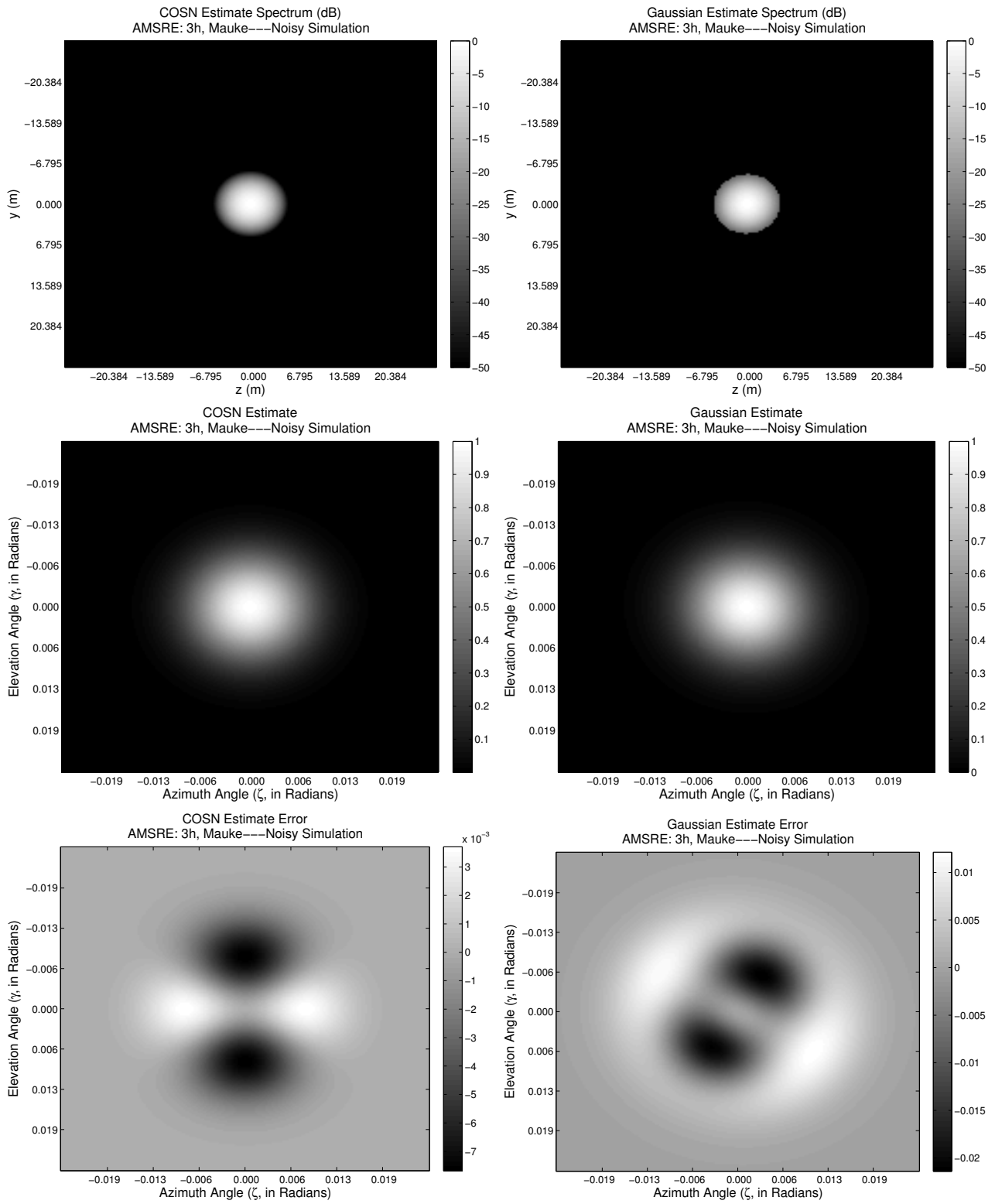


Figure 4.13: Channel 3 Power-cosine and Gaussian model solutions for noisy simulation.

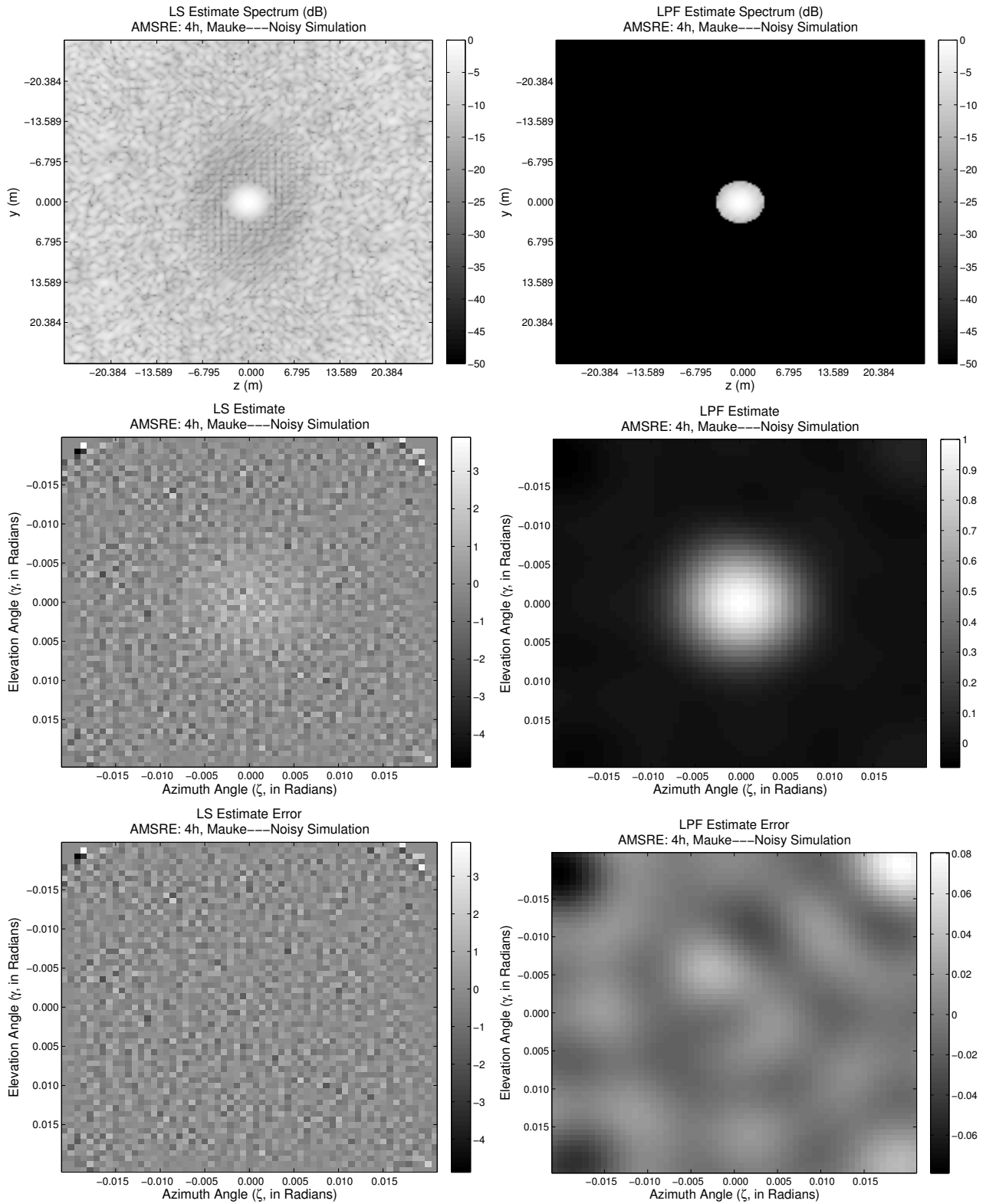


Figure 4.14: Channel 4 LS and low-pass model solutions for noisy simulation.

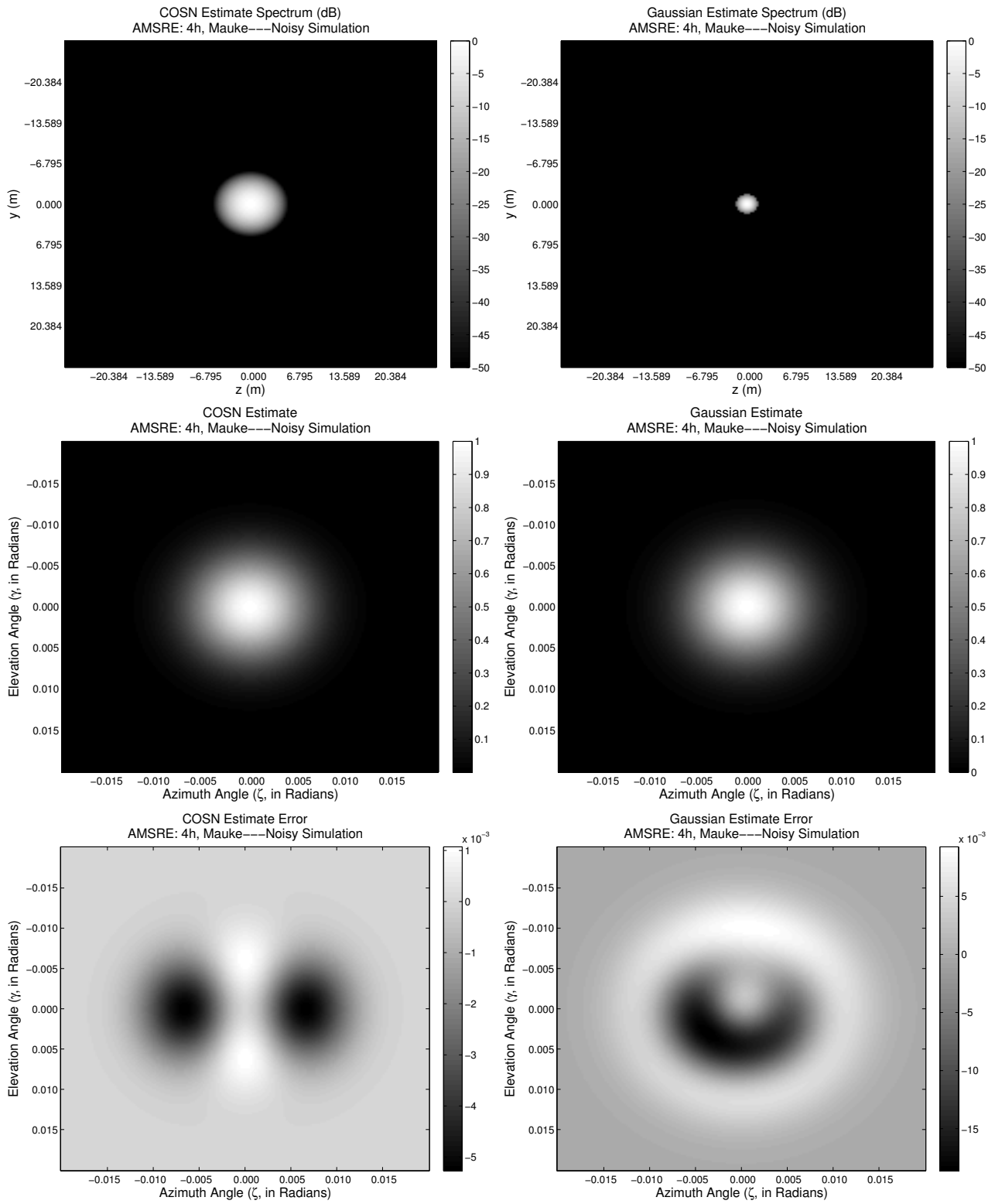


Figure 4.15: Channel 4 Power-cosine and Gaussian model solutions for noisy simulation.

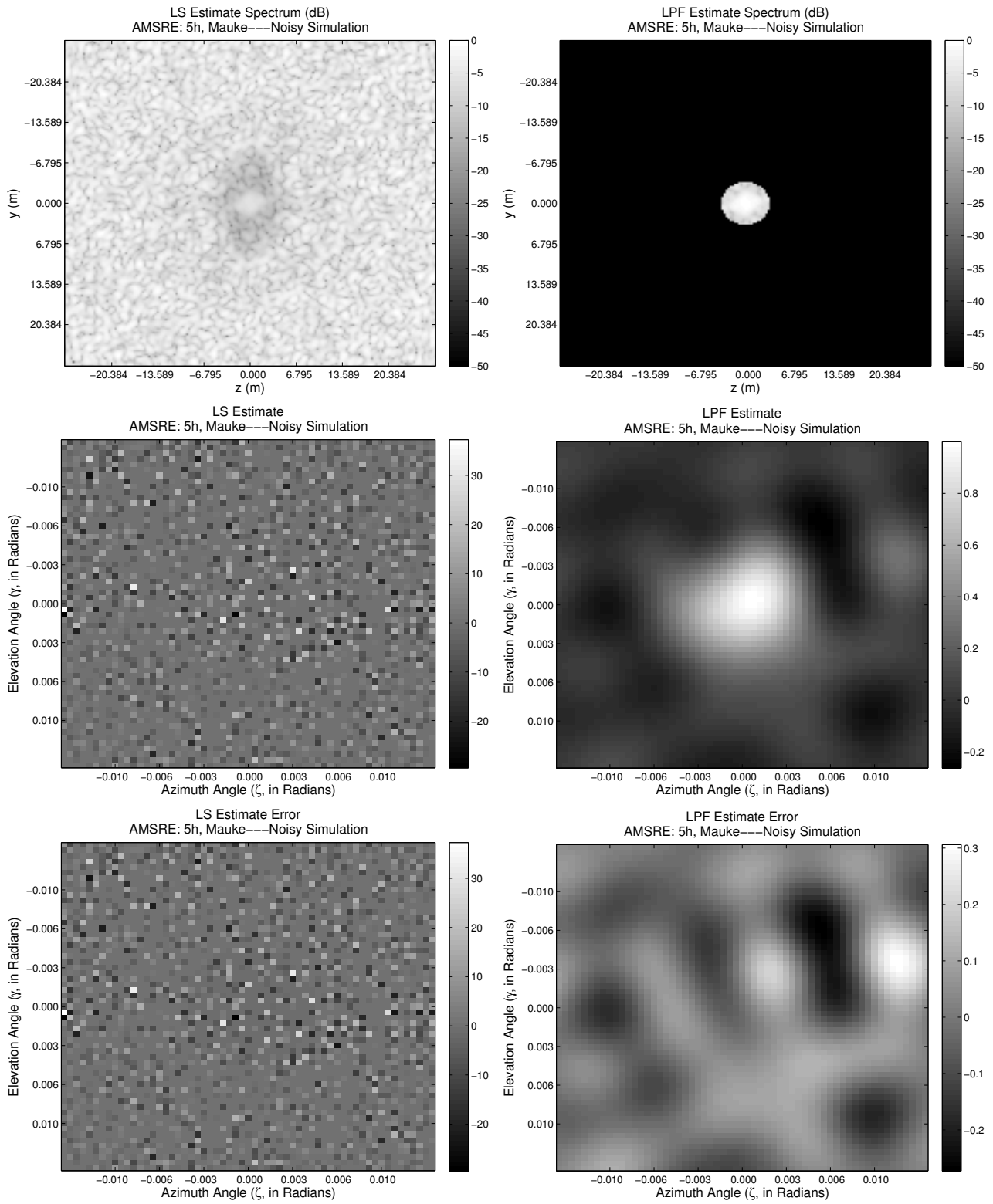


Figure 4.16: Channel 5 LS and low-pass model solutions for noisy simulation.

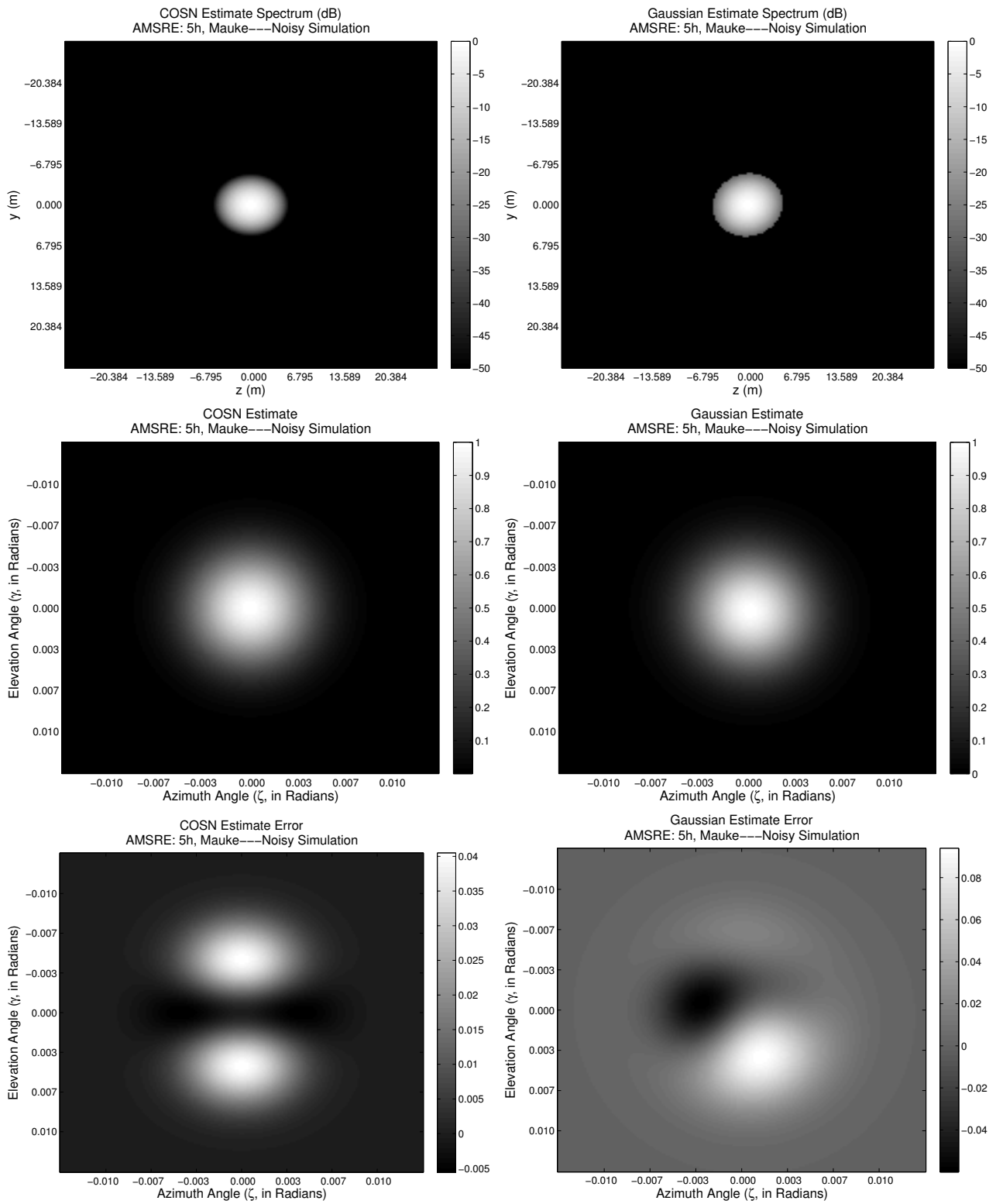


Figure 4.17: Channel 5 Power-cosine and Gaussian model solutions for noisy simulation.

The spectra are displayed in the equivalence current plane. The applied low-pass filter retains only those values that are within the reflector’s spatial support. Note in the LS estimate spectrum that noise amplification occurs for higher frequencies. This noise is reduced when the low-pass and Gaussian model are applied.

Figures 4.8 to 4.17 show noisy simulation results for channels 1–5. The error between the simulation aperture function and the estimated aperture function is only a few percent for channels 1–3 and less than 10% for channel 5. These results validate the estimation method developed in Section 4.1. The estimate error increases with channel frequency, as expected.

The figures also show that the Gaussian model differ by only by a fraction of a percent from the power-cosine model for most channels. This justifies the use of the Gaussian model in SIR with its simplicity and decreased computation. Estimation for actual data is performed in the next section.

4.3 AMSR-E Aperture Function Estimates

Figures 4.18 through 4.21 show the aperture function estimates for channels 1, 2, 3, and 5 and the “error” or difference between the currently-used Gaussian functions and the new estimates. While the Gaussian approximation is not the true aperture function, it is a good reference for comparison. Parameters for the Gaussian model are in Table 4.2. Chapter 5 analyzes T_B images created using these estimates.

Differences between these estimates and the Gaussian approximations previously used in SIR are only a few percent for channels 1–3. For channel 5, the difference is much greater. Because of the higher errors in the simulated aperture functions for channel 5 (Section 4.2), the corresponding new estimates are lower-confidence. For the lower-frequency channels, however, the aperture function estimation is validated by the simulation, showing that an aperture function can be estimated from raw data if certain criteria are met. These criteria include restrictions on the selected target scene to be used, limits on the amount of atmospheric effects for the T_B electromagnetic frequency and polarization, and the number of available measurements.

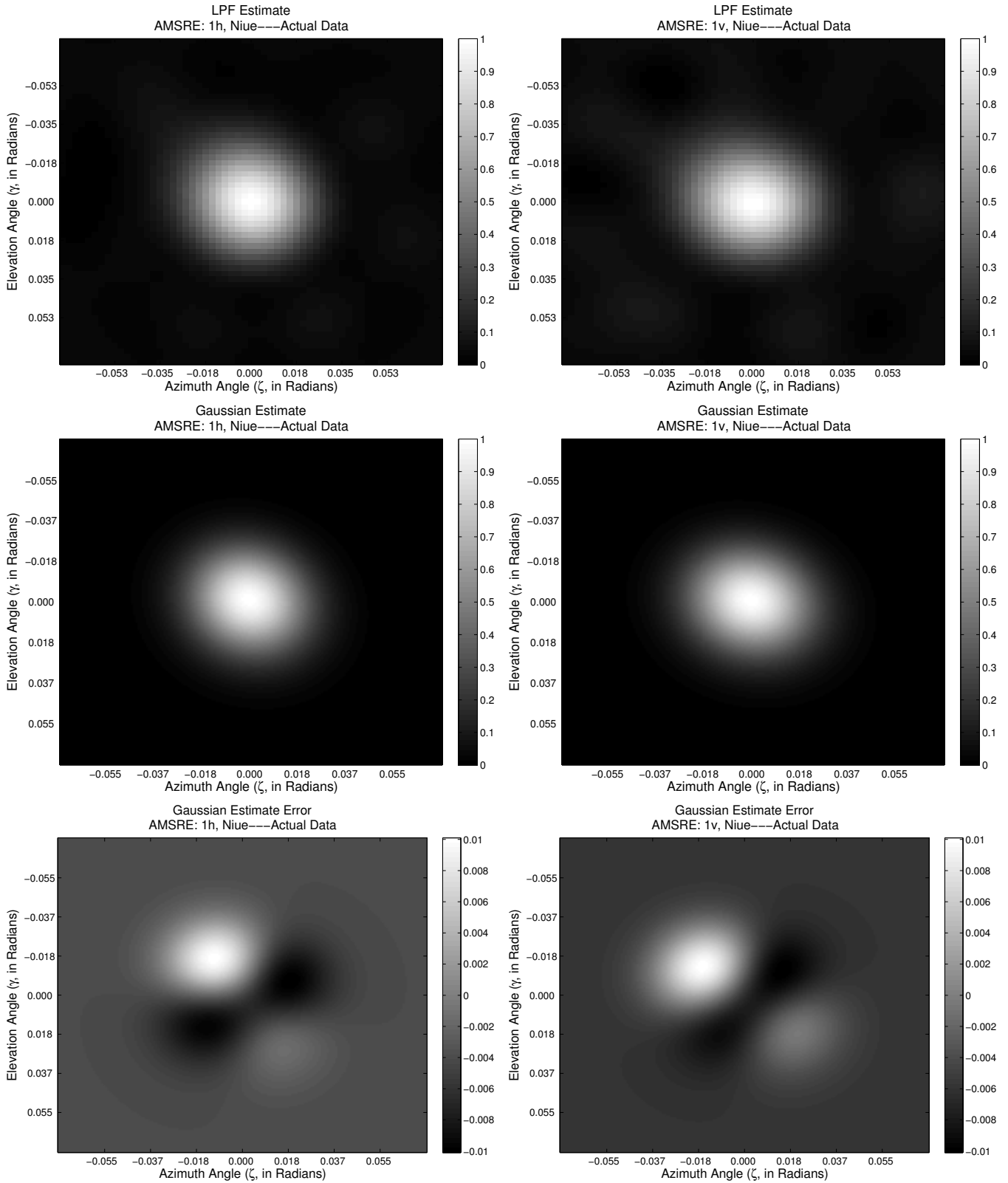


Figure 4.18: Channel 1 (v/h pol) solutions and “errors”—or the difference between each and the previously supposed aperture functions—for the Gaussian model.

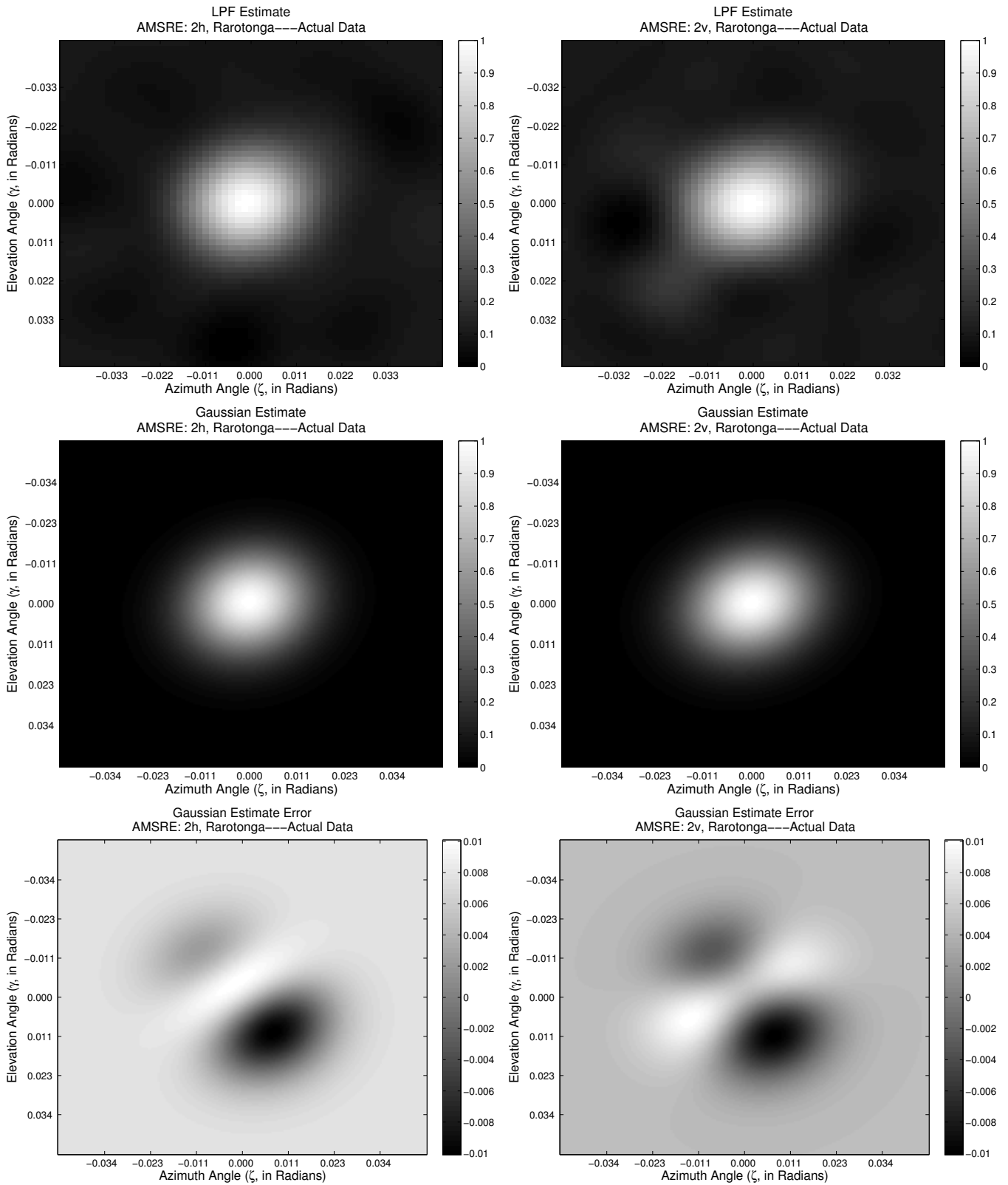


Figure 4.19: Aperture function estimates for channels 2 h/v pol. (See caption for Fig. 4.18.)

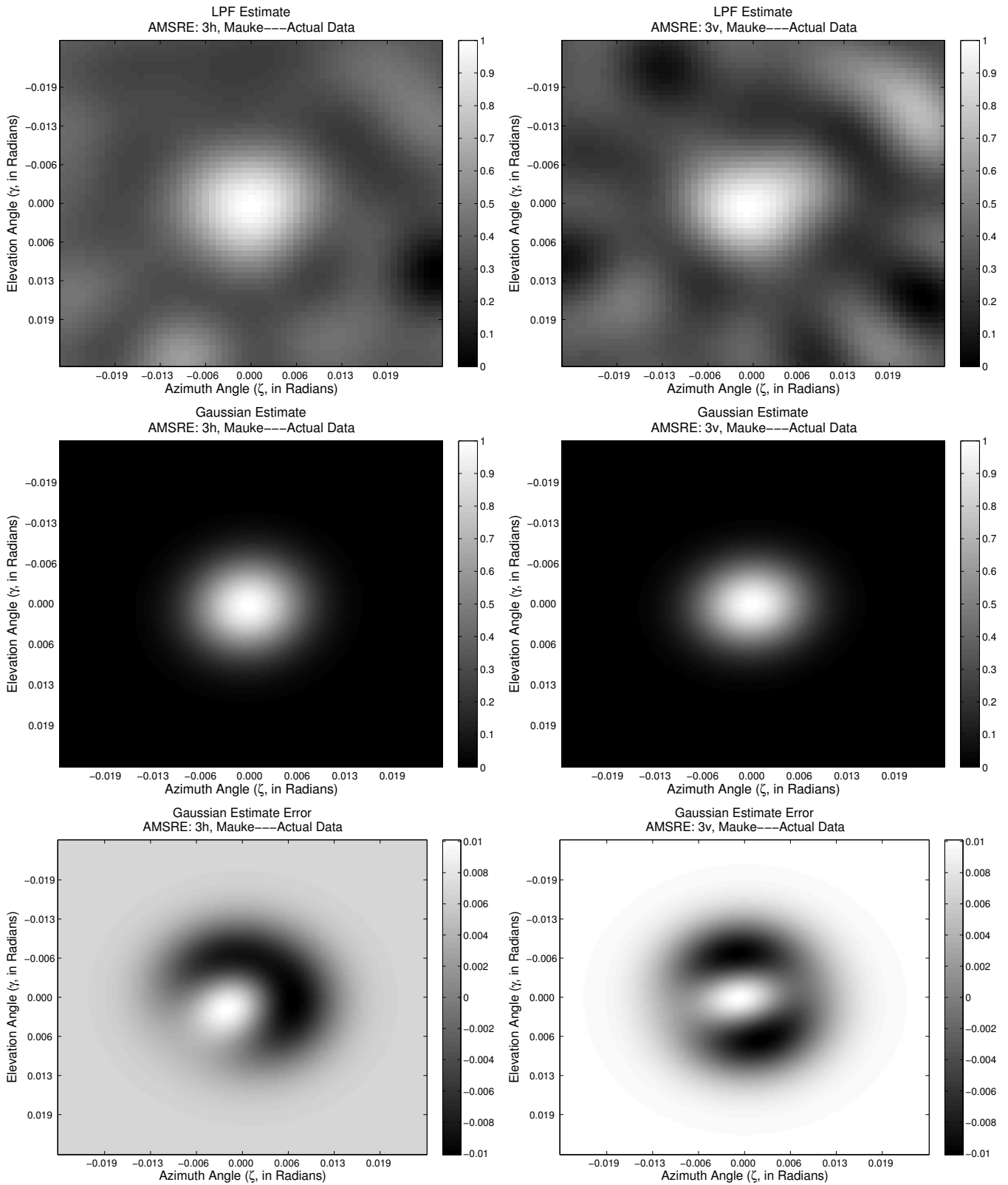


Figure 4.20: Aperture function estimates for channels 3 h/v pol. (See caption for Fig. 4.18.)

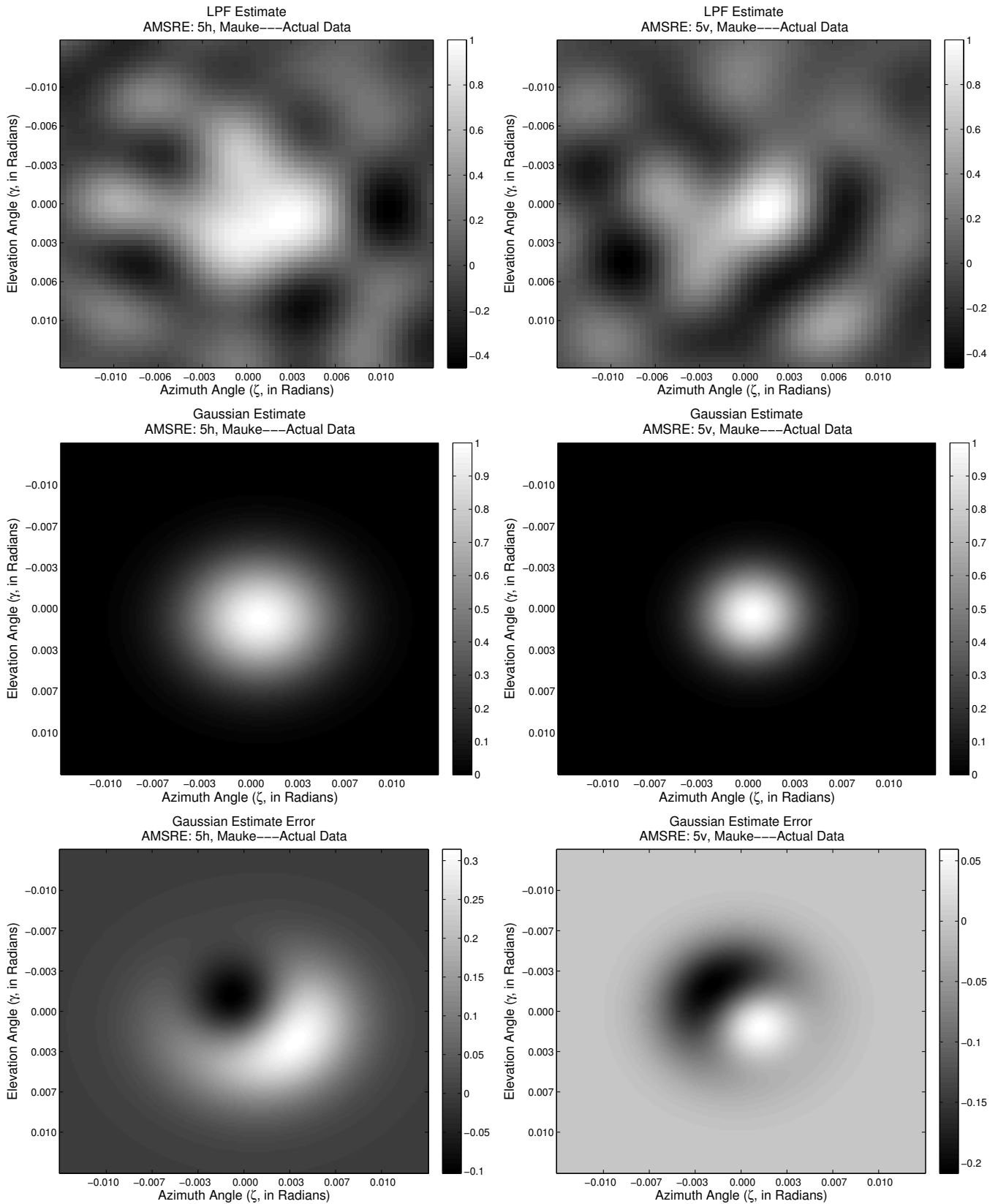


Figure 4.21: Aperture function estimates for channels 5 h/v pol. (See caption for Fig. 4.18.)

Table 4.2: Gaussian model parameters for aperture function estimates. Channels with asterisks are those whose estimated aperture functions are significant improvements as shown in the results of Chapter 5. Parameters y_0 and z_0 are the 3dB half widths of the Gaussian antenna footprint in the near cross- and along-scan directions, respectively. The rotation t is performed on the footprint after the spatial shifts Δy and Δz from the traditional center. Parameters y'_0 and z'_0 are values from AMSR-E specs (Table 2.1) used in the traditional aperture function approximation with no spatial shift nor rotation on the aperture.

Channel	y_0 (km)	z_0 (km)	t	Δy (km)	Δz (km)	y'_0 (km)	z'_0 (km)
1h*	39.0	21.2	4.6°	2.08	-0.81	37.5	21.5
1v*	38.5	22.3	5.4°	1.19	-1.00	37.5	21.5
2h*	24.1	13.9	-4.9°	1.33	-0.55	25.5	15.0
2v	24.1	14.3	-7.4°	0.73	-0.41	25.5	15.0
3h	12.3	7.2	-2.4°	0.61	-0.42	13.5	8.0
3v	11.2	7.2	-2.9°	-0.06	-0.17	13.5	8.0
5h	8.1	5.0	-0.1°	-1.48	0.82	7.0	4.0
5v	6.1	3.5	-0.6°	-0.78	0.46	7.0	4.0

4.4 Conclusion

The aperture function estimation problem developed in this chapter proved successful for all but AMSR-E channels 4 and 6. The small difference between the aperture function estimates and the traditional approximations validates using the traditional Gaussian for SIR. SIR T_B images generated using both are compared in the next chapter. Values of Gaussian-model aperture function estimates are found in Table 4.2.

Poor SNR and matrix singularities affect channels 4 and 6. Channel 4 is the most affected by poor SNR because it lies within the water frequency band, which increases noise due to atmospheric effects. Because of its narrow aperture function, the estimation for channel 6 requires a small island, decreasing the signal. The small island limits the number and location of samples over the island, which can cause singularities in the sampling matrix. These limitations prevent the estimation of aperture functions for channels 4 and 6.

CHAPTER 5. COMPARISONS

Adjustments of SIR parameters are performed in Chapter 3 by minimizing the RMS error in images reconstructed from simulated measurements over a synthetic brightness scene. In Chapter 4, a method for estimating the aperture function of a spaceborne radiometer from raw data is developed and applied to AMSR-E. In this chapter, we compare AMSR-E T_B images created from actual data using previous parameter values and aperture functions with those developed in the previous chapters.

First, a discussion and comparison of changing SIR iteration and threshold parameters is provided. Second, images created by using traditional and alternative Gaussian models for the supposed aperture in the SIR algorithm are compared. Last, a conclusion is given.

5.1 Tuning

Chapter 3 presents a simulator-based method to optimize SIR iteration and aperture function threshold parameters for AMSR-E. Most of the suggested optimum values for these parameters differ from those used currently for AMSR-E processing. This section compares images reconstructed using optimal (as described in Chapter 3) and the currently-used iteration and threshold parameter values in the SIR algorithm. Although the parameter values from Chapter 3 are optimal in the RMS error sense as per our simulation, we recognize that changing parameter values results in trade-offs which may be undesirable in specific cases. These trade-offs are discussed for both tuning and threshold parameters.

Because of the increased SIR iterations and altered threshold for most channels, some T_B change is expected near sharp transitions. For an initial evaluation we choose Iceland as one comparison target to evaluate the changes. A region internal to Greenland is also chosen to validate the consistency of the T_B image where little change is expected. The low-resolution gridded (GRD) image serves as a low-resolution reference.

5.1.1 Iteration

In comparing images of differing SIR iteration, we start with channel 1 where the suggested iteration change (from 20 to 47) is greatest. Figure 5.1 shows the optimal and sub-optimal iteration images for the Am1v channel and their difference. The difference image shows that the area of greatest difference between the two is near sharp T_B transitions. A larger difference is expected in areas near transitions due to the amplification of the high-frequency band with additional iterations.

Figure 5.2 shows a North–South cross section (or slice) through both images over Iceland for channels 1–6. The GRD T_B is also included. The plot shows that the increased iteration sharpens the T_B transition while increasing the ringing amplitude. While the sharp transition is desirable, more iterations increase the ringing and the noise amplification, forcing us to decide between sharp transitions or decreased ringing.

Although ringing due to sharp transitions is intuitive, the increased variation internal to the island may or may not be signal. Even the GRD plot is somewhat unreliable here because its increased susceptibility to aperture function blurring. One interesting observation comes by comparing the plots of different channels. We note that the brightness temperatures at similar frequencies are highly correlated and that higher frequency channels have a higher effective resolution. We use channel 3 as a qualitative reference for channels 1 and 2. (Channel 4 is in the water band, and may not correlate well depending on atmospheric effects.)

For both channels 1 and 2, increasing iteration lowers the local minimum internal to the island to more closely match that of channel 3. The same comparison for Fig. 5.3 shows that channels 1 and 2 match channel 3 better for the optimal iteration number suggested in Chapter 3 as opposed to the sub-optimal value. These characteristics support the new values of the SIR iteration parameters.

The optimum value of the iteration parameter for channels 3–6 changes much less than for channels 1 and 2; however, images of channels 3 and 4 follow similar trends because of increased iteration number. For channels 5 and 6, while the iteration number decreased slightly from sub-optimal to optimal, the change in T_B image is marginal. Fewer iterations mean less computation time—so although they provide similar output images, fewer iterations are preferred.

In Fig. 5.4, we see that the T_B changes are a fraction of a Kelvin. The most apparent differences are in channels 1, 2, and 6. Channels 1 and 2 experience an increased variation in

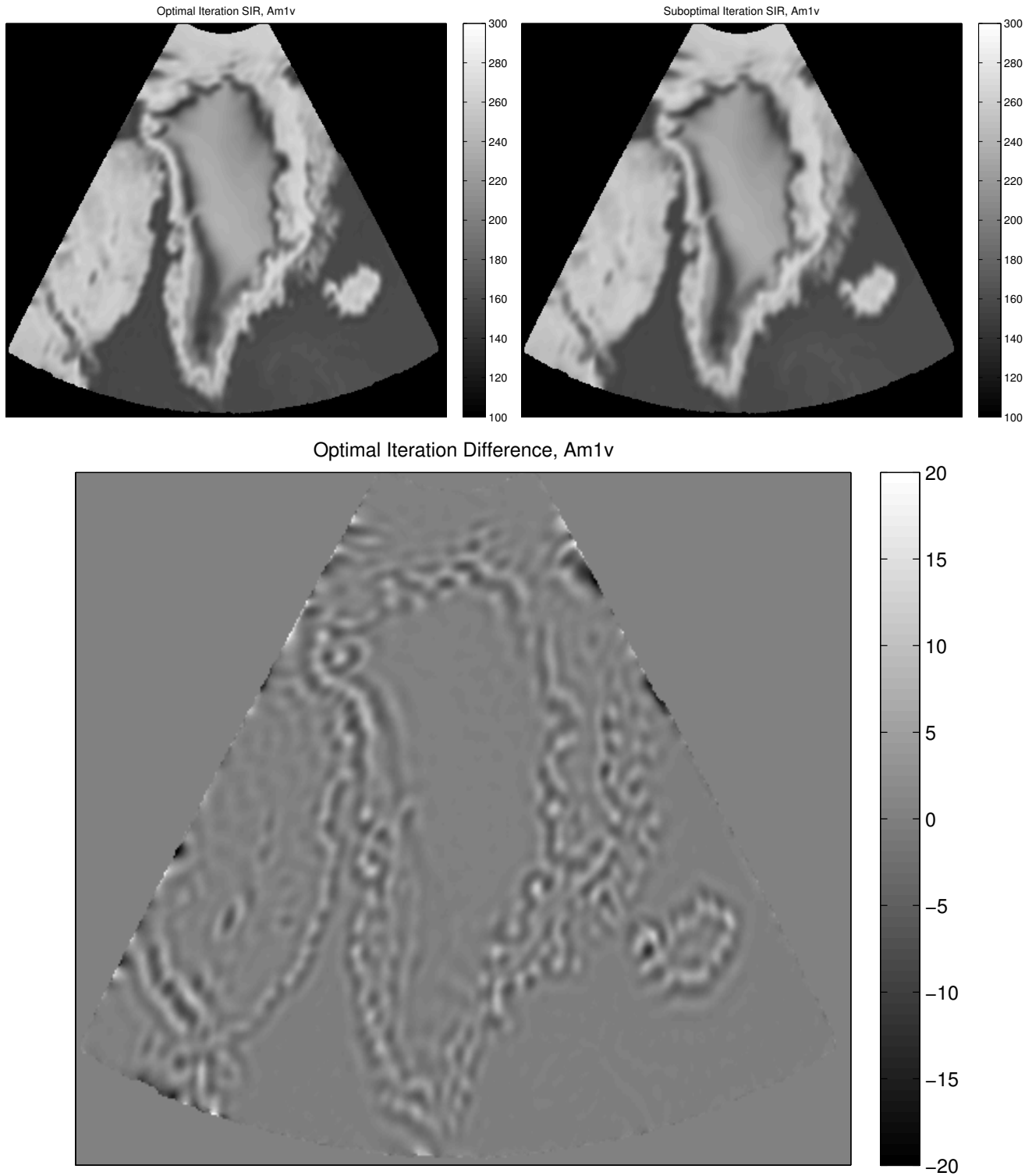


Figure 5.1: Greenland SIR Am1v T_B images produced using the optimal (upper left) and sub-optimal (upper right) number of iterations and the difference. A difference image of the top two images (bottom). There is a larger difference near sharp transitions primarily because the image created using more SIR iterations has higher frequency content and therefore sharper transitions.

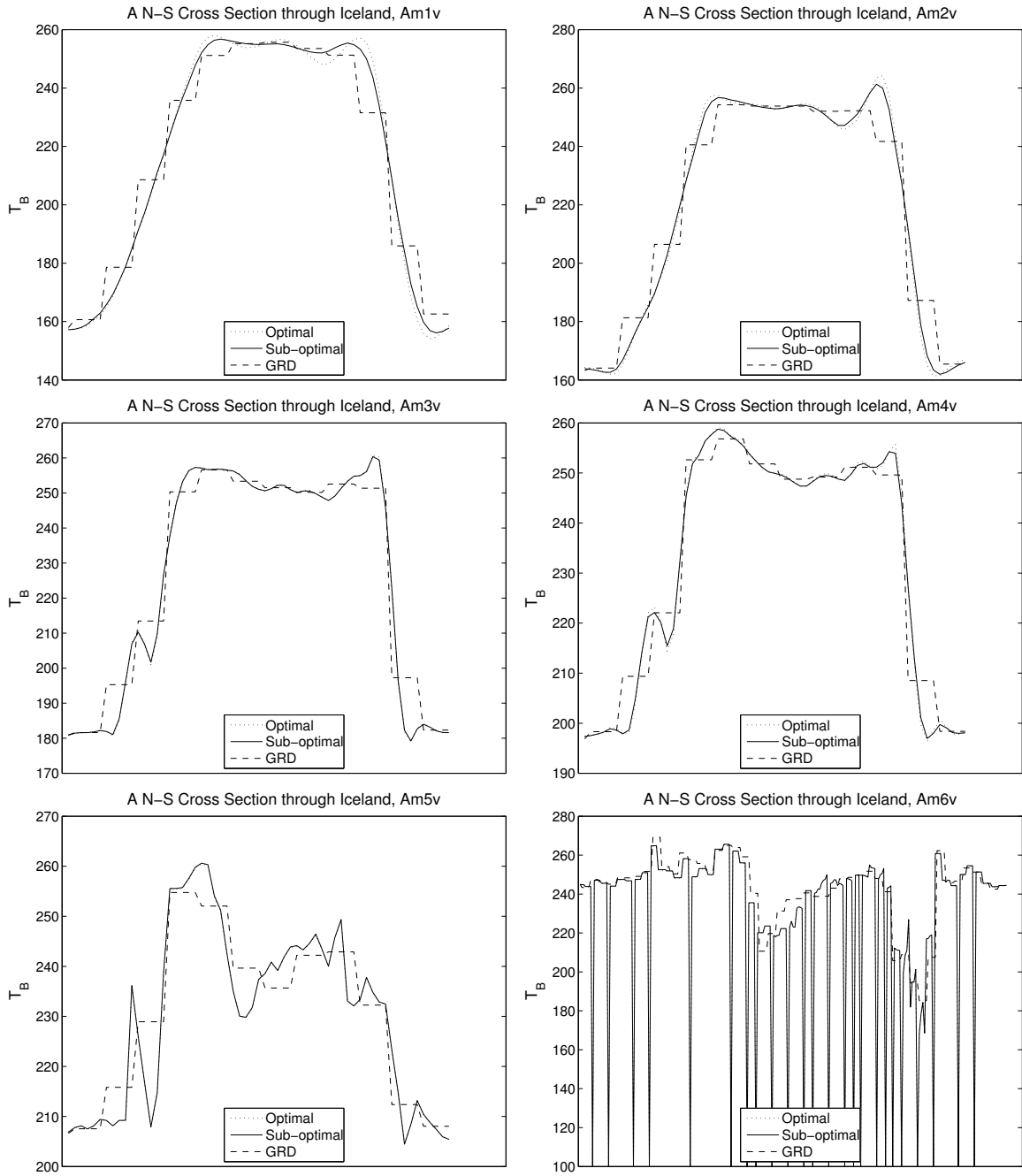


Figure 5.2: A N–S slice of image T_B over Iceland for Am^*v channels, with optimal (as per Chapter 3) and suboptimal (20) SIR iterations. The dashed line is a low-resolution GRD T_B plot for comparison. SIR plots are results of averaging 5 pixels (the SIR-to-GRD pixel ratio) in the cross-slice direction for all but channels 5 and 6. This exception is due to the imaging gaps in channels 5 and 6 for un-tuned aperture function thresholds.

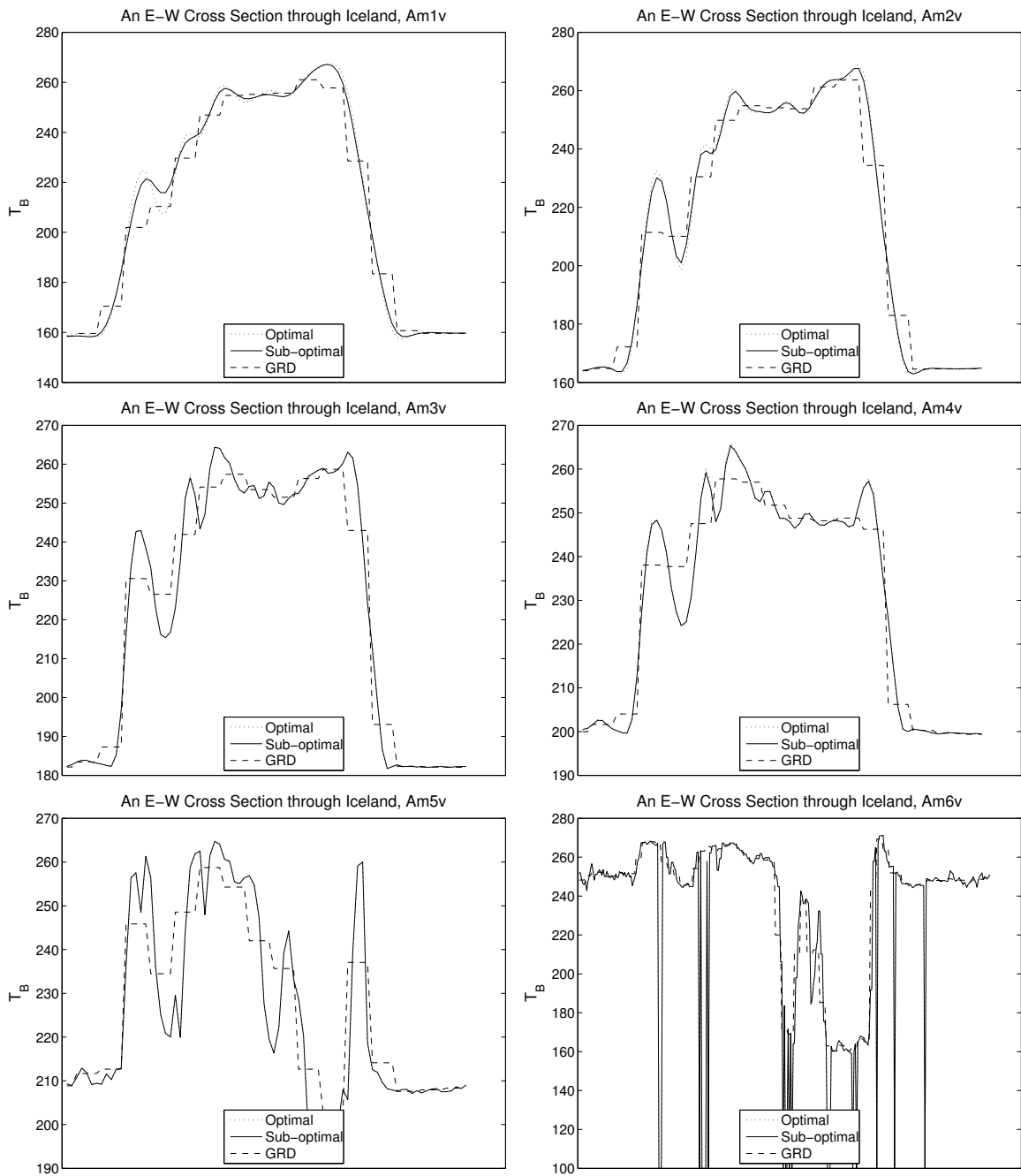


Figure 5.3: An E–W cross section through Iceland, as in Fig. 5.2.

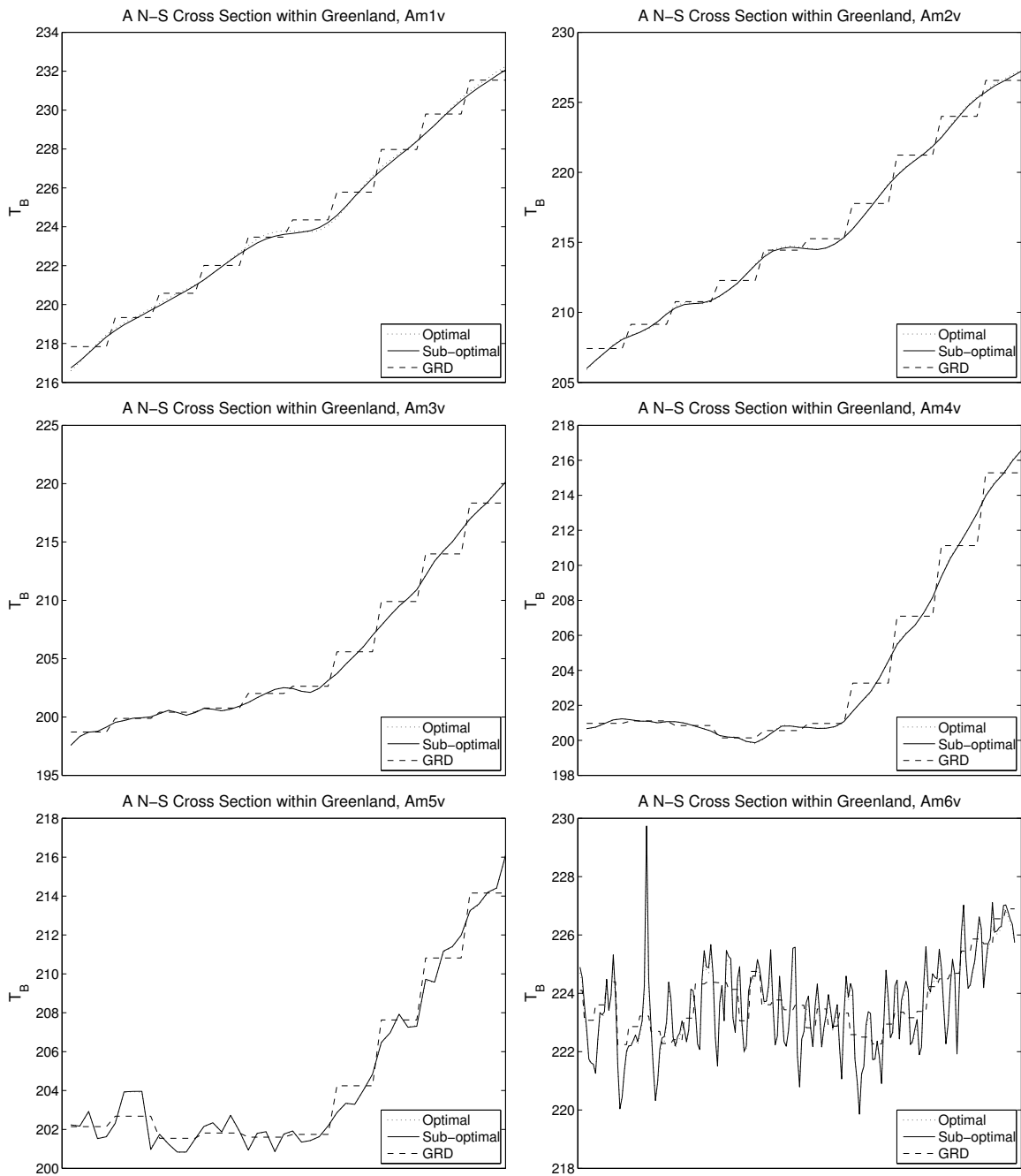


Figure 5.4: A N-S cross section through Greenland, as in Fig. 5.2.

slope. We attribute this to signal because of the changes' high correlation with that of channel 3. The decreased iterations for channel 6 causes a slight decrease in the amplitude of the peaks because of their high frequency.

5.1.2 Threshold

In optimizing the SIR aperture function threshold, the parameter value changed only for channels 1, 2, 5, and 6. For channels 1 and 2, an increase in threshold (which decreases the accuracy of the aperture function) is suggested. While this decreases the T_B images' accuracy, it also decreases the computation time. Figures 5.5, 5.6, and 5.7 show that the difference in image T_B is small, justifying the change of threshold for these channels.

For channels 5 and 6, the threshold is decreased, increasing the accuracy of the aperture function approximation. While the increased accuracy for these channels comes with increased computational costs, the benefits outweigh the costs. Also, channel 5 and 6 footprints are much smaller than those of the lower-frequency channels, so they require much less computation even after the threshold change.

From Figs. 5.5 and 5.6, we see that the primary difference is the elimination of the T_B gaps in the image, particularly for channel 6. Figures 5.8 through 5.13 show T_B images generated using optimal and sub-optimal thresholds and their differences, where this improvement is apparent.

Figures 5.12 and 5.13 are daily images. Even with the increased sampling density of the daily set, there are still T_B gaps in the suboptimal image. Also, while effects of temporal T_B variation are apparent in all the daily images, the optimal threshold value decreases the severity of the effects. These benefits validate using the optimized aperture function threshold for daily images.

5.2 Aperture Function Estimate

In Chapter 4 a method for estimating the aperture function of a satellite radiometer is developed and applied to AMSR-E. In this section, we compare Greenland T_B images generated using the previously-used aperture function to those generated using the new approximations as

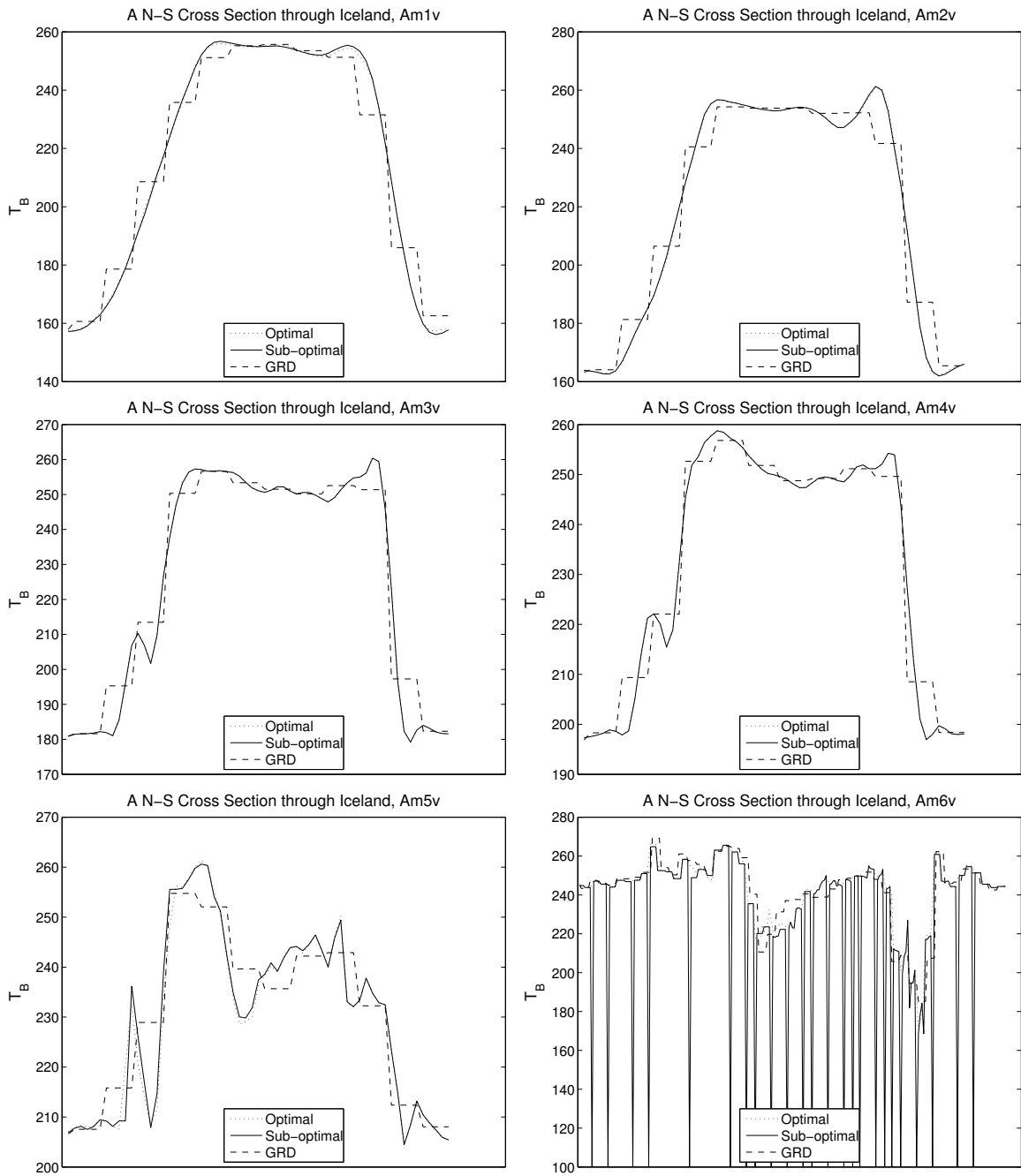


Figure 5.5: A N–S cross section of image T_B through Iceland for Am^*v channels, with the optimal (as per Chapter 3) and -8dB SIR aperture function threshold. The dashed line is GRD T_B value for comparison.

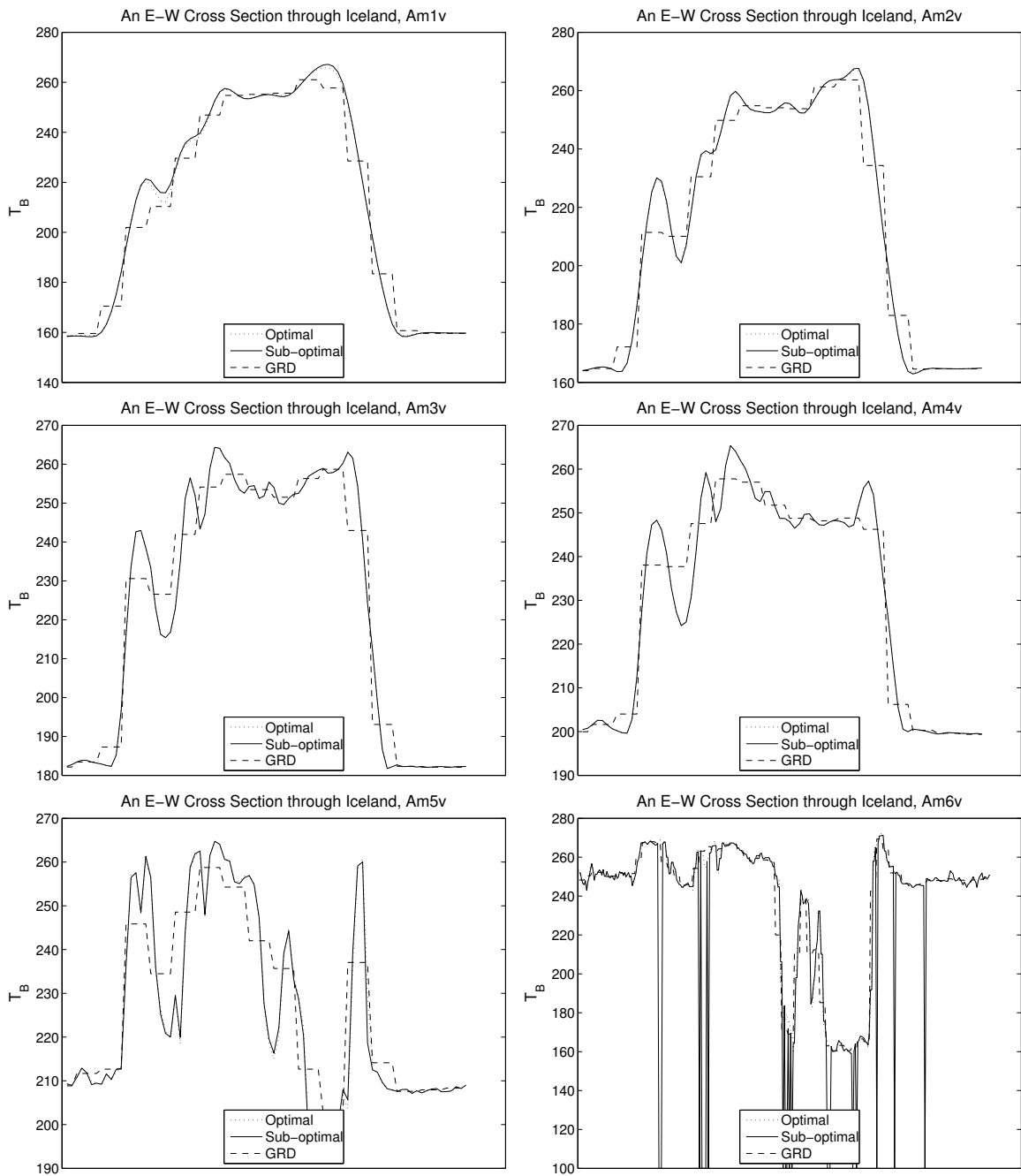


Figure 5.6: An E–W cross section through Iceland, as in Fig. 5.5.

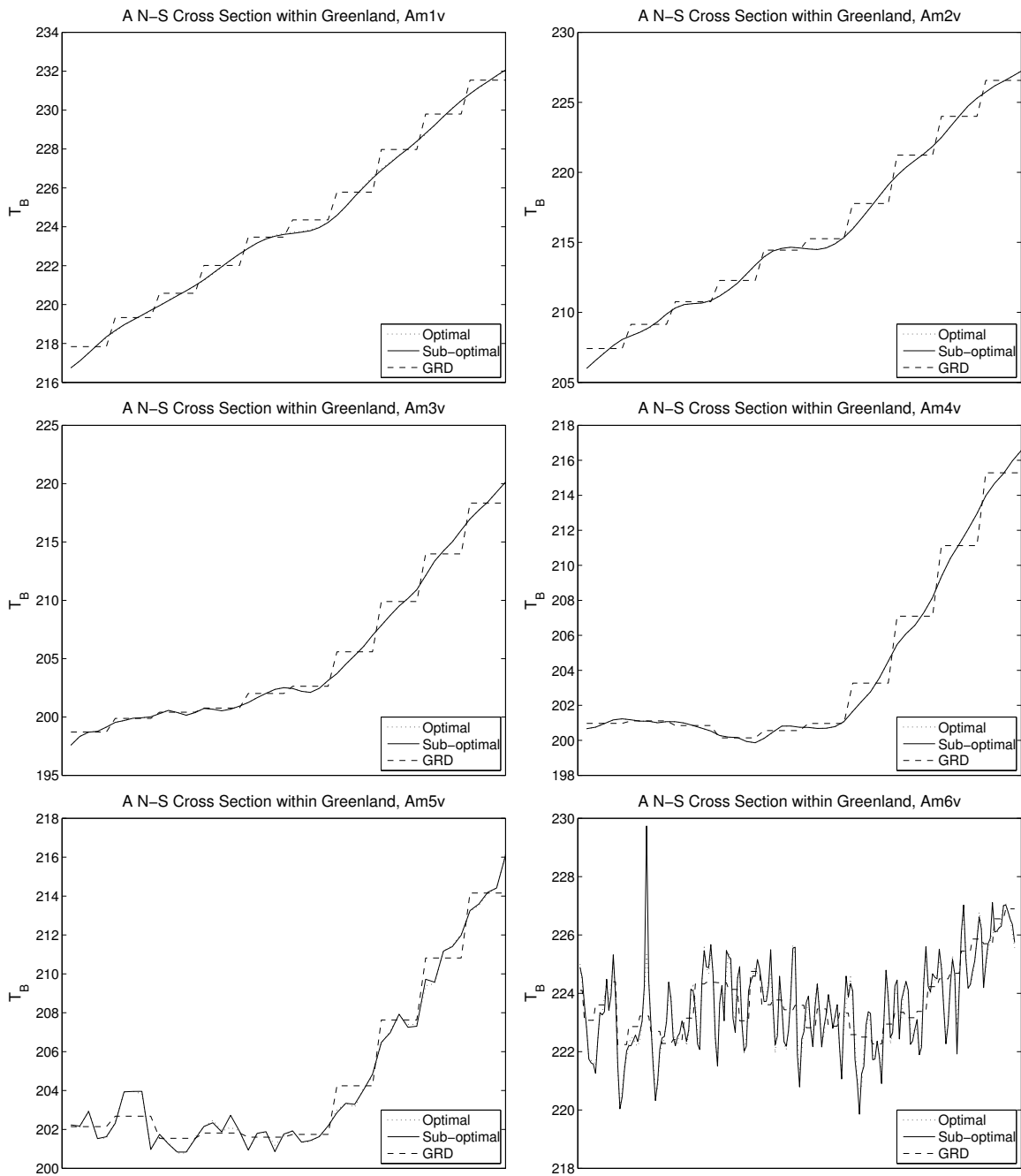


Figure 5.7: A N-S cross section through Greenland, as in Fig. 5.5.

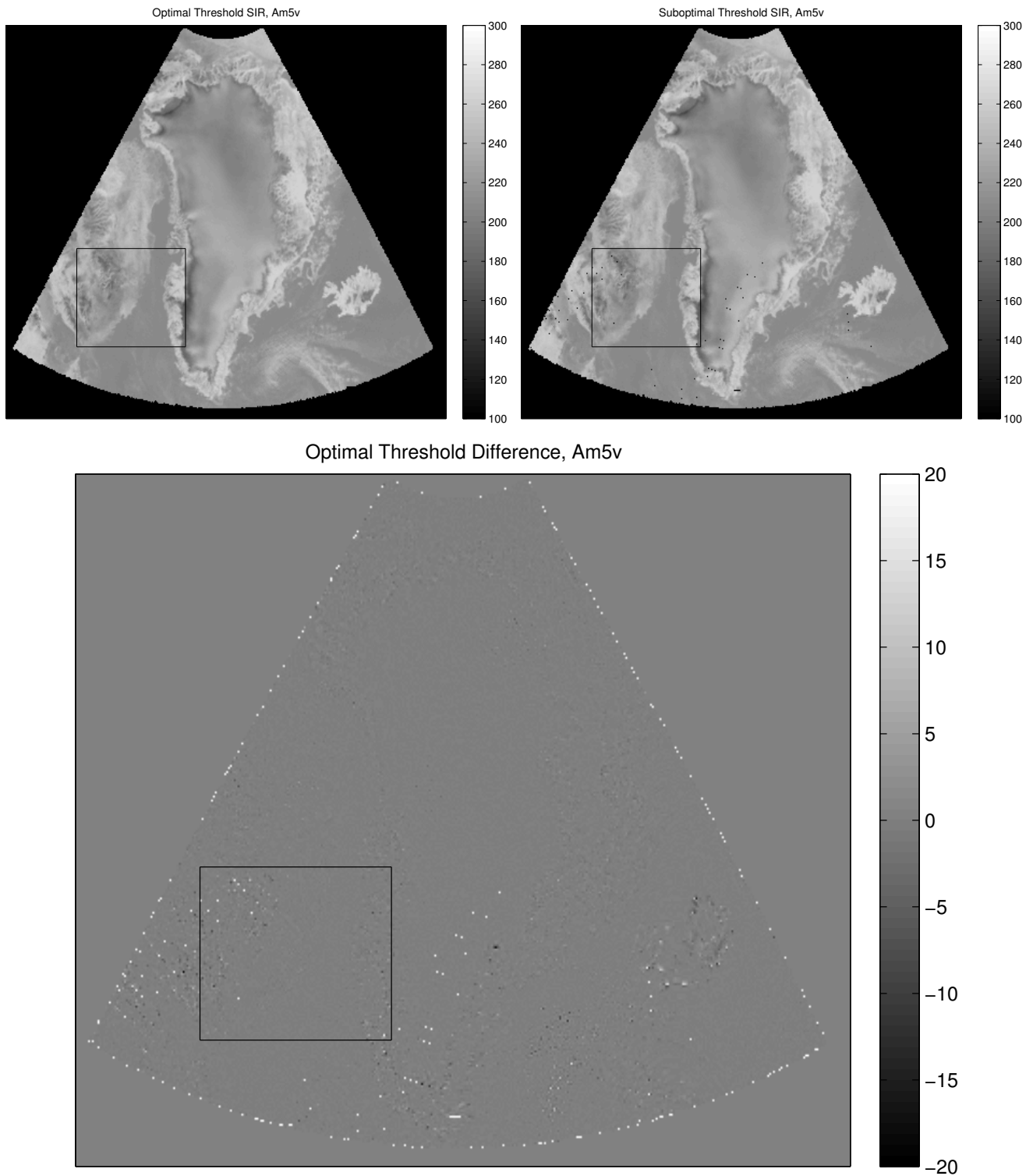


Figure 5.8: SIR Am5v T_B images produced using the optimal (upper left) and sub-optimal (upper right) thresholds and their difference (bottom).

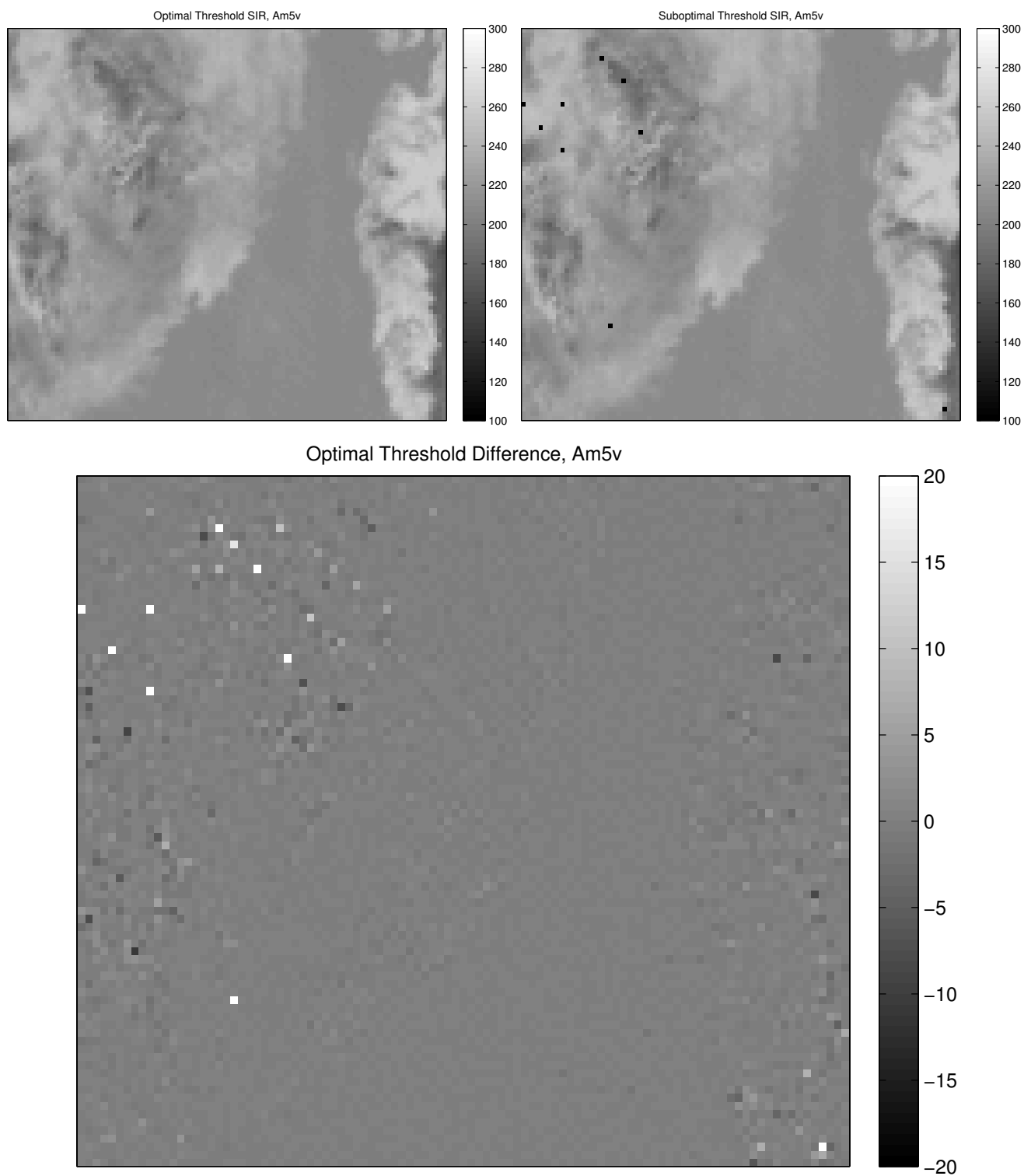


Figure 5.9: SIR Am5v T_B images produced using the optimal (upper left) and sub-optimal (upper right) thresholds and their difference (bottom), zoomed to the region indicated in Fig. 5.8.

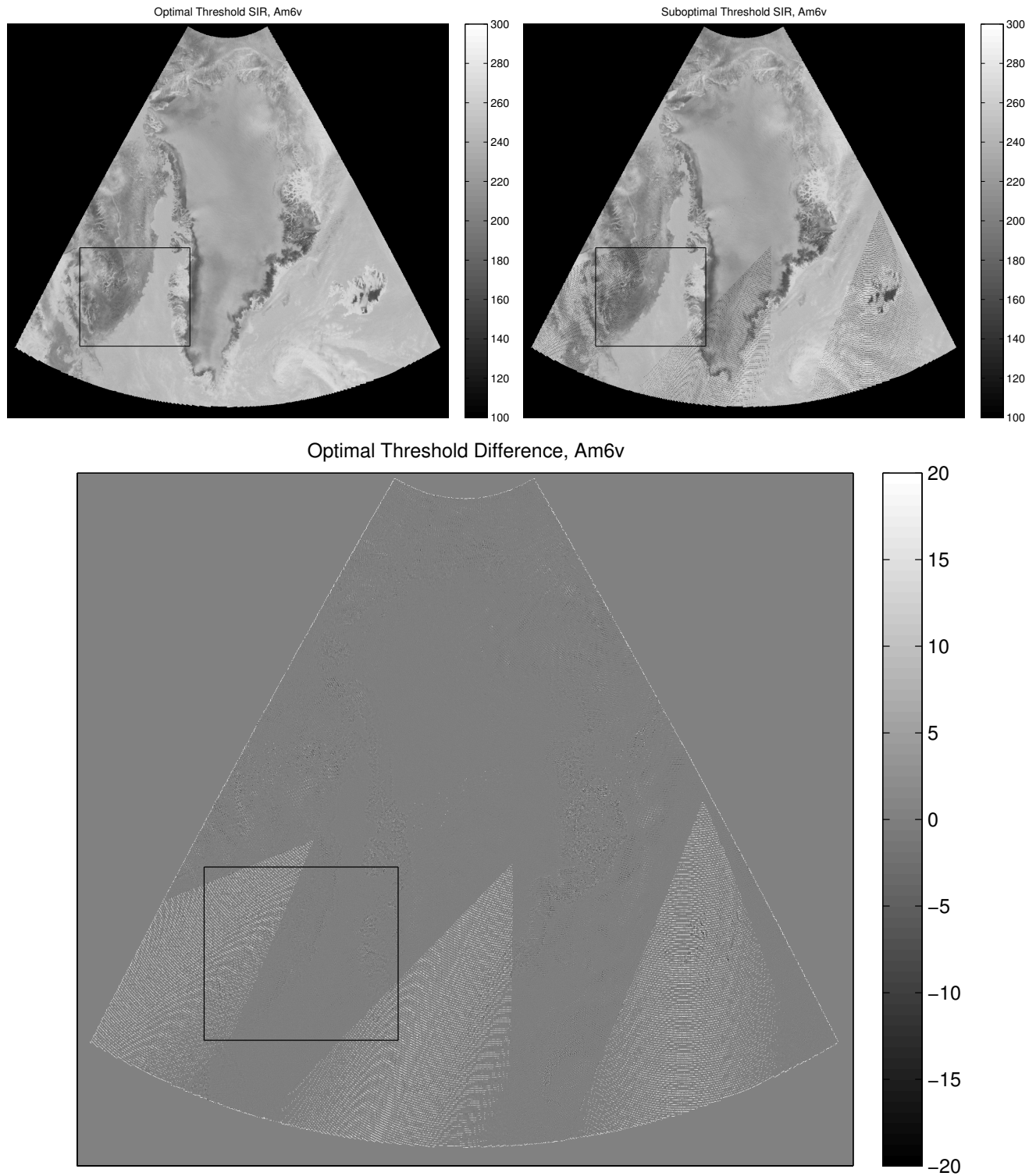


Figure 5.10: SIR Am6v T_B images as in Fig. 5.8.

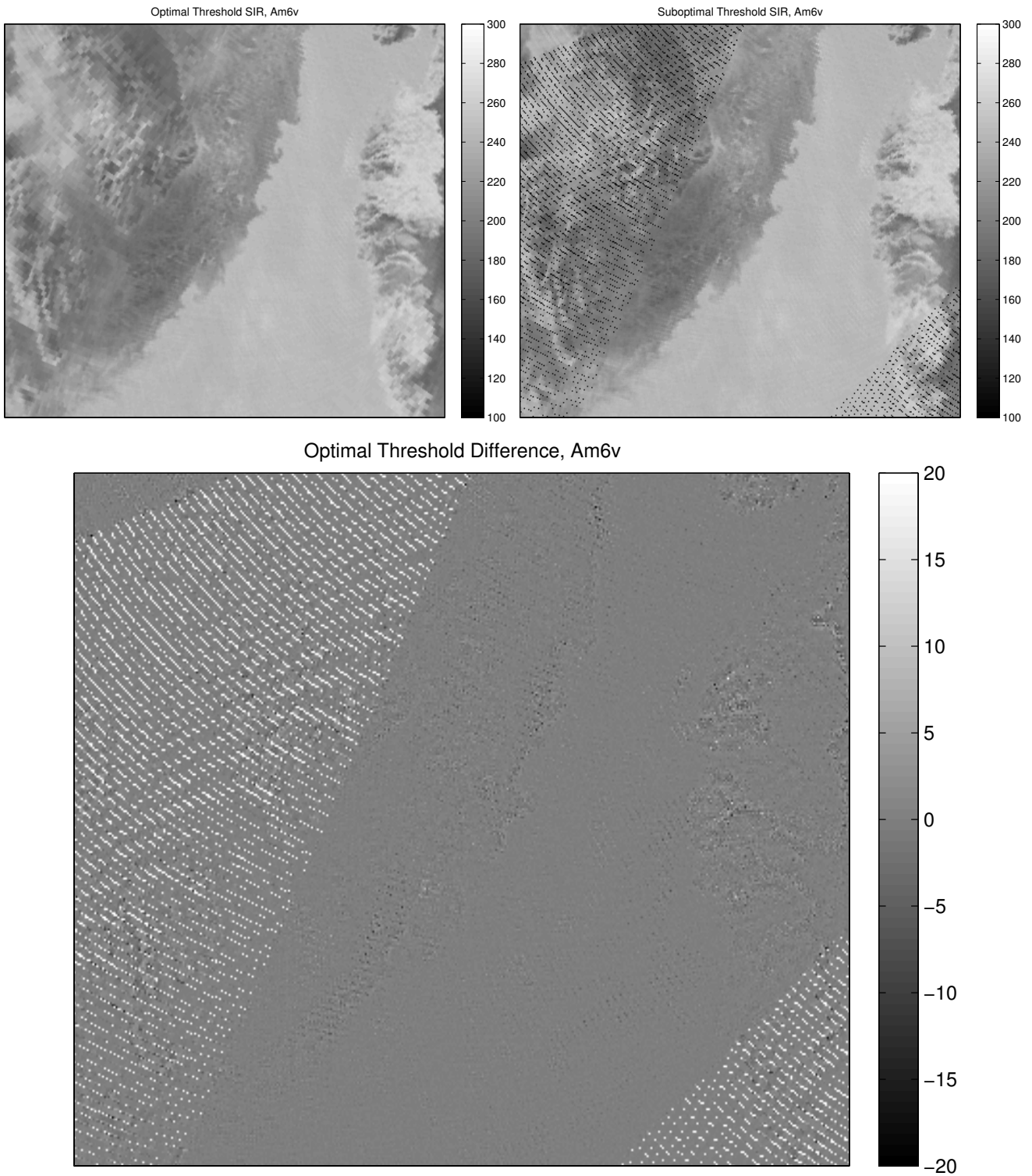


Figure 5.11: SIR Am6v T_B images as in Fig. 5.9

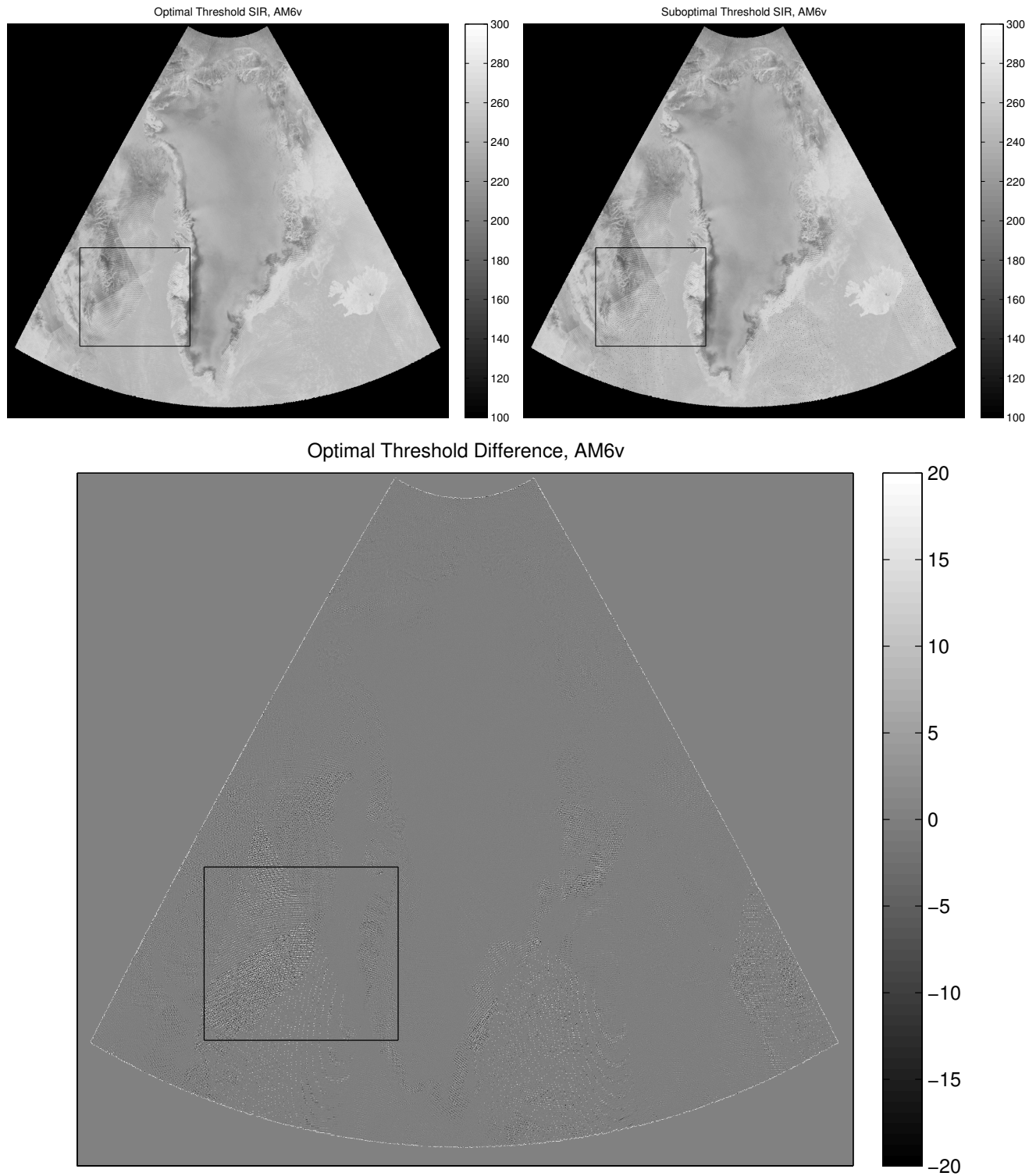


Figure 5.12: SIR AM6v T_B images as in Fig. 5.8.

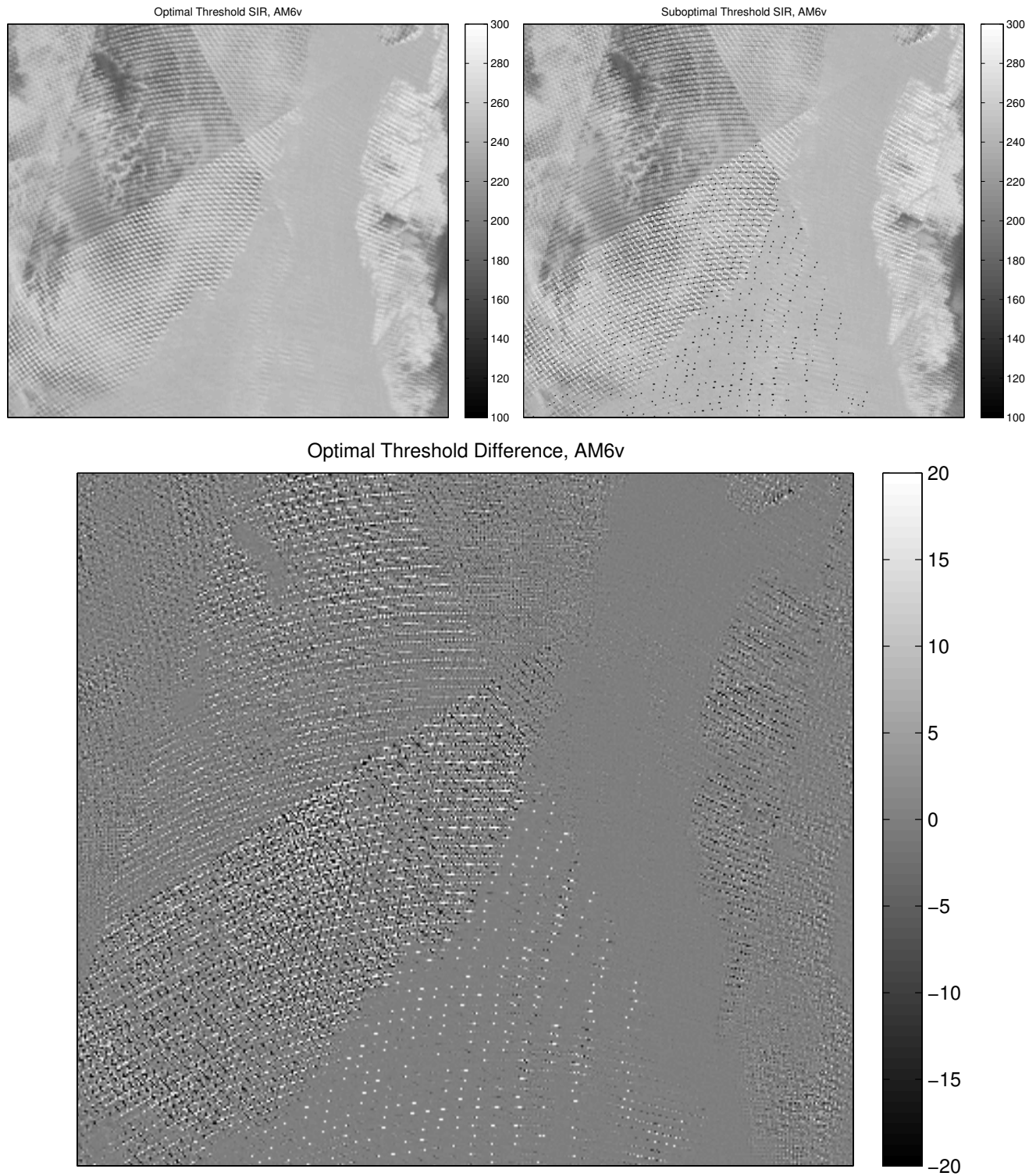


Figure 5.13: SIR AM6v T_B images as in Fig. 5.9.

the aperture function in SIR. The purpose of the comparison is to validate the new aperture function for each channel. Since most of the aperture function estimates found in Chapter 4 are very close to the traditional Gaussian approximation, only a small difference is expected in the output images.

Figures 5.14 through 5.21 show Greenland images generated from SIR using the estimated (Chapter 4) and traditional aperture function approximations and their difference. The maximum T_B difference for most channels is a few Kelvin. There is no obvious evidence supporting the use of one aperture function over the other.

As with changing SIR iteration, the greatest error is near boundaries between regions of contrasting T_B . However, one distinction is apparent in the difference images. Note in the difference image that the difference along the southern coast of Iceland is of opposite sign of the northern coast. This indicates that at least one of the sampling aperture approximations used in SIR is shifted from the true location. The shift is not universally latitudinal throughout the image—it depends on the rotations of the aperture function throughout each scan. T_B cross sections through Iceland's coastline highlight some characteristics which may be useful in supporting a particular choice for the aperture function.

Figures 5.22 through 5.29 show T_B cross sections through Iceland's coastline. The actual coastline lies near the center of the transition region for each plot. Each figure contains data from **m** and **n** LTOD T_B images and the **M** daily image for the estimated and traditional aperture function reconstruction. Because the island is stationary, the reconstruction with the most consistent transition is assumed to be the most correct.

For channels 1h, 1v, and 2h, the modified SIR using the estimated aperture function provides a more consistent indication of the location of the coast than the images created using the traditional aperture function. For the remaining channels, the traditional aperture function produces better transitions. Based on this criterion, the aperture function estimates for channels 1h, 1v, and 2h are suggested as replacements to the traditional approximation.

To compare results for a more homogeneous target, Fig. 5.30 has T_B slices internal to Greenland for the **m** data set. Again, the primary difference between the T_B values is the expected spatial shift.

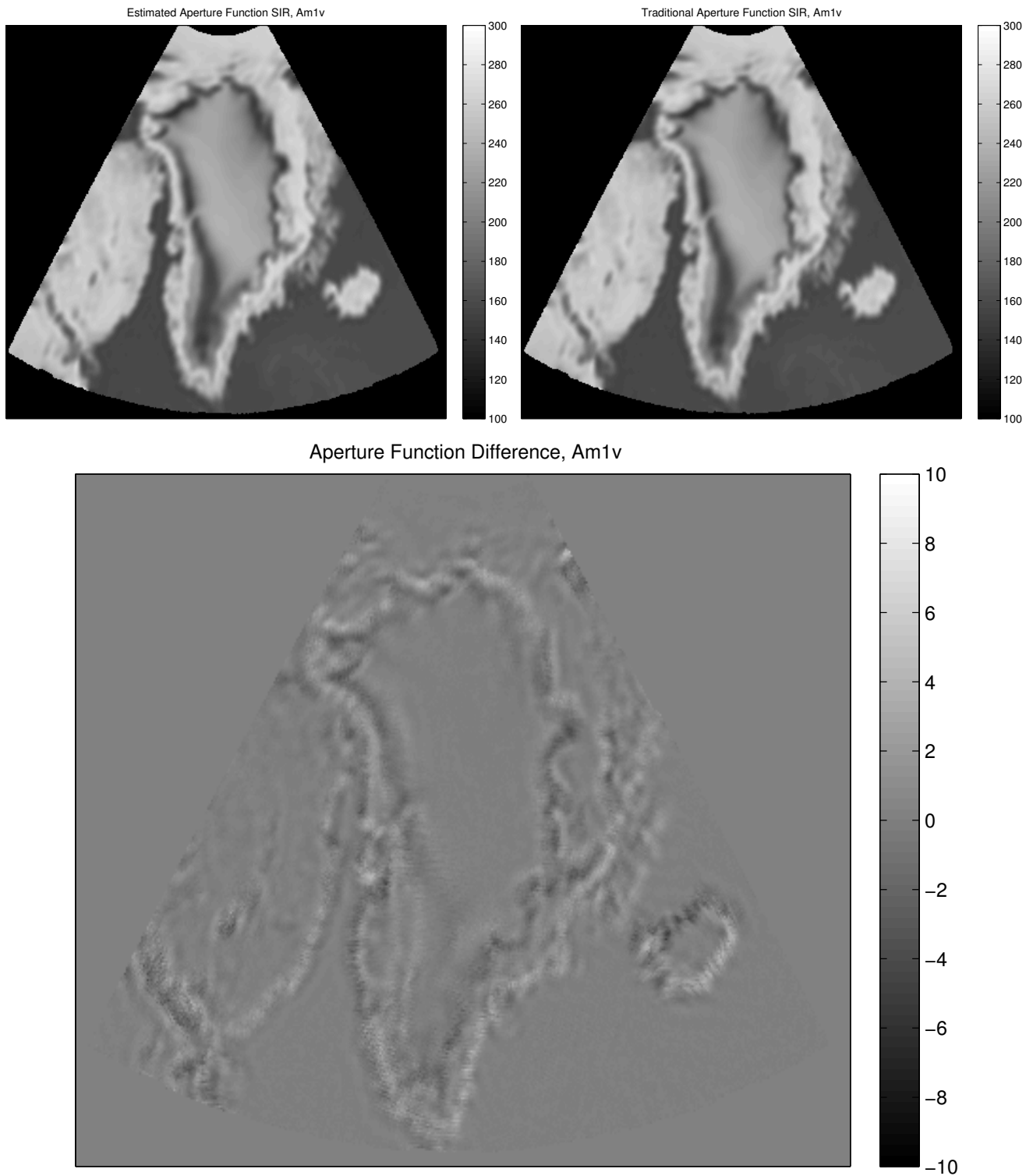


Figure 5.14: SIR Am1v T_B images produced using the estimated (upper left) and traditional (upper right) aperture functions in SIR and their difference.

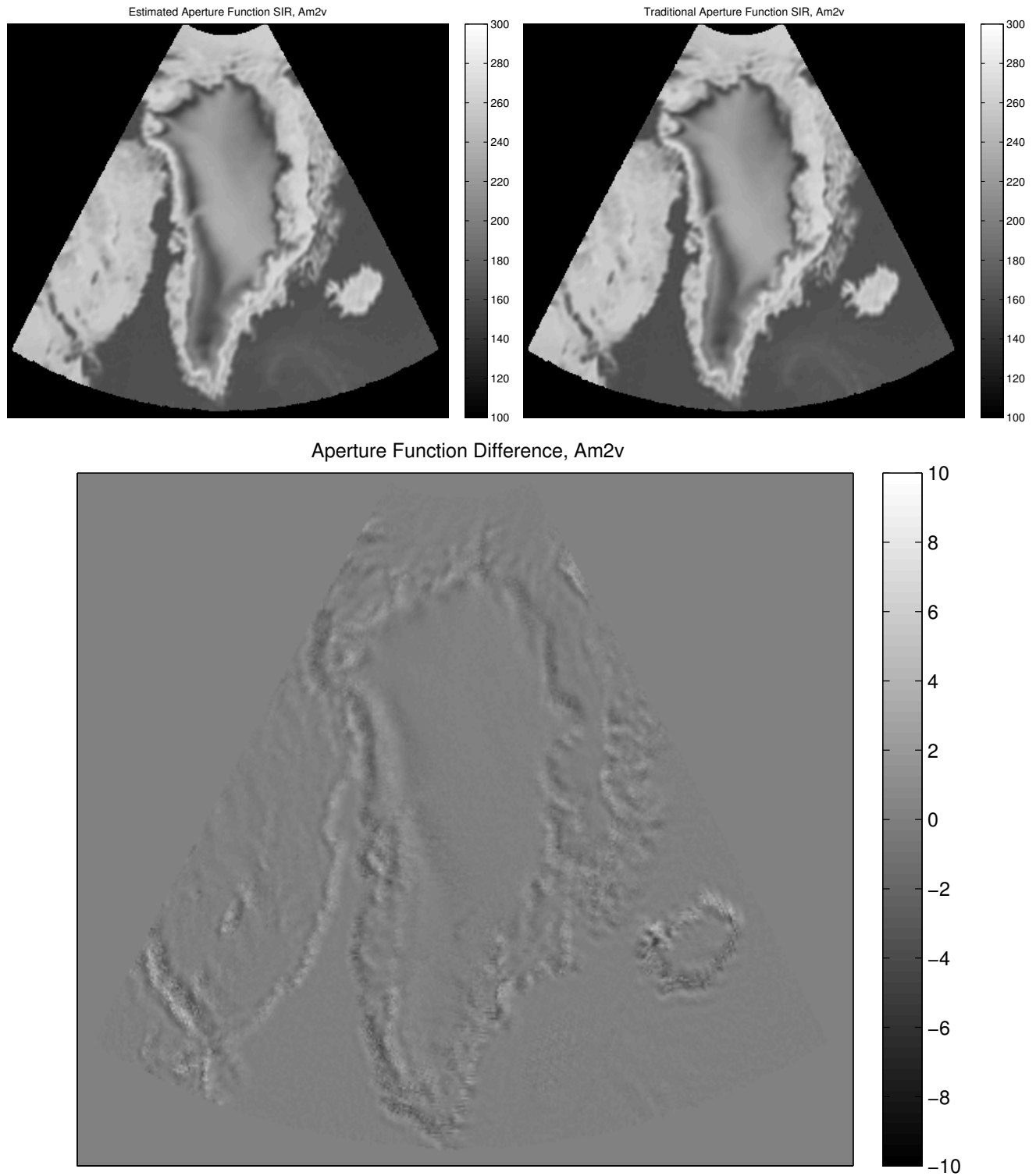


Figure 5.15: SIR Am2v T_B images as in Fig. 5.14.

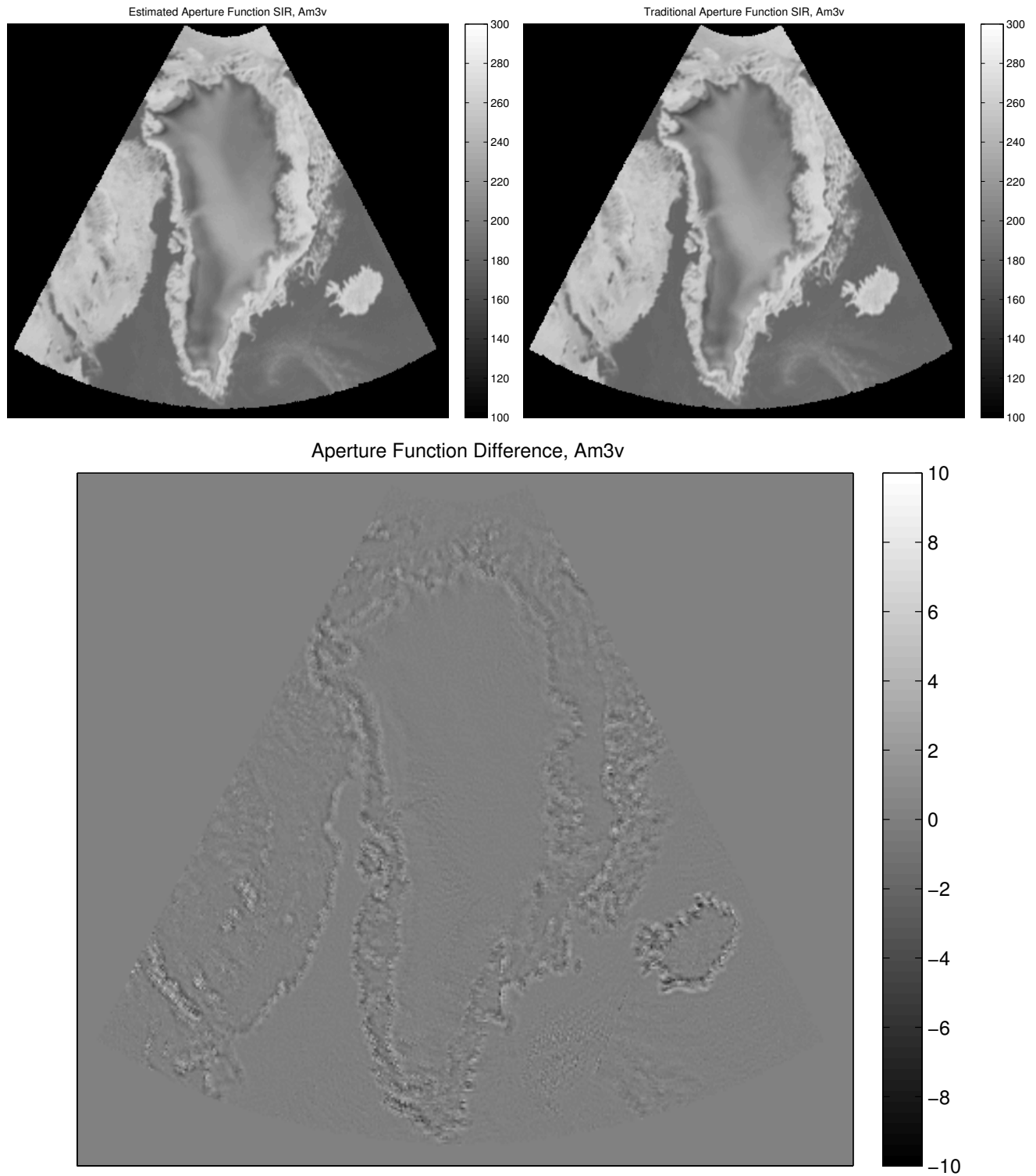


Figure 5.16: SIR Am3v T_B images as in Fig. 5.14.

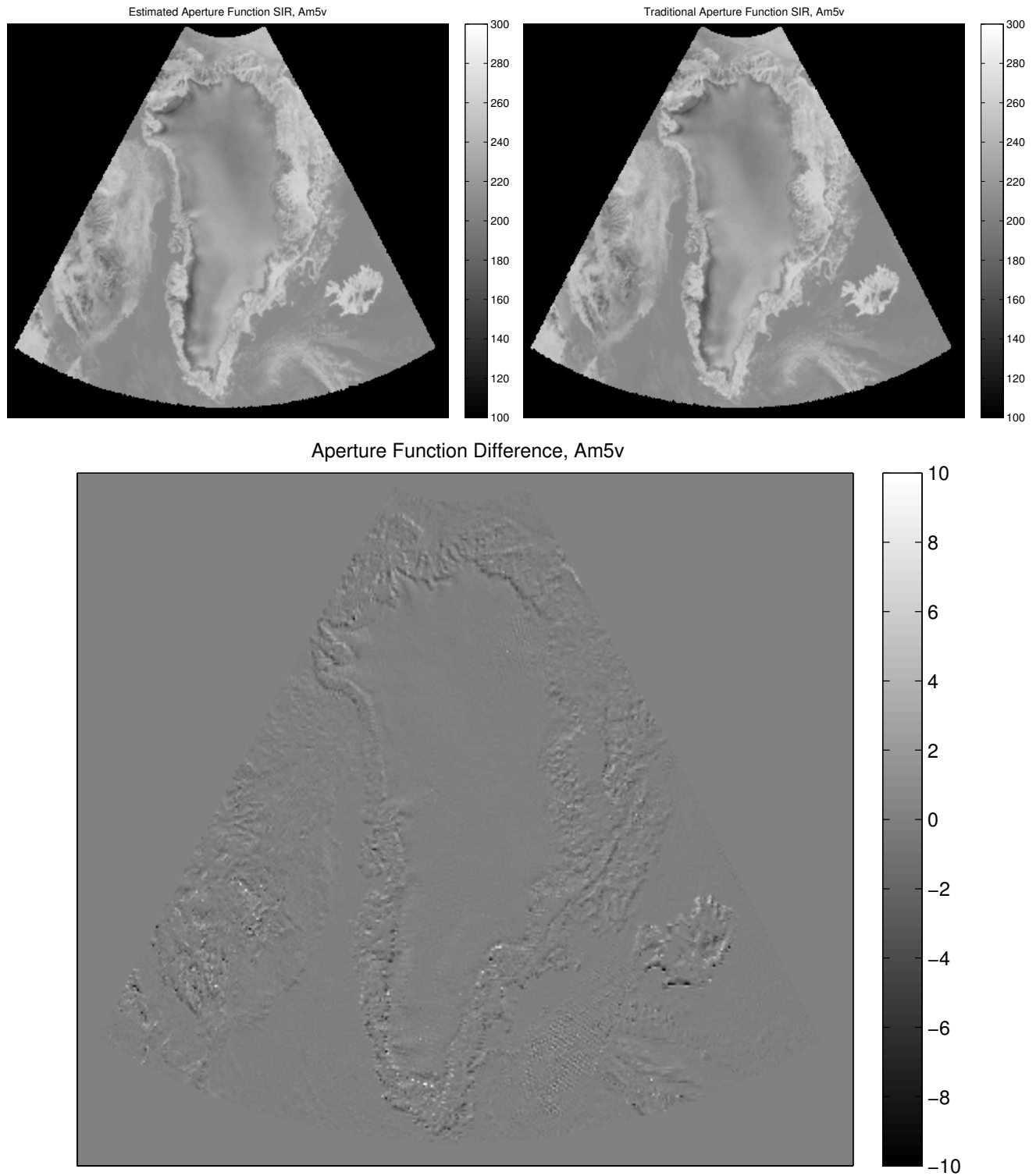


Figure 5.17: SIR Am5v T_B images as in Fig. 5.14.

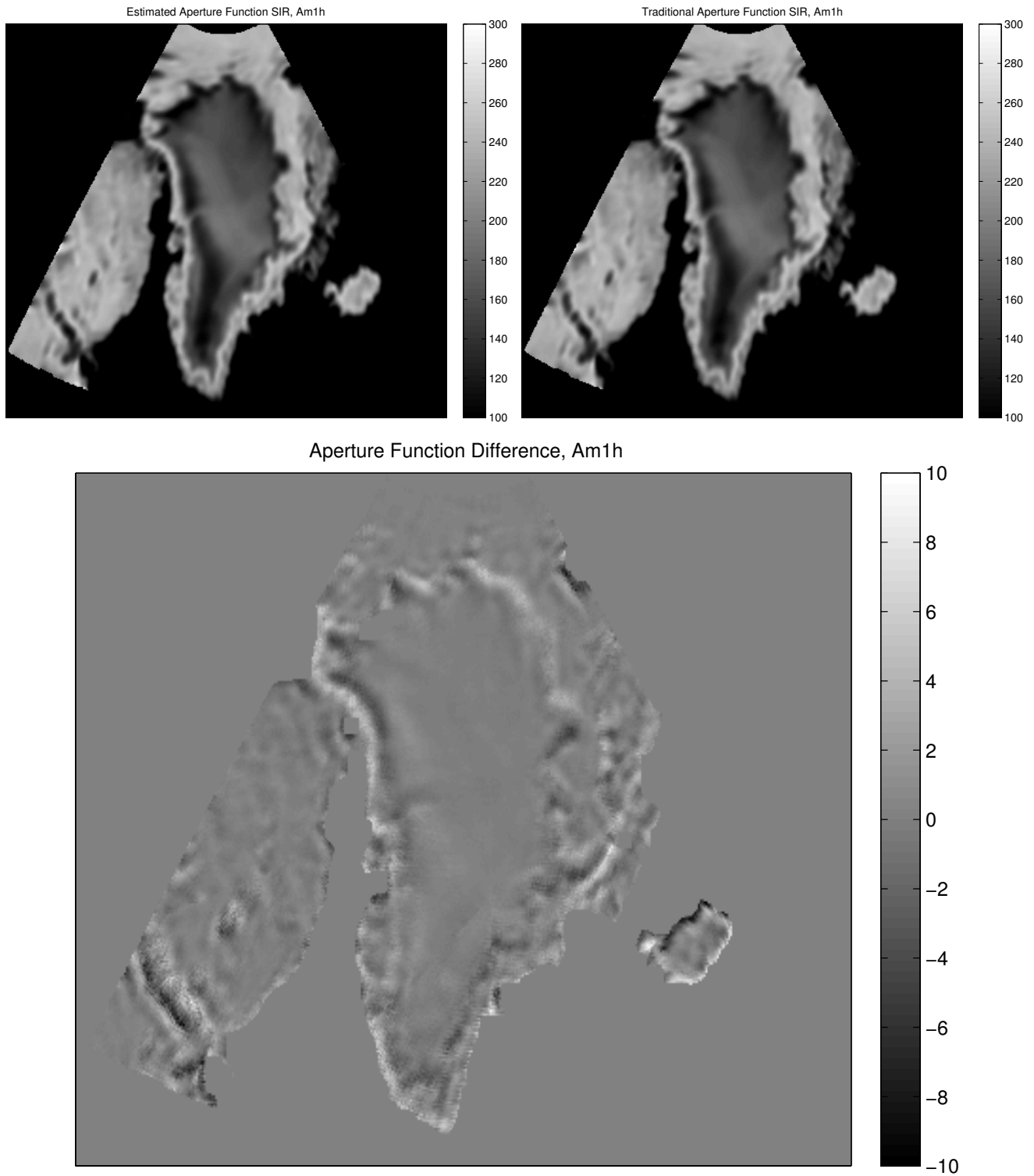


Figure 5.18: SIR Am1h T_B images as in Fig. 5.14. T_B images have a bottom threshold of 100 K.

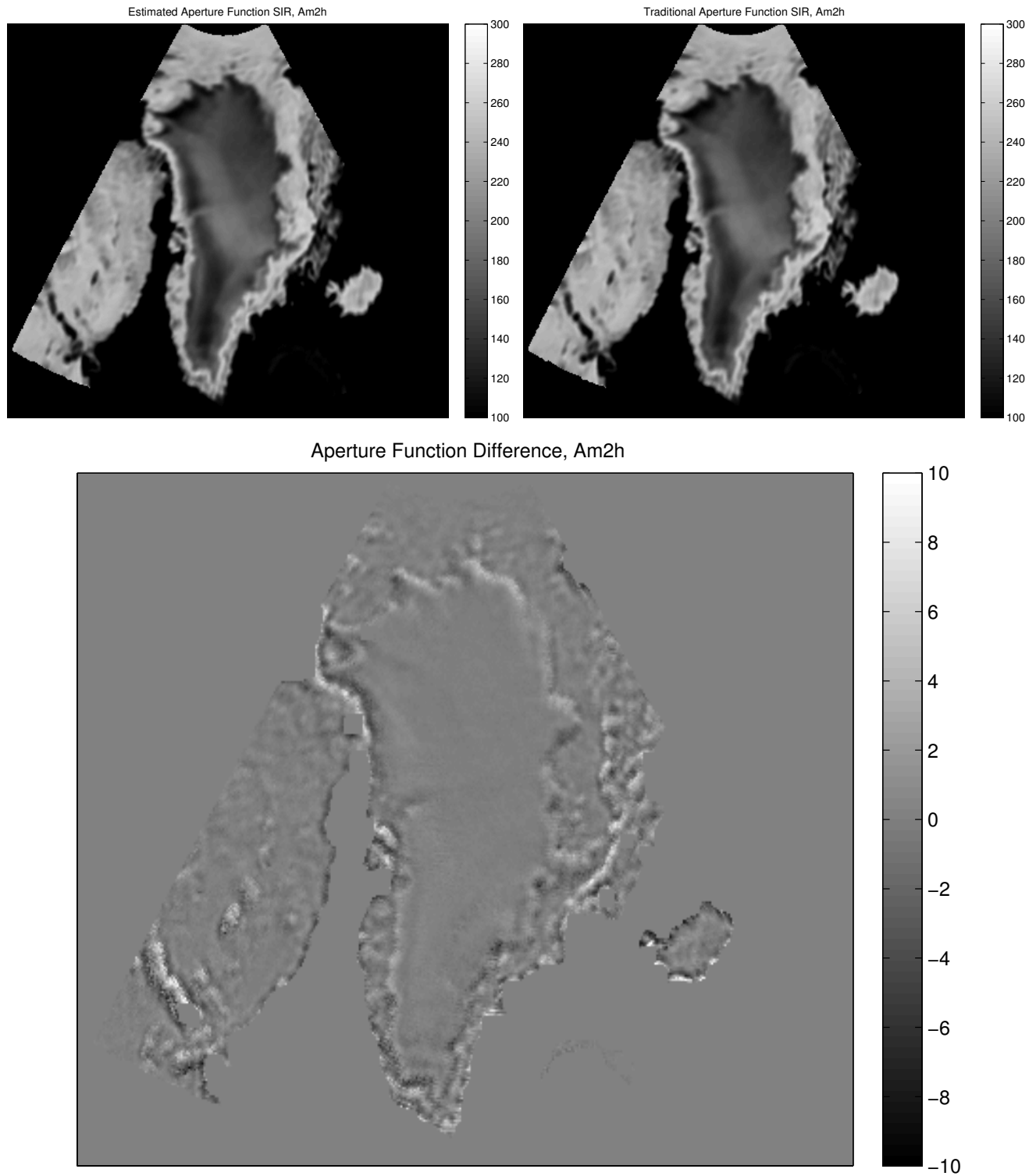


Figure 5.19: SIR Am2h T_B images as in Fig. 5.14.

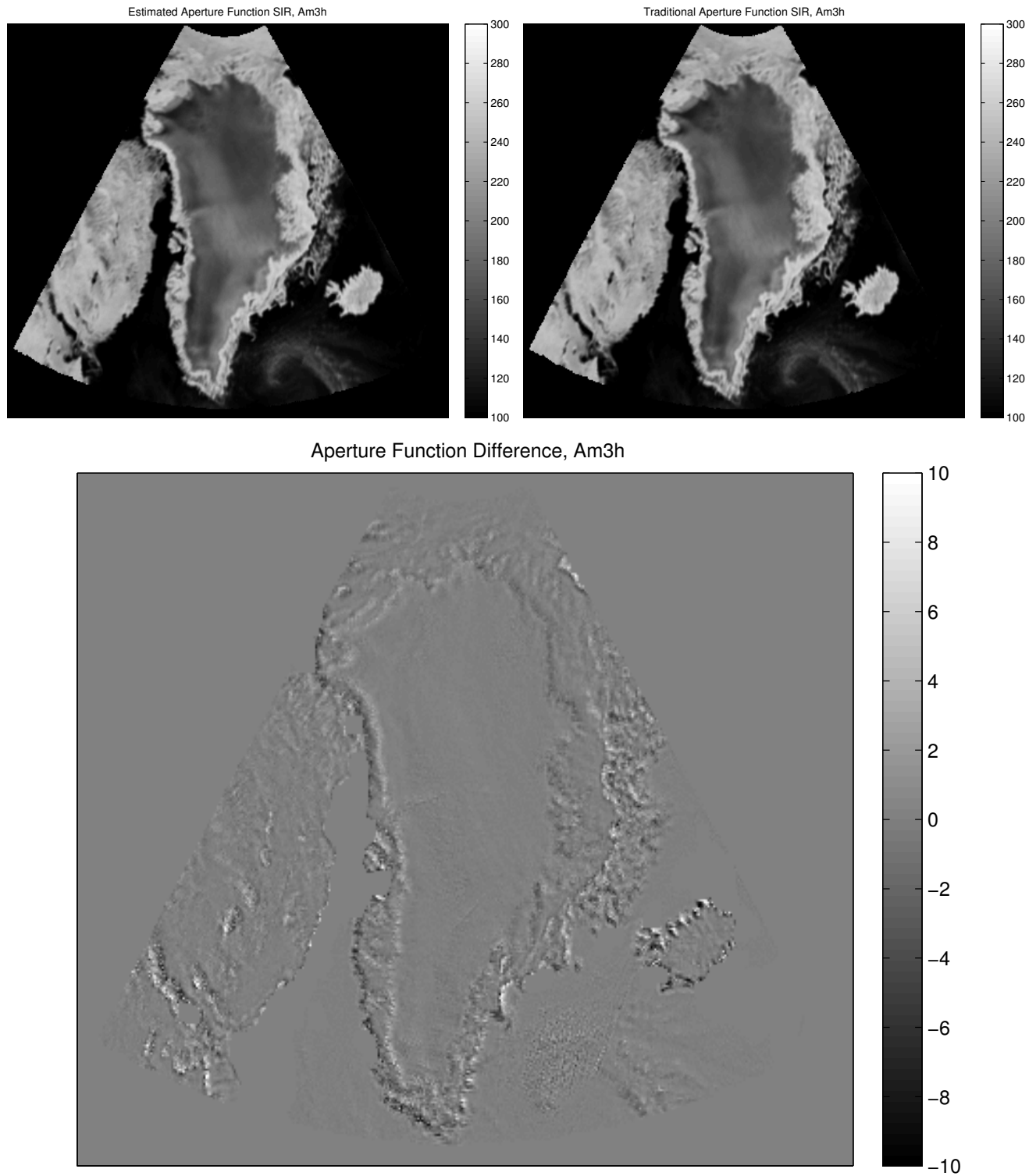


Figure 5.20: SIR Am3h T_B images as in Fig. 5.14.

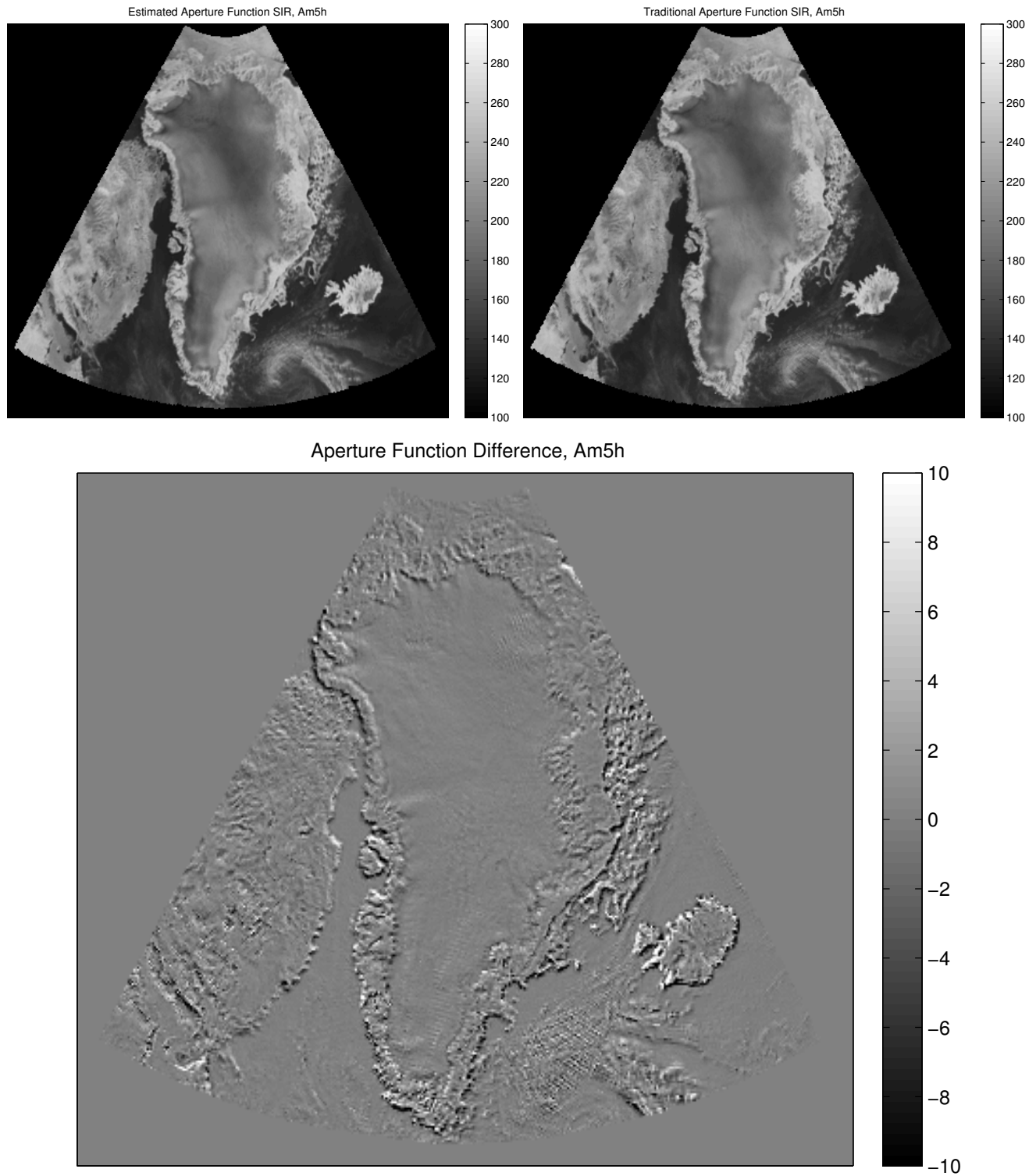


Figure 5.21: SIR Am5h T_B images as in Fig. 5.14.

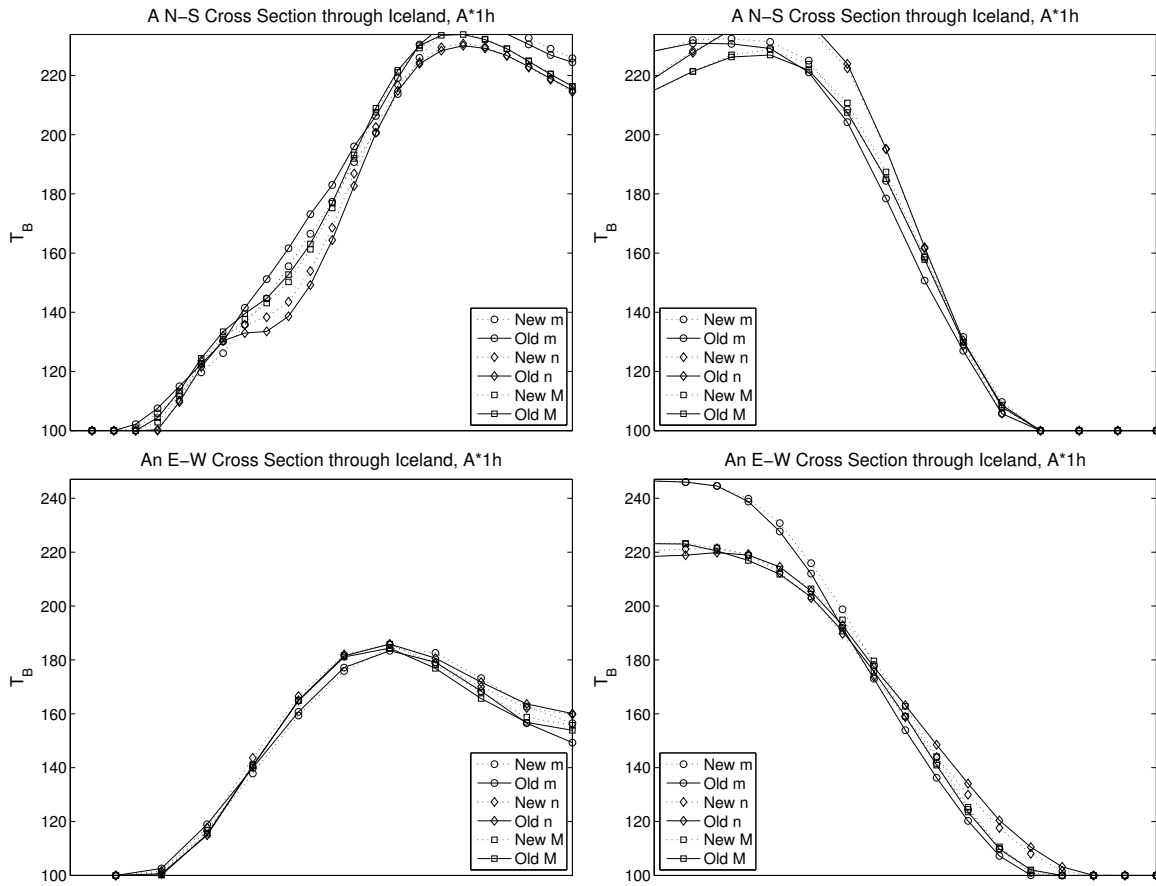


Figure 5.22: T_B plots crossing Iceland coasts to compare consistency of transition T_B between \mathbf{m} , \mathbf{n} , and \mathbf{M} images for the estimated and traditional aperture function SIR. North (upper-left), south (upper-right), west (bottom-left), and east (bottom-right).

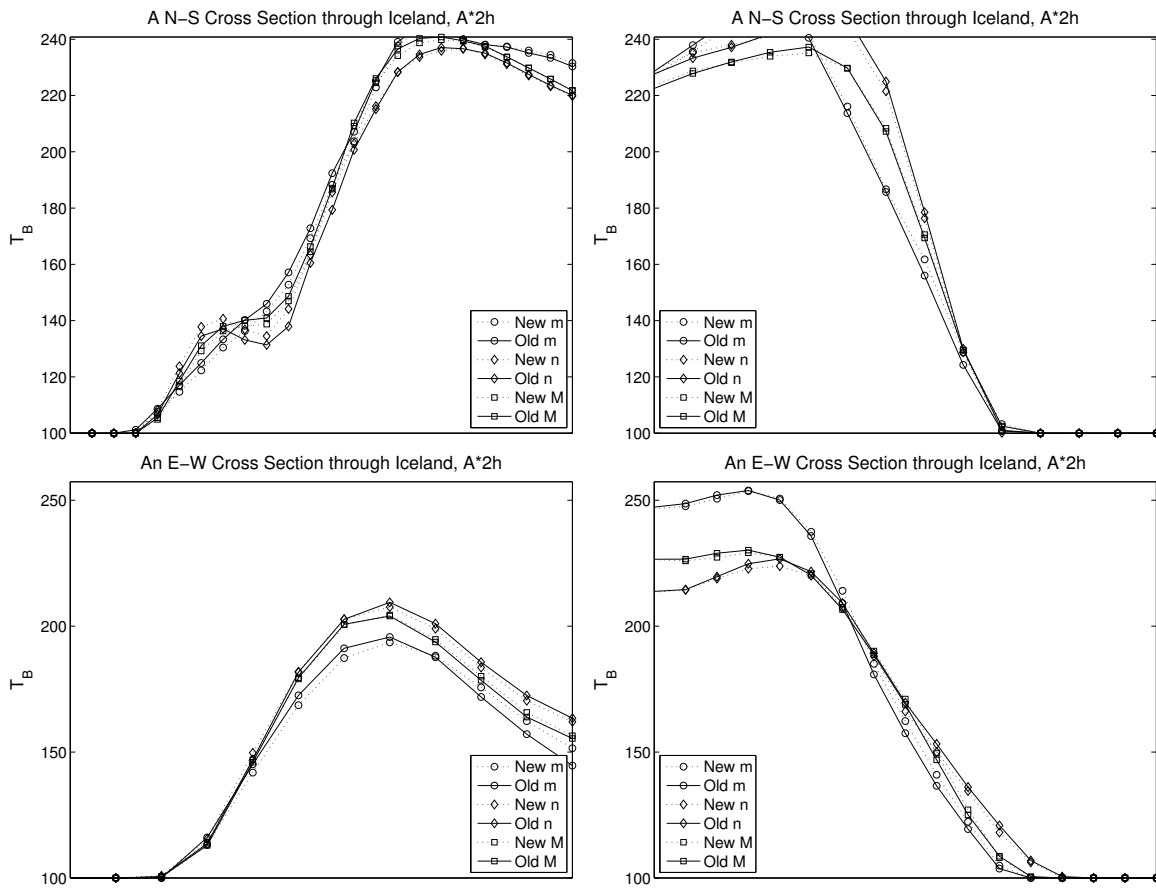


Figure 5.23: An E-W cross section for channel 2h, as in Fig. 5.22.

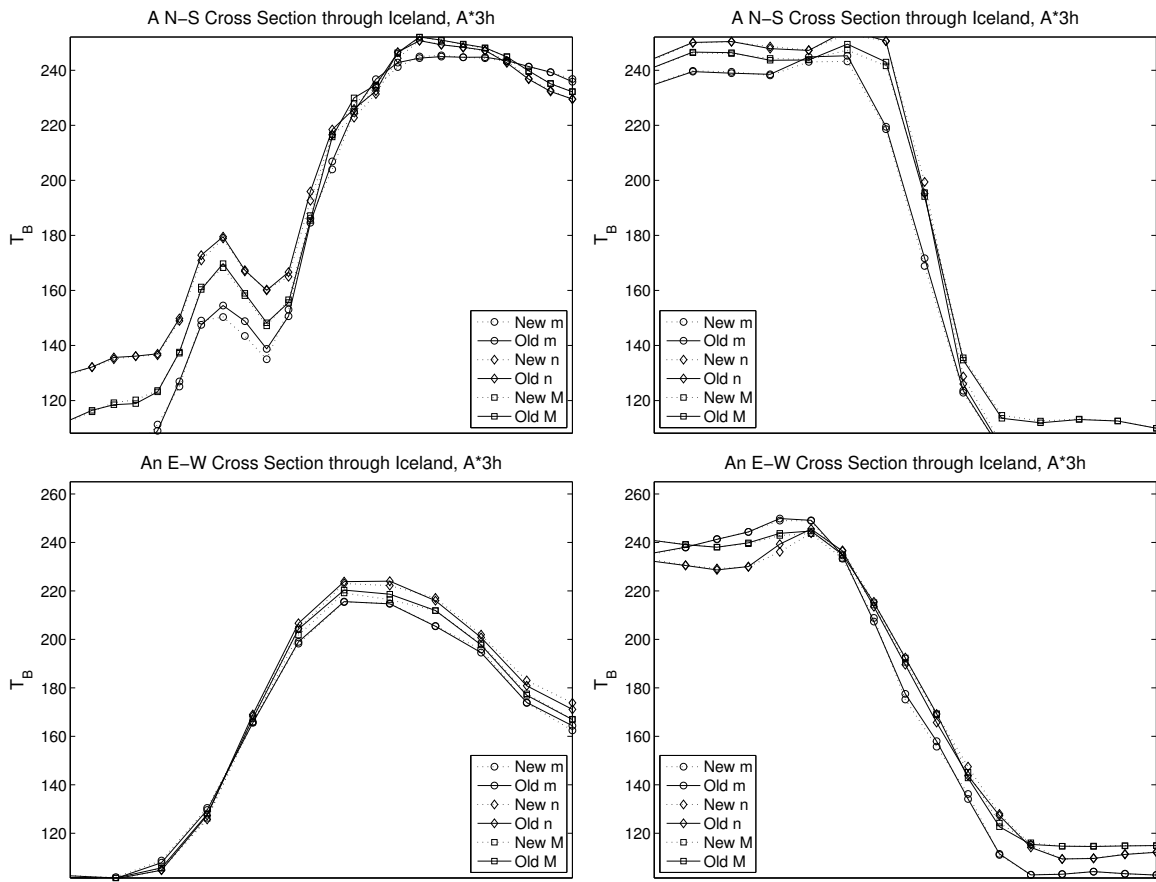


Figure 5.24: An E-W cross section for channel 3h, as in Fig. 5.22.

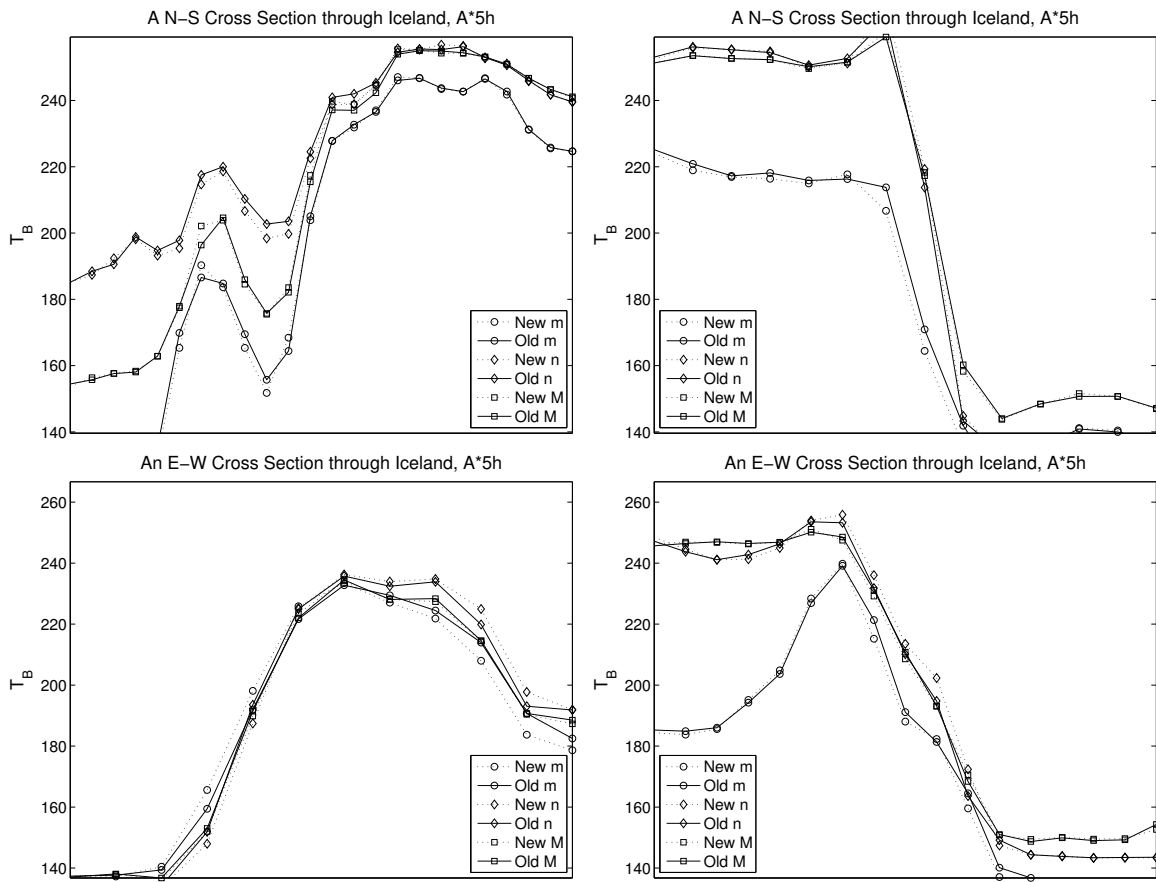


Figure 5.25: An E-W cross section for channel 5h, as in Fig. 5.22.

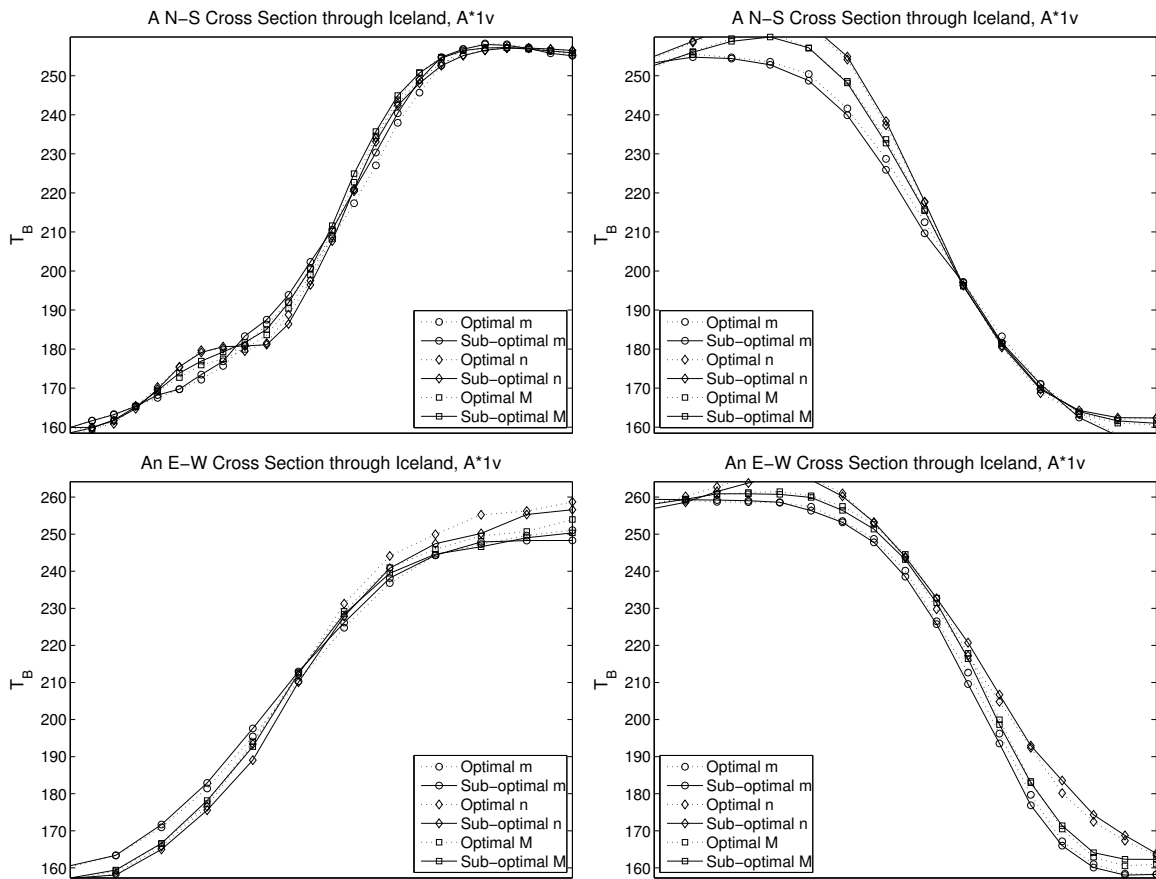


Figure 5.26: An E–W cross section for channel 1v, as in Fig. 5.22.

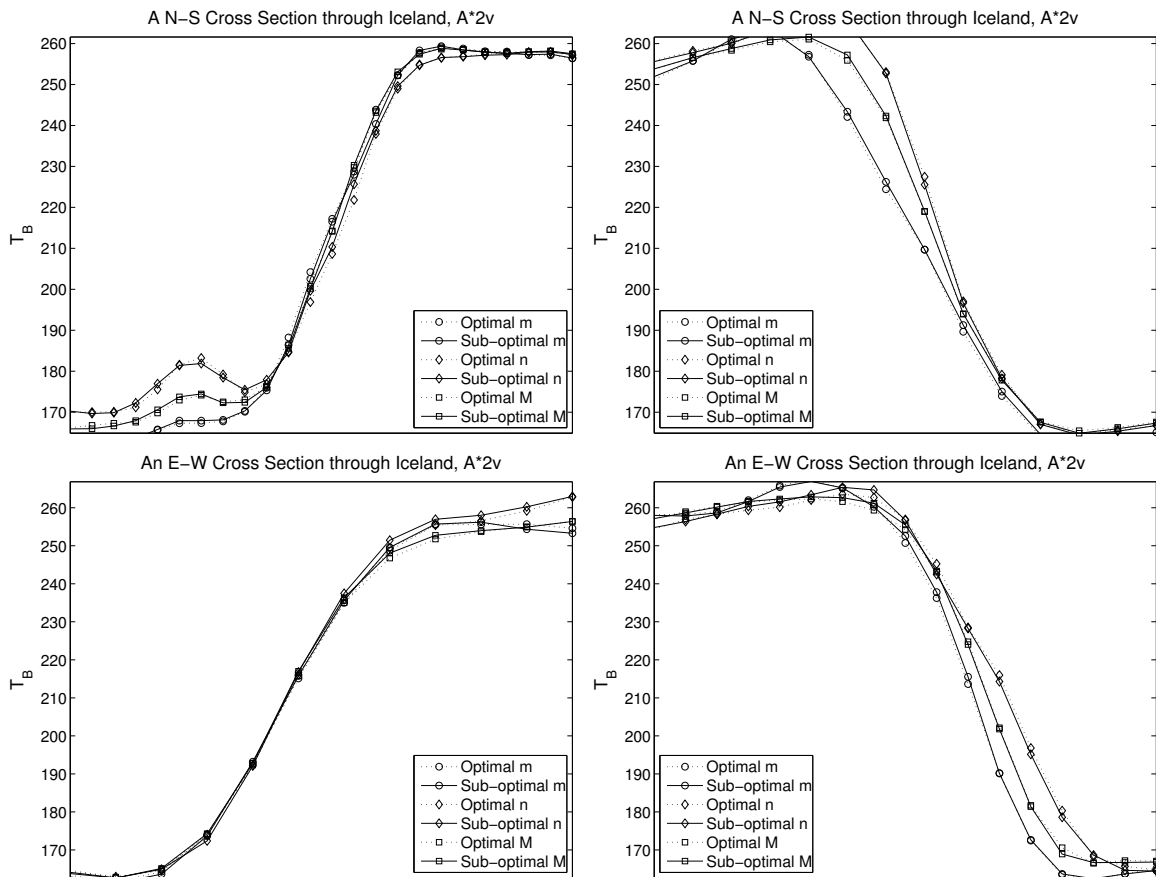


Figure 5.27: An E-W cross section for channel 2v, as in Fig. 5.22.

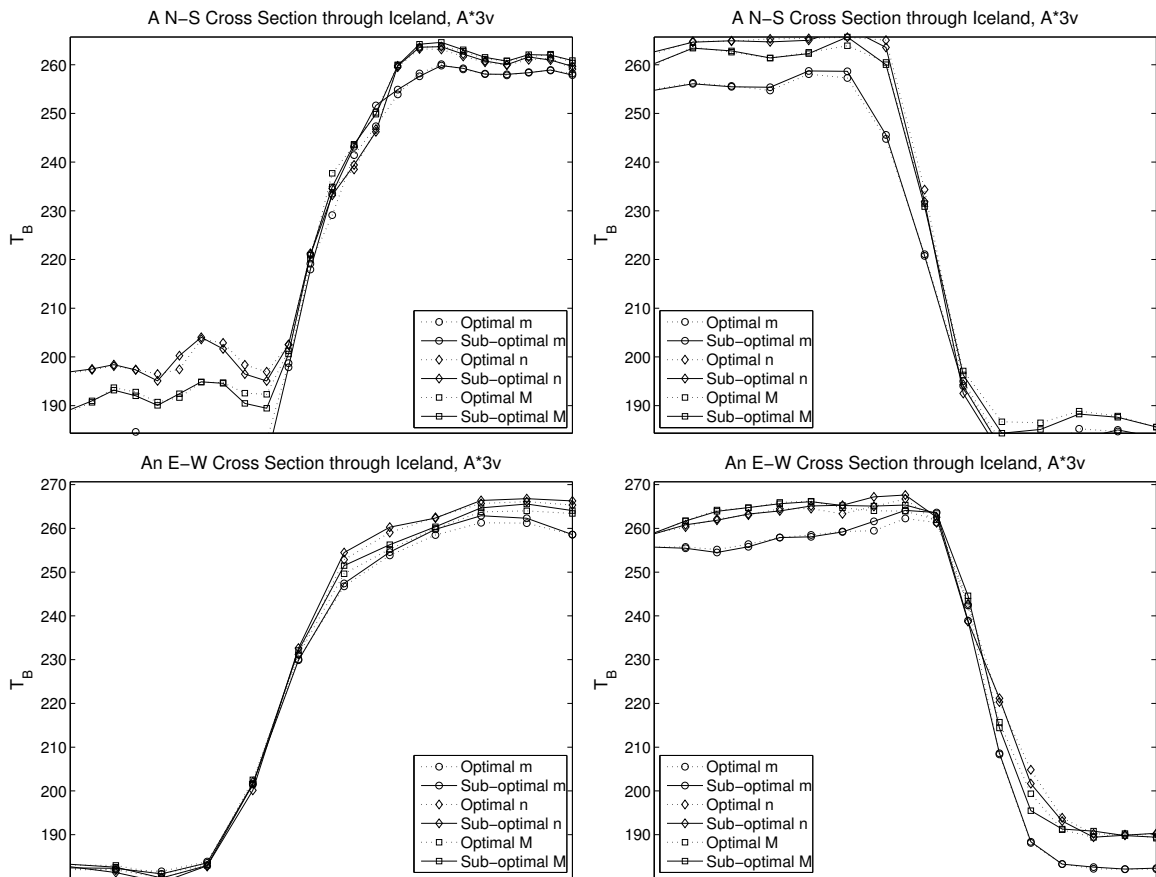


Figure 5.28: An E-W cross section for channel 3v, as in Fig. 5.22.

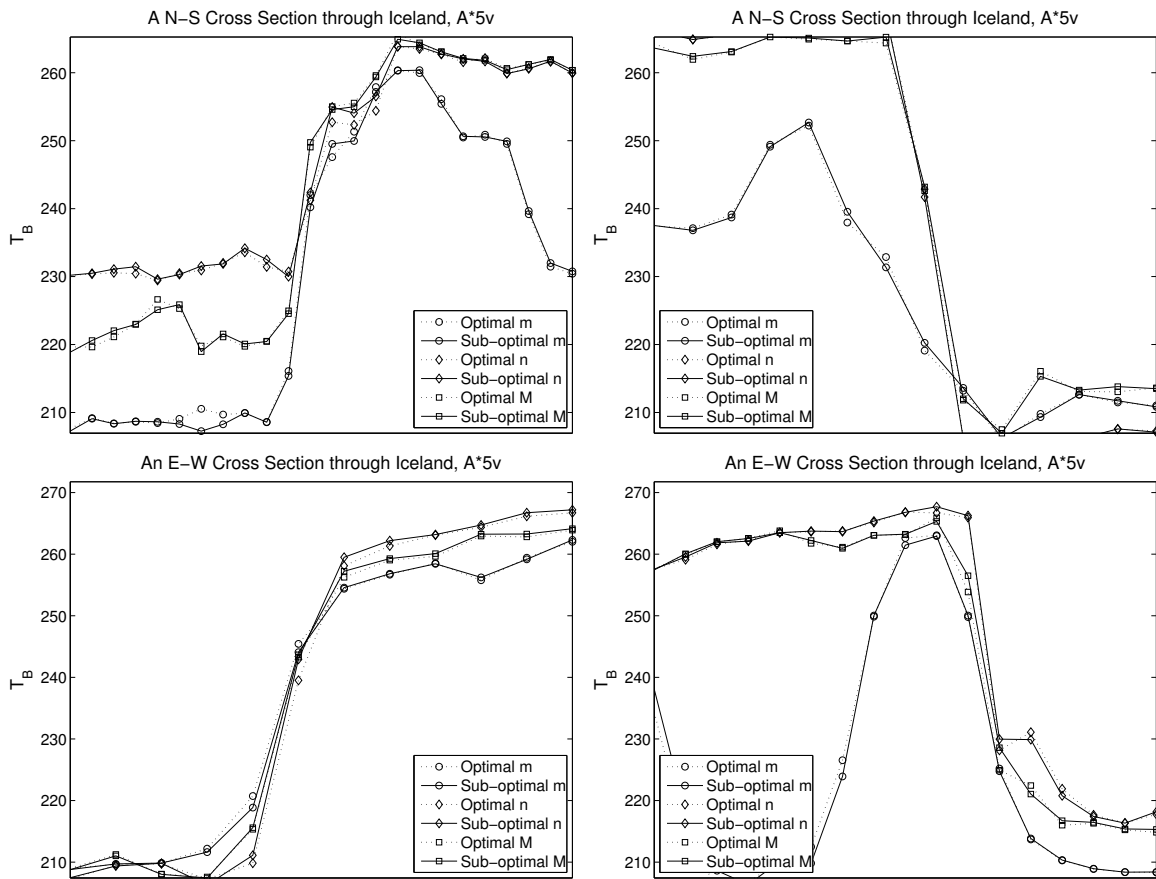


Figure 5.29: An E-W cross section for channel 5v, as in Fig. 5.22.

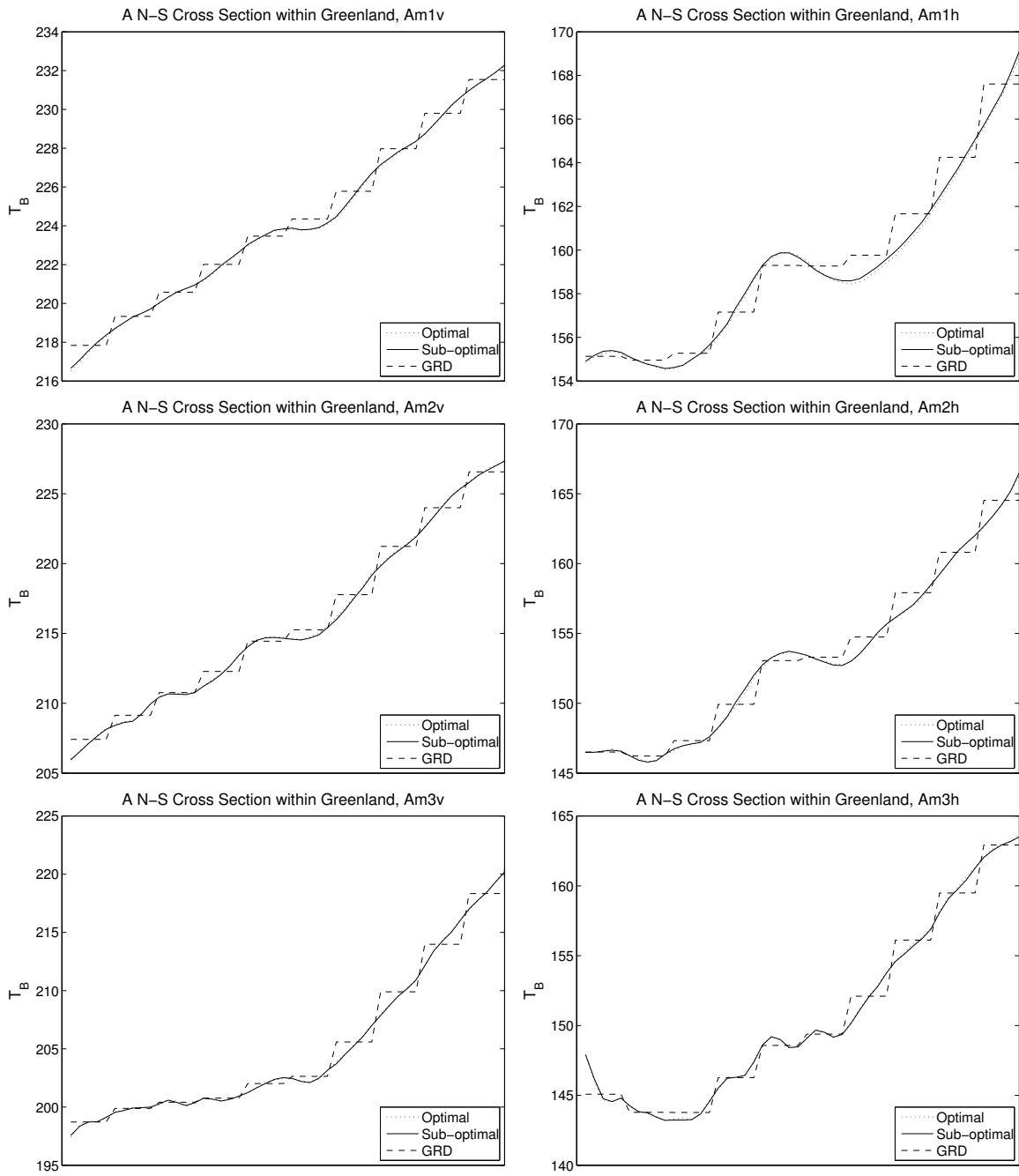


Figure 5.30: A N-S cross section through Greenland, comparing T_B values from using the estimated “optimal” or estimated aperture function and the “sub-optimal” or traditional aperture function in SIR processing. The GRD T_B plot is included for reference.

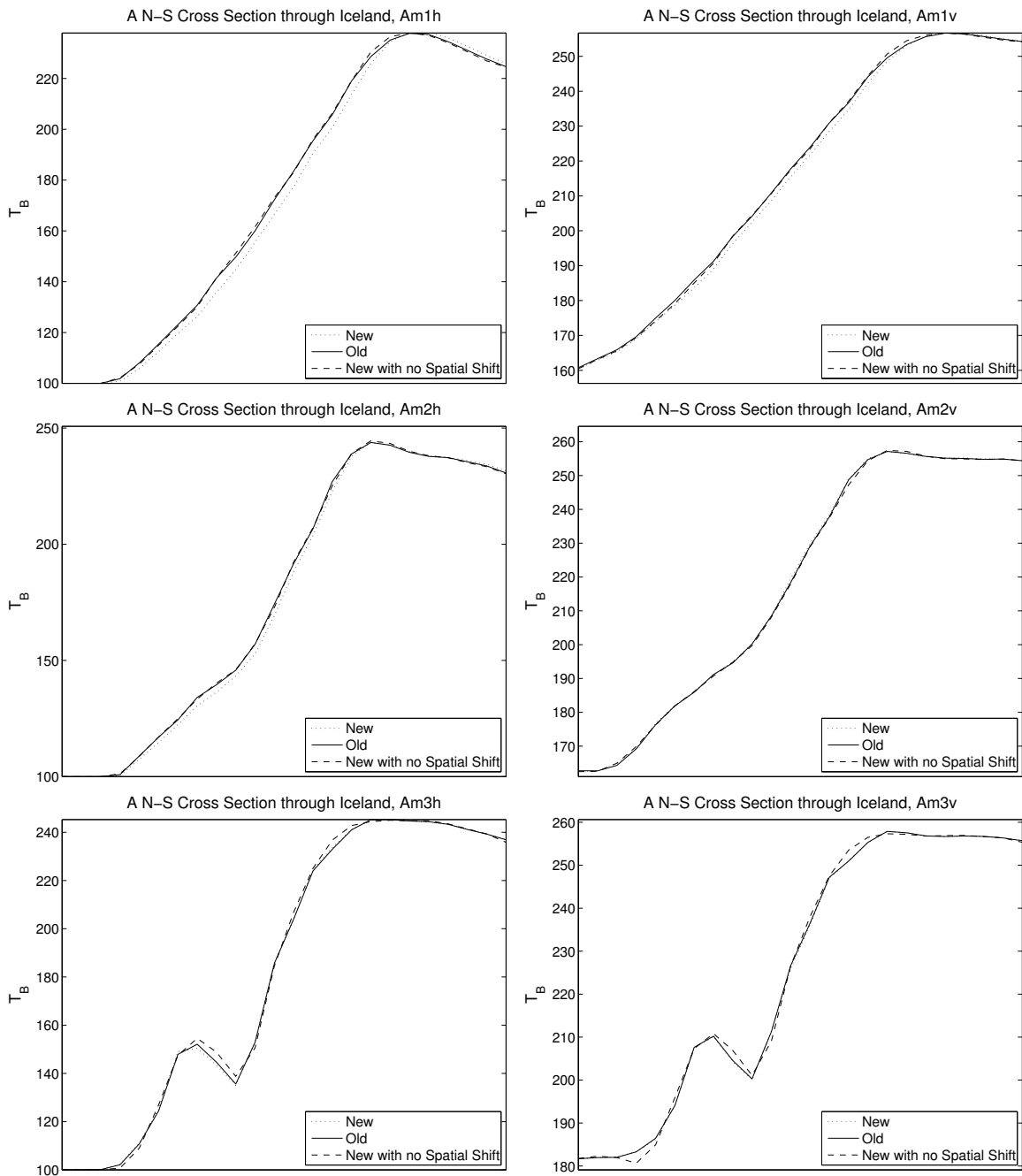


Figure 5.31: A N-S cross section of T_B over Iceland's coast, using the newly estimated aperture function, the old one, and the new one without the spatial shift ($\Delta x, \Delta y = 0$).

In order to determine the primary cause of the shift between images, we process a new set of T_B images using a modified version of the new aperture function estimate which ignores the spatial shifts Δx and Δy . Slices through Iceland's coast for these images are in Fig. 5.31. The plots suggest that the primary cause for the spatial shifts in the output images is due to the non-zero Δx and Δy for at least channels 1h, 1v, and 2h. For the other channels, the increasing difference between the old and modified new SIR T_B images indicates that the spatial T_B shift is most likely related to both spatial shift and orientation of the new sampling aperture. Using both spatial shift and orientation on the new sampling aperture provides a better estimate for use in SIR.

5.3 Conclusion

The image comparisons in this chapter support using the new tuned SIR parameter values over those used previously. The tuned iteration number increases transition sharpness for lower-frequency channels. The tuned aperture function threshold eliminates data gaps within individual swaths and decreases the imaging effects due to temporal variations in T_B between swaths.

SIR T_B images produced using the traditional Gaussian aperture function and those estimated in Chapter 4 are very similar. This is expected due to the small difference between them. Showing the similarities between the traditional and estimated aperture functions and their output images validates using the traditional Gaussian approximation as the aperture function for SIR.

The only apparent difference in images generated using the traditional and the estimated aperture function is a small spatial shift over some regions. Comparing LTOD and daily T_B images for each channel indicates the estimated aperture functions give more consistent coastal lines than the traditional aperture function in SIR for channels 1h, 1v, and 2h. This result supports the adoption of the estimated aperture functions into SIR for these channels.

CHAPTER 6. CONCLUSION

In summary, this research develops a simulation-based optimization of SIR parameters for the AMSR-E radiometer. The parameters—namely the number of SIR iterations and the aperture function threshold—are optimized for each AMSR-E channel. AMSR-E T_B images generated using SIR with the optimized parameter values have sharper transitions between high- and low- T_B regions for the lower-frequency channels. The optimization for the higher-frequency channels shows improvement in eliminating T_B imaging gaps internal to the swath and decreasing the severity of artifacts due to temporal variations in T_B .

Also presented is a method of estimating the aperture function of satellite-based radiometers. The estimated aperture functions result from the a matrix inversion based on satellite sampling. The mathematical formulation requires imposing assumptions and conditions on the target scene to reduce problem complexity and to account for the aperture function frequency support. For most channels, the aperture function estimates differ only slightly from the currently-used approximations, providing them validation for use in SIR.

Unfortunately, aperture function estimates for channel 4 (water band) and 6 (oxygen band) were unattainable due to reduced SNR. Both channels suffer from atmospheric contamination. The estimation for channel 6 requires a smaller island to preserve the frequency band containing the aperture function, further decreasing SNR and causing singularity issues.

Some channels' SIR T_B images produced using the estimated aperture functions manifest spatial shifts from those produced using the traditional aperture function. The primary cause of spatial shift in the T_B image is the spatial shift between the center location of the estimated and the traditional aperture function approximation. Comparing LTOD and daily images for each shows improvements afforded by the estimated aperture functions for channels 1h, 1v, and 2h. Other channels' comparison provides no support for using the new estimates over the traditional approximations.

6.1 Contributions

This thesis contains the following contributions:

- A simulator-based optimization method for selecting iteration and aperture function threshold parameters for use in SIR and its application to AMSR-E.
- Modification and validation of optimized SIR parameters for AMSR-E T_B images.
- The development of an aperture function estimation method for spaceborne radiometers.
- Application of the aperture function estimation method to AMSR-E.
- Use of estimated aperture functions in AMSR-E SIR and a comparison of resulting images with those generated using previously-used aperture function estimates.
- Bi-daily local time-of-day processing for AMSR-E. Previously AMSR-E images were produced in daily sets.

6.2 Future Work

Possible direction for future work includes:

- SIR optimization for other satellite radiometers.
- Aperture function estimation for other satellite radiometers.
- Using a more complex target for aperture function estimation. While the oval island target proved effective for most channels, increased SNR would result from a larger target, increasing the estimates' accuracy and perhaps enabling channel 4 and 6 estimation.

REFERENCES

- [1] D. R. Daum, D. G. Long, W.B. Davis “Reconstructing Enhanced Resolution Images from Spaceborne Microwave Sensors,” *International Geoscience and Remote Sensing Symposium, (IGARSS)* Vol. 4, pg. 2231-2233, May 1994. 2
- [2] D. G. Long and D. L. Daum, “Spatial Resolution Enhancement of SSM/I Data,” *IEEE Transactions on Geoscience and Remote Sensing*, Vol. 35, No. 2, pp. 407-417, 1998. 2, 13
- [3] F. T. Ulaby, R. K. Moore, and A. K. Fung, *Microwave Remote Sensing*. Norwood, MA: Artech House, 1981. 5, 7
- [4] JAXA, “AMSR-E Level 3 Products,” <http://sharaku.eorc.jaxa.jp/AMSR/index.html>, Dec. 2009. 8, 9
- [5] “AMSR-E Data Users Handbook,” http://www.eorc.jaxa.jp/en/hatoyama/amsr-e/amsr-e_handbook_e.pdf, Dec. 2009. 9, 10
- [6] NSIDC, “AMSR-E Instrument Description,” http://nsidc.org/data/docs/daac/amsre_instrument.gd.html 11
- [7] NSIDC, “AMSR-E/Aqua Daily L3 25 km T_B and Sea Ice Concentration Polar Grids,” http://nsidc.org/data/docs/daac/ae_si25_25km_tb_and_sea_ice.gd.html, Apr. 2009. 12
- [8] D. S. Early, D. G. Long “Image Reconstruction and Enhanced Resolution Imaging from Irregular Samples,” *International Geoscience and Remote Sensing Symposium, (IGARSS)* Vol. 39, No. 2, Feb. 2001. 12, 13, 14, 24, 26
- [9] D. G. Long, P. J. Hardin, and P. Whiting, “Resolution Enhancement of Spaceborne Scatterometer Data,” *IEEE Transactions on Geoscience and Remote Sensing*, Vol. 31, pp. 700-715, 1993. 13, 14
- [10] D. S. Early, D. G. Long, “Enhanced Resolution Imaging from Irregular Samples,” *IEEE Transactions on Geoscience and Remote Sensing*, Vol. 39, pp 291-302, 2001. 22
- [11] D. G. Long, D. S. Early, and M. R. Drinkwater, “Enhanced Resolution ERS-1 Scatterometer Imaging of Southern Hemisphere Polar Ice,” *International Geoscience and Remote Sensing Symposium, (IGARSS)* Aug. 1994. 26
- [12] B. Gunn “Temporal Resolution Enhancement for AMSR Images,” *Brigham Young University Microwave Remote Sensing Report 07-02*, Dec. 2007. 26
- [13] B. Gunn and D. G. Long “Spatial Resolution Enhancement of AMSR T_b Images Based on Measurement Local Time of Day,” *International Geoscience and Remote Sensing Symposium, (IGARSS)*, Paper FR1.103.2, Jul. 2008. 26

- [14] G. Watt,, and D. G. Long, *Temporal Average Estimate Algorithm for ERS-1/2*, Brigham Young University MERS Report 97-07, 5 August 1997.
- [15] D. G. Long, D. L. Daum, P. J. Hardin “Spatial Resolution Enhancement of SSM/I Data: Vegetation Studies of the Amazon Basin,” *International Geoscience and Remote Sensing Symposium (IGARSS)*, Vol. 3, pg. 1606-1608, May 1996.

APPENDIX A. ANTENNA FAR FIELD AND THE FAST FOURIER TRANSFORM

In this section we show how the antenna pattern is related by Fourier transform to a space-limited equivalence current near the antenna. This section provides the basis of our assumption that the aperture function is low pass. Approximations in the scanning geometry are shown in Fig. A.1.

The relationship between the electric field and the equivalence current induced at the antenna can be expressed in terms of the 3D Green's Function,

$$\begin{aligned}\bar{E}(\bar{r}) &= i\omega\mu \int_V G(\bar{r}, \bar{r}') \cdot \bar{J}(\bar{r}') d\bar{r}', \\ &= i\omega\mu [\bar{I} + \frac{1}{k^2} \nabla \nabla] \cdot \int_V \frac{e^{ik|\bar{r}-\bar{r}'|}}{4\pi|\bar{r}-\bar{r}'|} \bar{J}(\bar{r}') d\bar{r}',\end{aligned}\tag{A.1}$$

with

- $\bar{E}(\bar{r})$: induced electric field,
- i : imaginary unit,
- ω : radian frequency,
- G : Green's Function,
- J : electric equivalence current density,
- k : wave number = $\omega\sqrt{\mu\epsilon}$,
- \bar{I} : identity matrix.

The vectors \bar{r} and \bar{r}' are position vectors indexing the electric field and current density, respectively. If $\bar{r} \gg \bar{r}'$, the term $|\bar{r}-\bar{r}'|$ can be approximated to zeroth order by $r = ||\bar{r}||$ in the denominator and

to first order by $r - \hat{r} \cdot \vec{r}'$ in the phase of the integral kernel, giving

$$\begin{aligned}\bar{E}(\vec{r}) &\approx i\omega\mu\left[\bar{I} + \frac{1}{k^2}\nabla\nabla\right] \cdot \int_V \frac{e^{ik(\vec{r}-\hat{r}\cdot\vec{r}')}}{4\pi r} \bar{J}(\vec{r}') d\vec{r}' \\ &\approx i\omega\mu \frac{e^{ikr}}{4\pi r} \left[\bar{I} + \frac{1}{k^2}\nabla\nabla\right] \\ &\quad \cdot \int_V e^{-ik(\hat{r}\cdot\vec{r}')} \bar{J}(\vec{r}') d\vec{r}'.\end{aligned}$$

Furthermore, if the support of $\bar{J}(\vec{r}')$ is restricted to a plane, the broadside electric field can be approximated as

$$\bar{E}(\vec{r}) \approx i\omega\mu \frac{e^{ikr}}{4\pi r} \int_A e^{-ik(\hat{r}\cdot\vec{r}')} \bar{J}(\vec{r}') d\vec{r}'.$$

Restricting $\bar{J}(\vec{r}')$ to the $y-z$ plane,

$$\vec{r}' = \hat{y} y' + \hat{z} z'.$$

Although AMSR-E's pencil beam is not broadside to the current on the reflector dish, Huygens's principle states that the far-field electric field for a current can be generated by an equivalent current impressed on a surface which encloses the real current. This is the equivalent current corresponding to \bar{J} . Although the exact location and spatial extent is unknown, the equivalent current is near the antenna and spatially limited to approximately the size of the reflector.

The phase term $\hat{r} \cdot \vec{r}'$ can be approximated by truncating the Taylor series of the \hat{r} term.

$$\begin{aligned}\hat{r} &= \hat{x} \cos(\gamma)\cos(\zeta) + \hat{y} \sin(\gamma) + \hat{z}\cos(\gamma)\sin(\zeta) \\ &\approx \hat{x} + \hat{y} \gamma + \hat{z} \zeta,\end{aligned}$$

with

$$\begin{aligned}\gamma &= \sin^{-1}\left(\frac{y}{r}\right), \\ \zeta &= \tan^{-1}\left(\frac{z}{x}\right),\end{aligned}$$

with γ, ζ the elevation and azimuth angles from broadside, respectively. The primed parameters again refer to the current distribution over the antenna reflector, the unprimed to the far electric

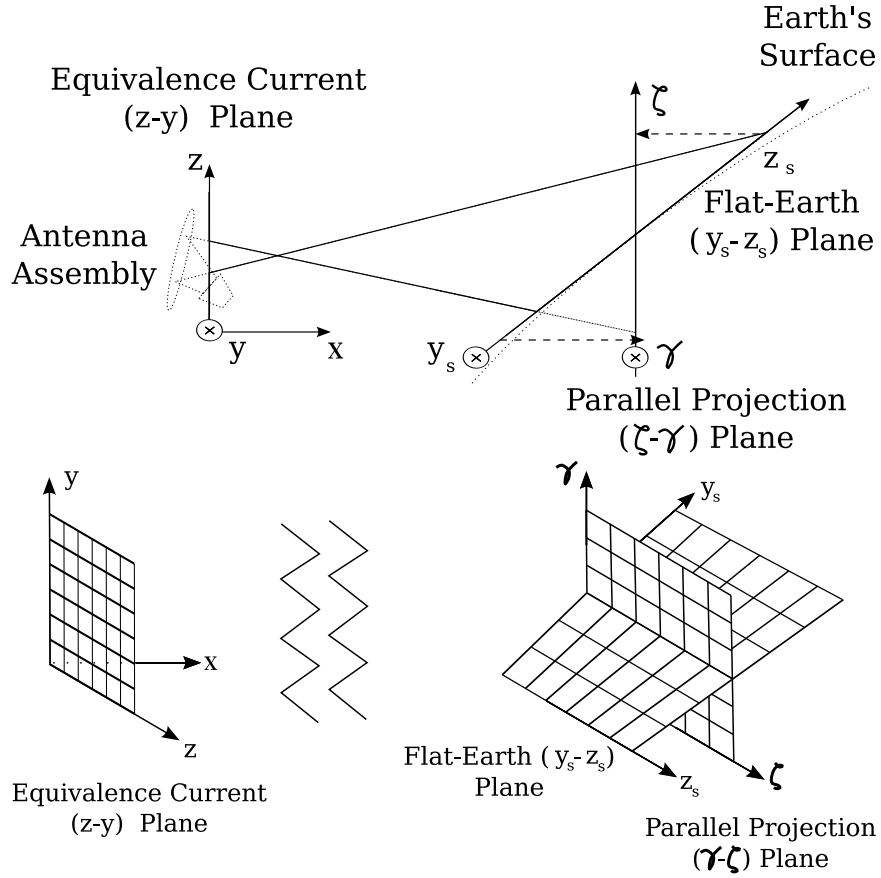


Figure A.1: Figure showing the simplifications used in deriving the Fourier-transform relationship between an equivalence current and the far-field antenna pattern. On the left is the equivalence current assumption and its coordinate system (x, y, z) . On the right is the flat-Earth approximation and coordinates (y_s, z_s) , and the parallel projection plane (γ, ζ) .

field. In our problem, the maximum γ and ζ over the main lobe are about a tenth of a radian, producing a maximum error of a few tenths of a percent through this approximation. These simplifications give

$$\begin{aligned}
 \hat{r} \cdot \vec{r}' &\approx (\hat{x} + \hat{y} \gamma + \hat{z} \zeta) \cdot (\hat{y} y' + \hat{z} z') \\
 &= y' \gamma + z' \zeta \\
 &= y' \sin^{-1} \left(\frac{y}{r} \right) + z' \tan^{-1} \left(\frac{z}{x} \right).
 \end{aligned}$$

Because r and x are larger than 1000 km and y and z are on the order of tens of kilometers, we approximate the arctangent and arcsine to first order:

$$\begin{aligned}\gamma &= \sin^{-1}\left(\frac{y}{r}\right) \approx \frac{y}{r}, \\ \zeta &= \tan^{-1}\left(\frac{z}{x}\right) \approx \frac{z}{x}, \\ \hat{r} \cdot \vec{r}' &\approx y' \left(\frac{y}{r}\right) + z' \left(\frac{z}{x}\right).\end{aligned}$$

As y and z is small in comparison and nearly tangent to r , $r \approx x$, and

$$\begin{aligned}\gamma &\approx \frac{y}{x}, \\ \hat{r} \cdot \vec{r}' &\approx y' \left(\frac{y}{x}\right) + z' \left(\frac{z}{x}\right).\end{aligned}$$

Note from Fig. A.1 that although γ and ζ are angles, they're represented in a plane near the antenna footprint. This ‘‘parallel projection plane’’ arises from the simplifications we've made based on the geometry of the problem and is called such because it is parallel to the equivalence current plane. In terms of the parallel projection ($\gamma - \zeta$, in radians) plane coordinates,

$$\begin{aligned}\bar{E}_s(\bar{r}(\gamma, \zeta)) &= \bar{E}_s(\gamma, \zeta) \\ &\approx \tilde{A}(\gamma, \zeta) \int_A e^{-ik(y'\gamma + z'\zeta)} \bar{J}(\vec{r}') d\vec{r}', \\ \gamma &= \left(\frac{y}{x}\right), \\ \zeta &= \left(\frac{z}{x}\right), \\ \bar{r}(\gamma, \zeta) &\approx R_0 \left(1 + \frac{\gamma}{\cos(\theta_i)}\right), \\ \tilde{A}(\bar{r}(\gamma, \zeta)) &= \tilde{A}(\gamma, \zeta) = \frac{\omega\mu}{4\pi r(\gamma, \zeta)}.\end{aligned}\tag{A.2}$$

One may recognize the similarities between the integral kernel in Eq. A.2 and that of the Fourier transform. Letting \mathcal{F}' be a phase-scaled Fourier transform, we have

$$\begin{aligned}\bar{E}(\gamma, \zeta) &\approx \tilde{A}(\gamma, \zeta) \mathcal{F}'[\bar{J}(y', z')], \\ \frac{\bar{E}(\gamma, \zeta)}{\tilde{A}(\gamma, \zeta)} &\stackrel{\mathcal{F}'}{\leftrightarrow} \bar{J}(y', z').\end{aligned}\tag{A.3}$$

Consider a discretization of this function with Δ_f spacing and a finite sum approximation over Δ_A -spaced samples of the aperture current.

$$\begin{aligned} y'_m &= \Delta_A m, \\ z'_n &= \Delta_A n, \\ \gamma_u &= \Delta_f u, \\ \zeta_v &= \Delta_f v, \\ \frac{\bar{E}(\gamma, \zeta)}{A(\gamma, \zeta)} &\approx \end{aligned}$$

$$\Delta_A^2 \sum_{m=1}^M \sum_{n=1}^N \left(e^{-ik(y'_m \gamma_u + z'_n \zeta_v)} \bar{J}(y'_m, z'_n) \right). \quad (\text{A.4})$$

This can be represented as a scaled FFT if the kernel index dimensions agree.

$$\begin{aligned} -ik(\Delta_A m \Delta_f u + \Delta_A n \Delta_f v) &= -i2\pi \left(\frac{mu}{M} + \frac{nv}{N} \right), \\ \frac{2\pi}{\lambda} (\Delta_A m \Delta_f u + \Delta_A n \Delta_f v) &= 2\pi \left(\frac{mu}{M} + \frac{nv}{N} \right), \end{aligned}$$

$$\begin{aligned} \frac{\Delta_A \Delta_f mu}{\lambda} &= \frac{mu}{M}, & \frac{\Delta_A \Delta_f nv}{\lambda} &= \frac{nv}{N}, \\ \frac{\Delta_A \Delta_f}{\lambda} &= \frac{1}{M}, & \frac{\Delta_A \Delta_f}{\lambda} &= \frac{1}{N}. \end{aligned}$$

Therefore, if the forward or inverse FFT is used to implement this transform for the discrete case, the factors $\frac{\lambda}{M}$ and $\frac{\lambda}{N}$ must be accounted for in the domain transformation. In our formulation, we choose to estimate h over a square grid, i.e. $M = N$.

The AMSR-E beam incidence angle θ_i is nominally 55° with a footprint size that justifies the local flat-Earth approximation. Because both the γ - ζ plane and the flat-Earth approximation plane are in the far field, we assume that the antenna pattern is the same function at all ranges over our estimation grid spatial extent.

With this assumption, the γ - ζ and the corresponding electric field approximation is related to the surface electric field by projection along the rays of constant angle from the satellite. Function scaling is dictated by the range at the flat-Earth approximated surface.

The electric field on the Earth's surface is

$$\begin{aligned}\bar{E}_s(\bar{r}) &\approx i\omega\mu \frac{e^{ikr}}{4\pi r} \int_A e^{-ik(\hat{r}\cdot\bar{r}')} \bar{J}(\bar{r}') d\bar{r}', \\ \hat{r}\cdot\bar{r}' &\approx y' \left(\frac{y}{\chi(z)} \right) + z' \left(\frac{z}{\chi(z)} \right), \\ x &= \chi(z) = R_0 + z \sin(\theta_i).\end{aligned}\tag{A.5}$$

The linear coordinate transformation between the $\gamma - \zeta$ and flat-Earth ($y_s - z_s$) planes is

$$\begin{aligned}\frac{y}{\chi(z)} &= \frac{y_s}{\chi(z_s \cos(\theta_i))} = \frac{y_s}{R_0 + z_s \cos(\theta_i) \sin(\theta_i)}, \\ \frac{z}{\chi(z)} &= \frac{z_s \cos(\theta_i)}{\chi(z_s \cos(\theta_i))} = \frac{z_s \cos(\theta_i)}{R_0 + z_s \cos(\theta_i) \sin(\theta_i)}, \\ z_s &\approx \frac{z}{\cos(\theta_i)}, \\ y_s &\approx y.\end{aligned}$$

This suggests that although the reflector plane is in the spatial-frequency space (in units of inverse meters), it is also in normal space (in units of meters). This relationship allows us to base the spectral support of the spatial low-pass model and filters discussed in this paper on the dimensions of the antenna reflector.

APPENDIX B. ξ AND APERTURE ROTATION BIAS

If we perform a rotation of angle t :

$$\begin{aligned}\gamma_2 &= \gamma_1 \cos(t) - \zeta_1 \sin(t), \\ \zeta_2 &= \gamma_1 \sin(t) + \zeta_1 \cos(t),\end{aligned}$$

then

$$\begin{aligned}\left(\frac{\gamma_2}{\gamma_{02}}\right)^2 + \left(\frac{\zeta_2}{\zeta_{02}}\right)^2 &= \frac{(\gamma_1 \cos(t) - \zeta_1 \sin(t))^2}{\gamma_{02}^2} \\ &\quad + \frac{(\gamma_1 \sin(t) + \zeta_1 \cos(t))^2}{\zeta_{02}^2} \\ &= \gamma_1 \left(\frac{\cos^2(t)}{\gamma_{02}^2} + \frac{\sin^2(t)}{\zeta_{02}^2} \right) \\ &\quad + \gamma_1 \zeta_1 \cos(t) \sin(t) \left(\frac{1}{\zeta_{02}^2} - \frac{1}{\gamma_{02}^2} \right) \\ &\quad + \zeta_1 \left(\frac{\sin^2(t)}{\gamma_{02}^2} + \frac{\cos^2(t)}{\zeta_{02}^2} \right) \\ &= \left(\frac{\gamma_1}{\gamma_{01}} \right)^2 + \xi \gamma_1 \zeta_1 + \left(\frac{\zeta_1}{\zeta_{01}} \right)^2,\end{aligned}$$

with

$$\begin{aligned}\gamma_{01} &= \frac{\gamma_{02}^2 \zeta_{02}^2}{\gamma_{02}^2 \sin^2(t) + \zeta_{02}^2 \cos^2(t)}, \\ \zeta_{01} &= \frac{\gamma_{02}^2 \zeta_{02}^2}{\gamma_{02}^2 \cos^2(t) + \zeta_{02}^2 \sin^2(t)}, \\ \xi &= \cos(t) \sin(t) \left(\frac{\gamma_{02}^2 - \zeta_{02}^2}{\gamma_{02}^2 \zeta_{02}^2} \right).\end{aligned}$$

Although the rotation of the axes is more difficult to express in a single equation and slightly more computationally intensive than simply using the cross term ξ , it is perhaps more intuitive. We call t the estimated aperture rotation bias.

Because our model is in the y - z and γ - ζ planes, we need to project it into the y_s - z_s or the Earth-surface plane. The domain transformations discussed in Appendix A are repeated here:

$$\begin{aligned}\gamma &= \frac{y_s}{R_0 + z_s \cos(\theta_i) \sin(\theta_i)}, \\ \zeta &= \frac{z_s \cos(\theta_i)}{R_0 + z_s \cos(\theta_i) \sin(\theta_i)}.\end{aligned}$$

By substituting these equations for γ and ζ , we can update the equation for h_G in terms of y_s and z_s . Note that a direct substitution of these variables neglects the scaling in the radar equation due to range differences in the elevation angle in the aperture function. Since the footprint pixel range is approximately $R_0 + z_s \sin(\theta_i)$ from the antenna, a range mitigation factor

$$c_R = \left(\frac{R_0}{R_0 + z_s \sin(\theta_i)} \right)^2,$$

can be multiplied to account for the difference in ranges. Since this is a nearly-linear relationship, we let the spatial shift parameters Δy and Δz compensate for this effect.